

**UNIFIED ELECTRON EMISSION AND GAS BREAKDOWN THEORY
ACROSS LENGTH, PRESSURE, AND FREQUENCY**

by

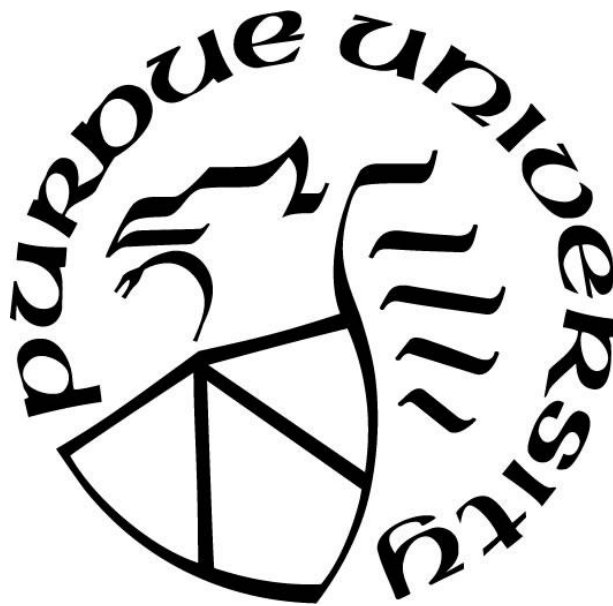
Amanda M. Loveless

A Dissertation

Submitted to the Faculty of Purdue University

In Partial Fulfillment of the Requirements for the degree of

Doctor of Philosophy



School of Nuclear Engineering

West Lafayette, Indiana

August 2020

**THE PURDUE UNIVERSITY GRADUATE SCHOOL
STATEMENT OF COMMITTEE APPROVAL**

Dr. Allen Garner, Chair

School of Nuclear Engineering, Purdue University

Dr. Ahmed Hassanein

School of Nuclear Engineering, Purdue University

Dr. Martin Lopez-De-Bertodano

School of Nuclear Engineering, Purdue University

Dr. Alina Alexeenko

Department of Aeronautics and Astronautics, Purdue University

Dr. Ágúst Valfells

School of Science and Engineering, Reykjavik University

Approved by:

Dr. Seungjin Kim

For my mom and dad, whose love and support have led me to where I am today.

ACKNOWLEDGMENTS

The work for this dissertation was supported by the Office of Naval Research under Grant No. N00014-17-1-2702, the Air Force Office of Scientific Research under award number FA9550-18-1-0218, and the Directed Energy Professional Society. Furthermore, I would like to acknowledge IEEE for awarding me the 2016 IEEE International Conference on Plasma Science (ICOPS) Best Student Paper 1st Place, 2016-2017 IEEE Dielectric and Electrical Insulation Society (DEIS) Graduate Fellowship, 2017 IEEE Nuclear and Plasma Sciences Society (NPSS) Graduate Scholarship, 2017 IEEE International Conference on Plasma Science (ICOPS) Best Student Paper 2nd runner up, and the 2018 Igor Alexeff Outstanding Student in Plasma Science Award. Finally, I would like to acknowledge my advisor, Dr. Allen Garner, for his invaluable mentorship throughout the years.

TABLE OF CONTENTS

| | |
|--|----|
| LIST OF TABLES | 8 |
| LIST OF FIGURES | 9 |
| ABSTRACT | 14 |
| 1. INTRODUCTION | 17 |
| 1.1 Background | 17 |
| 1.2 Derivation of Breakdown Condition | 24 |
| 1.3 Scope of Dissertation | 30 |
| 2. A UNIVERSAL THEORY FOR GAS BREAKDOWN FROM MICROSCALE TO THE CLASSICAL PASCHEN LAW | 32 |
| 2.1 Introduction | 32 |
| 2.2 Matched Asymptotic Analysis | 33 |
| 2.2.1 Dimensionless breakdown voltage equation | 33 |
| 2.2.2 Asymptotic equation derivation | 40 |
| 2.2.3 Transition to Paschen's law | 44 |
| 2.3 Analysis | 46 |
| 2.3.1 Calculation of V | 46 |
| 2.3.2 Minimum breakdown voltage derivation | 52 |
| 2.3.3 Comparison to experiment | 55 |
| 2.4 Conclusion | 56 |
| 3. DEMONSTRATION OF FIELD EMISSION DRIVEN MICROSCALE GAS BREAKDOWN FOR PULSED VOLTAGES USING IN-SITU OPTICAL IMAGING | 60 |
| 3.1 Introduction | 60 |
| 3.2 In-Situ Electrical-Optical Measurement System | 60 |
| 3.3 DC Microscale Gas Breakdown Theory | 64 |
| 3.4 Results and Discussion | 69 |
| 3.4.1 Results | 69 |
| 3.4.2 Implications to engineering of microplasma devices | 76 |
| 3.5 Conclusion | 77 |

| | |
|---|-----|
| 4. THE TRANSITION TO PASCHEN’S LAW FOR MICROSCALE GAS BREAKDOWN AT SUBATMOSPHERIC PRESSURE..... | 79 |
| 4.1 Introduction..... | 79 |
| 4.2 Theoretical and Experimental Analysis | 79 |
| 4.2.1 Experimental setup and results | 79 |
| 4.2.2 Dimensionless model derivation and comparison to experiment | 81 |
| 4.2.3 Parametric assessment of implications of material properties on transition to Paschen’s law | 86 |
| 4.3 Conclusion | 88 |
| 5. THE IMPACT OF CATHODE SURFACE ROUGHNESS AND MULTIPLE BREAKDOWN EVENTS ON MICROSCALE GAS BREAKDOWN AT ATMOSPHERIC PRESSURE..... | 90 |
| 5.1 Introduction..... | 90 |
| 5.2 Materials and Methods..... | 91 |
| 5.2.1 Materials | 91 |
| 5.2.2 Methods | 92 |
| 5.3 Results..... | 93 |
| 5.3.1 Cathode surface changes..... | 93 |
| 5.3.2 Changes in breakdown voltage | 96 |
| 5.4 Theoretical Assessment | 102 |
| 5.5 Conclusion | 109 |
| 6. UNIFICATION OF ELECTRON EMISSION AND BREAKDOWN MECHANISM THEORIES FROM QUANTUM SCALES TO PASCHEN’S LAW | 112 |
| 6.1 Introduction..... | 112 |
| 6.2 Model Development..... | 113 |
| 6.3 Results..... | 119 |
| 6.4 Conclusion | 126 |
| 7. SCALING LAWS FOR AC GAS BREAKDOWN AND IMPLICATIONS FOR UNIVERSALITY | 129 |
| 7.1 Introduction..... | 129 |
| 7.2 Matched Asymptotic Analysis..... | 131 |

| | |
|---|-----|
| 7.3 Conclusion | 140 |
| 8. CONCLUSION..... | 142 |
| APPENDIX A. DETAILED MATCHED ASYMPTOTIC ANALYSIS OF BREAKDOWN VOLTAGE..... | 146 |
| APPENDIX B. DERIVATION OF THE MODIFIED PASCHEN MINIMUM..... | 151 |
| APPENDIX C. UNIFICATION OF ELECTRON EMISSION MODEL DERIVATION..... | 154 |
| REFERENCES | 169 |
| VITA..... | 182 |
| PUBLICATIONS..... | 188 |

LIST OF TABLES

| | |
|--|-----|
| Table 2.1. Values for A_p and B_p from Raizer (1991), and the E/p and E/N ranges for which they are valid. The E/p range is from Raizer (1991) and the E/N range is calculated from (2-2) considering room temperature Huxley et al. (1966). | 34 |
| Table 2.2 Values for A_p and B_p from Marić et al. (2005) and the corresponding E/N range. The A_p and B_p values are given with the units used in Marić et al. (2005) and converted to the units used in Table 2-1 for comparison..... | 35 |
| Table 2.3. V^* calculated from A_p and B_p from Raizer (1991) and Marić et al. (2005). | 35 |
| Table 2.4 Calculated scaling parameters from (2-4) for argon, nitrogen, neon, and xenon. | 37 |
| Table 3.1. Parameters and typical values for the model | 67 |
| Table 4.1. Summary of parameters considered in this work..... | 82 |
| Table 5.1. Average surface features before breakdown tests..... | 95 |
| Table 5.2. Depth of the observed craters at the breakdown voltage for the cathodes polished at each grit where measurable ablation occurred. | 95 |
| Table 5.3. Adjusted p-values from Tukey tests comparing breakdown voltage for 5 μm and 1 μm gaps, 10 μm and 1 μm gaps, and 10 μm and 5 μm gaps for the fifth through tenth breakdown events. Conditions undergoing a statistically significant change are denoted with *. Generally, breakdown events after the fifth event yield a statistically significant breakdown voltage between the 1 μm gap and the other gap distance while no statistical significant difference arises between the 5 μm and 10 μm gaps..... | 99 |
| Table 5.4. Average crater depth and breakdown voltage after the tenth breakdown event | 101 |
| Table 5.5. Summary of parameters used in the theoretical analysis..... | 103 |
| Table 6.1. Summary of scaling parameters used in calculations for air. | 118 |
| Table 7.1 Molecular constants summarized from (Kihara, 1952) for the gases considered in this work. | 132 |
| Table 7.2 Summary of scaling parameters for the gases considered here. | 134 |

LIST OF FIGURES

Figure 1.1. Breakdown voltage as a function of gap distance for ambient air at atmospheric pressure, with aluminum, brass, and nickel electrodes. Solid line represents Paschen’s law predictions and dotted lines represent experiment results. Reprinted with permission from Torres and Dhariwal (1999). © IOP Publishing. Reproduced with permission. All rights reserved. 18

Figure 1.2. Breakdown voltage, V_b , as a function of gap pressure, p , and gap distance, d , demonstrating the deviation from Paschen’s law at small pd . The solid line shows Paschen’s law results, the large dashes show results with a fixed gap distance of 1 cm, and the small dotted lines (showing the deviation) represent a constant pressure of 1 mmHg. Reprinted from Boyle and Kisliuk (1955), with the permission of AIP Publishing..... 20

Figure 1.3. Breakdown voltage as a function of gap distance for various electrode materials demonstrating the deviation from Paschen’s law. Reproduced from Go and Venkatraman (2014), © IOP Publishing. Reproduced with permission. All rights reserved. 22

Figure 1.4. Outline of piecemeal connections of various breakdown mechanisms, from [a] Lau et al. (1994), [b]Loveless and Garner (2016), [c]Venkatraman and Alexeenko (2012), [d] Go and Pohlman (2010), [e] Warne et al. (2003), and [f] Benilov (2009). 24

Figure 2.1. Comparison of V as a function of p for argon, nitrogen, neon, and xenon at dimensionless gap distances, d , of (a) 5×10^4 , (b) 5×10^5 , (c) 2.5×10^6 , and (d) 5×10^6 . The average percent difference in V between each of the gases is $\sim 1.6\%$, demonstrating the universality of (2-5). 38

Figure 2.2. Comparison of the standard deviation of dimensionless breakdown voltage, σV , and field enhancement factor, $\sigma\beta$, as a function of dimensionless gap distance, d , for gap distances ranging from 1-20 μm using the experimental results of (Bilici et al., 2016). Fitting the numerical solution of (2-5) to the experimental data from (Bilici et al., 2016) yielded the values of β for each gap distance..... 40

Figure 2.3. Comparison of αd as a function of p for dimensionless gap distances, d , of (a) 5×10^4 , (b) 5×10^5 , (c) 2.5×10^6 , and (d) 5×10^6 . As p increases, αd increases until $pE \approx 1$, at which point αd decreases. 42

Figure 2.4. Comparison of dimensionless breakdown voltage, V , calculated from numerically solving (2-6) as a function of dimensionless pressure, p , for various values of γSE for dimensionless gap distances, d , of (a) 5×10^4 , (b) 5×10^5 , (c) 2.5×10^6 , and (d) 5×10^6 ... 45

Figure 2.5. Comparison of dimensionless breakdown voltage, V , as a function of dimensionless pressure, p , determined from numerically solving (2-5), and calculating (2-6), (2-8), and (2-11) for (a) $d = 2.5 \times 10^6$ and $\gamma SE = 0.001$, (b) $d = 5 \times 10^6$ and $\gamma SE = 0.001$, (c) $d = 2.5 \times 10^6$ and $\gamma SE = 0.01$, and (d) $d = 5 \times 10 - 6$ and $\gamma SE = 0.01$ 47

Figure 2.6. Comparison of μ and ν as a function of dimensionless pressure, p , for $\gamma SE = 0$ and $\gamma SE = 0.1$ for dimensionless gap distances, d , of (a) 5×10^4 , (b) 5×10^5 , (c) 2.5×10^6 , and (d) 5×10^6 . Figure 6c shows that transition from field emission effects dominating to Townsend

effects dominating. For $\gamma_{SE} = 0.1$, we note that we can no longer solve for v for $p \gtrsim 10^{-6}$ in (c) and (d), due to the dominance of the Townsend avalanche and the transition to the classical Paschen law..... 48

Figure 2.7. Comparison of dimensionless breakdown voltage, V , as a function of dimensionless pressure, p , with $\gamma_{SE} = 0$ from the numerical solution of (2-5), the analytic solution of (2-6) with $\alpha d \ll 1$, the analytic solution of (2-8) with $\alpha d \gg 1$, and XPDP1 simulations at dimensionless gap distances, d , of (a) 4.5×10^4 , (b) 4.5×10^5 , (c) 2.25×10^6 , and (d) 4.5×10^6 . These dimensionless gap distances correspond to $\sim 0.1 \mu\text{m}$, $\sim 1 \mu\text{m}$, $\sim 5 \mu\text{m}$, and $\sim 10 \mu\text{m}$, respectively, for argon. 49

Figure 2.8. Percent difference in dimensionless breakdown voltage, V , from (2-6) ($\alpha d \ll 1$) and (2-8) ($\alpha d \gg 1$) compared to numerical solutions from (2-5) with $\gamma_{SE} = 0$ 51

Figure 2.9. Comparison of V from (2-5), (2-6), and (2-8) as a function of p for d of (a) 5×10^4 , (b) 5×10^5 , (c) 2.5×10^6 , and (d) 5×10^6 with $\gamma_{SE} = 0$. The pressure range is extended beyond that considered in Figure 2.6 to clearly show the matched asymptotic behavior of (2-6) and (2-8).. 52

Figure 2.10. Comparison of the critical pressure at which the minimum breakdown voltage occurs, p_c , as a function of dimensionless gap distance, d , from the numerical solution of (2-5), the numerical solution of (2-12) using (2-6) for V , the analytic solution for $\alpha d \ll 1$ given by (2-13), and the analytic solution for the Paschen regime given by (2-14)..... 54

Figure 2.11 Comparison of breakdown voltage, V , as a function of pressure, p , from the experimental results of (Ito et al., 2001), the numerical solution of (2-5), and the analytic solution of (2-11) with $\gamma_{SE} = 0.001$. The field enhancement factor, β , is used as a fitting parameter, and the values selected are displayed on the secondary vertical axes. 56

Figure 3.1. Schematic diagram of in-situ optical measurement system 61

Figure 3.2. Images of the sphere-to-sphere electrode configuration used in the experiments at (a) $10\times$, (b) $50\times$, and (c) $500\times$ magnification..... 62

Figure 3.3. (a) A set of voltage waveforms applied to the gap below the breakdown threshold. (b) Typical breakdown voltage and breakdown current waveforms compared to a typical sub-breakdown applied voltage from (a). 63

Figure 3.4. The temporal sequence of the optical and electrical processes 64

Figure 3.5. (a) Demonstration that $|\Delta_1|$ is approximately constant in the relevant gap width regime (b) Relative contributions of field emission and Townsend avalanche, given by μ and ν , respectively, showing that field emission dominates until the gap width is $\sim 10 \mu\text{m}$ 69

Figure 3.6. (a) Measured breakdown voltage and electric field as a function of gap width, the error bars represent the standard deviation of the measured breakdown voltage. (b) Comparison of measured breakdown voltage, matched asymptotic prediction of breakdown voltage using (3-1), simplified equation for breakdown voltage using (3-8), and universal Paschen's law using (3-9) with the fitted field enhancement factor, β , used in (3-1) and (3-8) as a function of gap width. . 71

Figure 3.7. Breakdown morphology at gap widths from $1 \mu\text{m}$ - $20 \mu\text{m}$. (a)-(c) show the breakdown propagating along the shortest path with luminescence filling the surrounding area, (d)-(f) show

the roughly constant path lengths regardless of gap width which is consistent with the plateau of breakdown voltage in this region, and (g)-(i) indicate no obvious breakdown channel arising at these smallest gap distances. 73

Figure 3.8. The effective lengths of breakdown path for various gap widths 73

Figure 3.9. The physical process unifying Townsend avalanche and field emission for microscale breakdown for (a) $d > 10 \mu\text{m}$, (b) $d = 5 \mu\text{m} - 10 \mu\text{m}$, (c) $d = 1 \mu\text{m} - 5 \mu\text{m}$ 76

Figure 4.1. Measured breakdown voltage (V_B) as a function of gap distance (d) for pressures (p) of 3 kPa, 50 kPa, and 101 kPa. 80

Figure 4.2. (a) Dimensionless breakdown voltage, V , as a function of the product of dimensionless pressure and gap distance, pd , for various pressures compared to results from the universal Paschen's law (UPL) determined from (4-2) with $\gamma SE = 10 - 5$ using β from Figure 4.3. The symbols represent experimental data points and the dashed lines represent the numerical solution of (4-1), using field enhancement factor β as a fitting parameter. (b) Dimensionless breakdown voltage, V , as a function of dimensionless gap distance, d . Numerical results from (4-1) are shown as the dashed lines and the limiting results of equation (4-5) are shown as symbols with $\gamma SE = 10 - 5$ using β from Figure 4.3. There is an average percent difference between equations (4-1) and (4-5) of 3.71%. 85

Figure 4.3. (a) Field enhancement factor, β , as a function of the product of the dimensionless pressure and gap distance, pd , obtained by fitting the experimental data from Figure 4.2. (b) Field enhancement factor, β , as a function of the dimensionless electric field, E 86

Figure 4.4. The ratio of the product of dimensionless pressure and gap distance, pd , causing the transition to Paschen's law, pd_{int} , to pd corresponding to the Paschen minimum, $pd_{PL, min}$, as a function of p for various values of (a) ϕ with $\beta = 60$ and $\gamma SE = 10 - 6$, and (b) β with $\gamma SE = 10 - 6$ and $\phi = 0.0465$. Figure (a) highlights that It is important to note that note that ϕ does not have a significant effect on the transition point until $p \approx 2 \times 10 - 6$ (which corresponds to 380 Torr), and β does not influence the transition point until $p \approx 5 \times 10 - 6$ (950 Torr). 88

Figure 5.1. Schematic of the xperimental setup showing the micromanipulator and pin mounting blocks. 91

Figure 5.2. Atomic force microscopy (AFM) measurements of the 800 grit cathode prior to experiments showing the average surface features (a) Optical image of the surface visually showing the surface roughness. (b) Contour mapping of surface height along the surface. (c) AFM arm deflection showing height and depth of the surface features. 94

Figure 5.3. Representative voltage (solid) and current (dashed) waveforms for a $5 \pm 0.5 \mu\text{m}$ gap with the cathode polished using 800 grit for (a) a single breakdown event and (b) the tenth breakdown event. All breakdown events exhibited similar characteristics. 97

Figure 5.4. Breakdown voltage as a function of number of breakdown events for three individual trials for (a) 400 grit (b) 800 grit and (c) 1200 grit samples at 1 μm gap distance. 97

Figure 5.5. Breakdown voltage as a function of number of breakdown events for three individual trials for (a) 400 grit (b) 800 grit and (c) 1200 grit samples at 5 μm gap distance. 98

Figure 5.6. Breakdown voltage as a function of number of breakdown events for three individual trials for (a) 400 grit (b) 800 grit and (c) 1200 grit polished cathodes at 10 μm gap distance. 98

Figure 5.7. Average breakdown voltage as a function of number of breakdown events for (a) 400 grit (b) 800 grit and (c) 1200 grit for three trials each. 101

Figure 5.8. Average breakdown voltage, V , as a function of effective gap distance, $d_{\text{eff}} = d + \delta$, where d is the anode-cathode gap and δ is the breakdown induced crater depth, compared to numerical results from (5-1) and analytic results from (5-2). The product of the ionization coefficient and effective gap distance, αd_{eff} , is displayed on the secondary vertical axis as a function of d_{eff} . The largest two gap distance points have $\alpha d_{\text{eff}} \gg 18$, which exceeds Meek's criterion for streamer formation. 105

Figure 5.9. (a) Field enhancement factor, β , as a function of effective gap distance, $d_{\text{eff}} = d + \delta$, where d is the gap distance and δ is the crater depth, showing that β is approximately linear until the larger gap distances corresponding to the transition to Townsend avalanche, where it becomes constant. (b) The ratio of the field emission component to the Townsend component, $\mu\nu$, as a function of d_{eff} , demonstrating that field emission effects govern breakdown until $d_{\text{eff}} \approx 10 \mu\text{m}$, which corresponds to $\alpha d_{\text{eff}} \approx 10$. This point coincides with the transition of β from linear to constant in (a), indicating the transition to the traditional Paschen's law. 106

Figure 5.10. (a) Breakdown voltage, V , as a function of effective gap distance, $d_{\text{eff}} = d + \delta$, where d is the gap distance and δ is the crater depth, from the experimental data, the numerical results of (5-1), and the analytic results of (5-3) assuming $\gamma SE = 1.5 \times 10^{-3}$. The product of the ionization coefficient and effective gap distance, αd_{eff} , is shown on the secondary vertical axis. The transition to Paschen's law occurs for $\alpha d_{\text{eff}} \approx 10$ and breakdown becomes driven by streamer formation when $\alpha d_{\text{eff}} > 18$ 107

Figure 5.11. The product of the ionization coefficient and effective gap distance, αd_{eff} , as a function of the effective gap distance, $d_{\text{eff}} = d + \delta$, where d is the gap distance and δ is the crater depth. Each pair of symbols shows the αd_{eff} value after the first and tenth breakdown events, showing that crater formation can push breakdown behavior past the $\alpha d_{\text{eff}} \approx 10$ criterion for transition to Paschen's law. 108

Figure 6.1. Summary of emission mechanisms from nanoscale to microscale with [1] Venkattraman & Alexeenko, 2012); [2] Lau, Liu, & Parker, 1994); [3] Go & Pohlman, 2010; [4] Warne, Jorgenson, & Nicolaysen, 2003; [5] Benilov, 2009; [6] Loveless & Garner, 2017b; [7] Lau et al., 1991; and [8] Darr, Loveless, & Garner, 2019. 113

Figure 6.2. Dimensionless breakdown voltage, V , as a function of the product of dimensionless pressure and gap distance, pd , for various gases with $\gamma SE = 10^{-3}$, calculated with the dimensionless PL using (6-14). One material parameter remains in (6-14), preventing it from being universal (true for any gas). 120

Figure 6.3. Dimensionless breakdown voltage, V , as a function of dimensionless gap distance, d , for various dimensionless pressures, p , calculated with (6-14) for nitrogen considering $\gamma SE = 10^{-3}$. Increasing p shifts the minimum to the left. 121

Figure 6.4. Dimensionless breakdown voltage, V , as a function of dimensionless gap distance, d , for dimensionless pressures of (a) $p = 3.18 \times 10^{-4}$ and (b) $p = 1.59 \times 10^{-4}$, using the exact (6-13), analytic (C54), and limiting equation (C55) for microscale and PL (6-14) with nitrogen considering $\gamma SE = 10 - 3$. The transition from microscale breakdown to the traditional PL can occur to either the left or the right of the Paschen minimum depending on one's pressure. 122

Figure 6.5. Dimensionless current density J as a function of dimensionless breakdown voltage V demonstrating the transitions of the exact solution between CSCL, FN, and MG, and showing the implications of increasing mobility on those transitions for a 10 nm gap. 123

Figure 6.6. Dimensionless current density J as a function of dimensionless breakdown voltage V for a 10 nm gap demonstrating the transitions of the exact solution between QSCL, CSCL, FN, and MG focusing on (a) the transition from QSCL to CSCL and (b) the full spectrum of transitions. 124

Figure 6.7. Dimensionless breakdown voltage, V , as a function of dimensionless gap distance, d , demonstrating the respective regions where each emission mechanism should dominate for dimensionless mobilities of (a) $\mu = 1000$ and (b) $\mu = 500$ 125

Figure 7.1 Comparison of dimensionless breakdown voltage, V , from (7-3) as a function of dimensionless pressure, P , at a dimensionless gap distance of $L = 1000$ for different values of dimensionless angular frequency, ω , for hydrogen, nitrogen, argon, and helium. At large P , V becomes independent of gas, or universal. 134

Figure 7.2 Comparison of dimensionless breakdown voltage, V , as a function of dimensionless pressure, P , for various values of $\omega \approx 0.1$ and $L \approx 5000$ for hydrogen, from [a] the exact, dimensionless equation for MW breakdown given by (7-3), [b] the $P \gg \omega$ limit given by (7-4), [c] the $P \ll \omega$ limit given by (7-5), and [d] experimental data (Lisovskiĭ, 1999). 135

Figure 7.3 Comparison of RF-induced dimensionless breakdown voltage, V , as a function of dimensionless pressure, P , for $\omega = 4.2 \times 10^{-4}$ and $L \approx$ (a) 4000 and (b) 2500 for hydrogen, from [a] the numerical solution of (7-6), [b] the analytic solution valid to the right of the minimum given by the negative root of (7-7), [c] the limit valid to the right of the minimum given by (7-9), [d] the analytic solution valid to the left of the minimum given by the positive root of (7-7), [e] the limit valid to the left of the minimum given by (7-8), and [f] experimental data from (Lisovskiy et al., 2006) 137

Figure 7.4 Transition from RF to MW dimensionless breakdown voltage, V , in hydrogen as a function of dimensionless angular frequency, ω , at a gap distance of 1 cm determined using [a] the full MW equation from (7-3), [b] the $P \gg \omega$ limit given by (7-4), [c] the $P \ll \omega$ limit given by (7-5), [d] the numerical solution of the RF equation from (7-6), and [e] the analytic RF solution of (7-7). 138

Figure 7.5 Dimensionless breakdown voltage, V , as a function of dimensionless pressure, P , for hydrogen for $L = 2000$ from [a] Paschen's law given by (7-11) assuming $\gamma = 0.1$, [b] the numerical solution of (7-6) assuming $\omega = 0.0002$, and [c] the solution of (7-3) considering $\omega = 0.002$. Additionally, the ratio of the results from Paschen's law from [a] and the numerical results from [b] are plotted on the secondary vertical axis. 140

ABSTRACT

As electronic device dimensions decrease to micro and nanoscale, Paschen's law (PL)—the standard theory used to predict breakdown voltage (V_b) governed by Townsend avalanche (TA)—fails due to ion-enhanced field emission (FE). Analytic models to predict V_b at these scales are necessary to elucidate the underlying physics driving breakdown and electron emission in these regimes. Starting from a previously-derived breakdown criterion coupling TA and FE, this dissertation derives a universal (true for any gas) breakdown equation. Further simplifying this equation using a matched asymptotic analysis, dependent on the product of the ionization coefficient and the gap distance, yields an analytic theory for dimensionless V_b . This analytic model unifies the coupled FE/TA regime to a universal PL derived by applying scaling parameters to the standard PL. This model enables parametric analyses to assess the effects of different parameters (such as pressure, gap distance, and field enhancement factor) on breakdown and quantify the relative contribution of FE and TA to identify the transition to the universal PL. This dissertation applies this general theory to experimental cases of different gap width, gap pressure and electrode surface roughness before exploring unification across electron emission regimes, validation with molecular dynamics simulations, and extensions to alternating current (AC).

One application of this theory to experimental data used data from a collaborator at Xi'an Jiaotong University, who used an electrical-optical measurement system to measure the breakdown voltage and determine breakdown morphology as a function of gap width. An empirical fit showed that the breakdown voltage varied linearly with gap distance at smaller gaps as in vacuum breakdown. This dissertation demonstrates that applying the matched asymptotic theory in the appropriate limits recovers this scaling with the slope as a function of field emission properties.

Pressure also plays a critical role in gas breakdown behavior. This dissertation derives a new analytic equation that predicts breakdown voltage V_b within 4% of the exact numerical results of the exact theory and new experimental results at subatmospheric pressure for gap distances from 1-25 μm . At atmospheric pressure, V_b transitions to PL near the product of pressure and gap distance, pd , corresponding to the Paschen minimum; at lower pressures, the transition to PL

occurs to the left of the minimum. We further show that the work function plays a major role in determining whether V_b transitions from the coupled FE/TA equation back to the traditional PL to the right or the left of the Paschen minimum as pressure increases, while field enhancement and the secondary emission coefficient play smaller roles. These results indicate that appropriate combinations of these parameters cause V_b to transition to PL to the left of the Paschen minimum, which would yield an extended plateau similar to some microscale gas breakdown experimental observations.

Finally, the importance of electrode surface structure on microscale gas breakdown remains poorly understood. This dissertation provides the next step at assessing this by applying the asymptotic theory to microscale gas breakdown measurements for a pin-to-plate electrode setup in air at atmospheric pressure with different cathode surface roughness. Multiple discharges created circular craters on the flat cathode up to 40 μm deep with more pronounced craters created at smaller gap sizes and greater cathode surface roughness. The theory showed that breakdown voltage and ionization coefficient for subsequent breakdown events followed our earlier breakdown theory when we replaced the gap distance d with an effective gap distance d_{eff} defined as the sum of cathode placement distance and crater depth. Moreover, the theory indicated that d_{eff} could become sufficiently large to exceed the Meek criterion for streamer formation, motivating future studies to assess whether the cathode damage could drive changes in the breakdown mechanism for a single electrode separation distance or the Meek criterion requires modification at microscale.

We next unified field emission with other electron emission mechanisms, including Mott-Gurney (MG), Child-Langmuir (CL), and quantum space-charge-limited current (QSCL) to develop a common framework for characterizing electron emission from nanoscale to the classical PL. This approach reproduced the conditions for transitions across multiple mechanisms, such as QSCL to CL, CL to FE, CL to MG to FE, and microscale gas breakdown to PL using a common nondimensional framework. Furthermore, we demonstrated the conditions for more complicated nexuses where multiple asymptotic solutions matched, such as matching QSCL, CSCL, MG, and FE to gas breakdown. A unified model for radiofrequency and microwave gas breakdown will be compared to experimental results from Purdue University to elucidate breakdown mechanism.

The results from this dissertation will have applications in microscale gas breakdown for applications including microelectromechanical system design, combustion, environmental mitigation, carbon nanotube emission for directed energy systems, and characterizing breakdown in accelerators and fusion devices.

1. INTRODUCTION

Reprinted in part from Loveless, A. M. (2017) *General Gas Breakdown Theory from Microscale to the Classical Paschen Law*, M. S. Thesis, Purdue University.

1.1 Background

This dissertation is a continuation of a previous M. S. Thesis. Therefore, the background given in Section 1.1 and 1.2 is reproduced here from (Loveless, 2017).

Gas breakdown in the presence of a high voltage is a classical problem typically described by Paschen's law, given by (Paschen, 1889)

$$V_b = \frac{Bpd}{\{\ln(Apd) - \ln[\ln(1 + \gamma_{SE}^{-1})]\}} \quad (1-1)$$

where p is gap pressure, d is electrode gap distance, A and B are material constants, and γ_{SE} is the secondary electron emission coefficient. Paschen's law (PL), which has served as the standard for calculating V_b since its initial derivation in the late 1800s, calculates breakdown by considering Townsend effects, or electron avalanches, as the driving breakdown mechanism (Raizer, 1991; Paschen, 1889). Thus, PL calculates V_b as a function of pd , as shown in (1-1).

Figure 1.1 shows that PL predicts a minimum V_b , such that V_b increases for either higher or lower pd . One can determine pd at which this minimum occurs by taking the derivative of V_b from (1-1) and setting it equal to zero to obtain

$$\ln[Apd] - \ln[\ln(1 + \gamma_{SE}^{-1})] - 1 = 0. \quad (1-2)$$

Then, solving (1-2) for the critical pd , or $(pd)_c$ yields

$$(pd)_c = \frac{\exp(1)}{A} \ln(1 + \gamma_{SE}^{-1}), \quad (1-3)$$

which gives the minimum V_b . Figure 1 shows V_b as a function of pd for air at atmospheric pressure. At small pd , PL (the solid line in Figure 1.1) predicts that V_b increases sharply because too many electrons reach the anode before causing sufficient ionizations for avalanche formation. This does not occur experimentally for gaps below approximately 15 μm (Go & Venkatraman, 2014; Go & Pohlman, 2010), as demonstrated by the dotted lines in Figure 1.1. Instead, V_b deviates from PL and continues decreasing with decreasing pd (Go & Venkatraman, 2014).

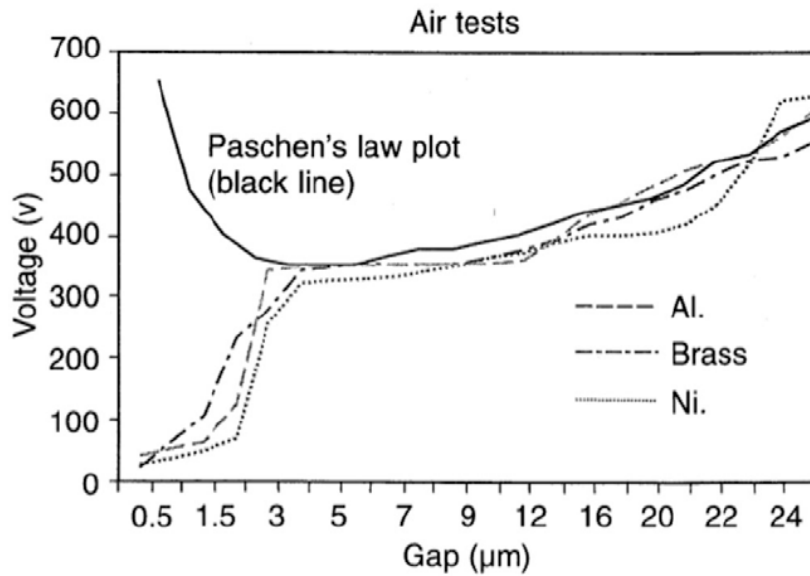


Figure 1.1. Breakdown voltage as a function of gap distance for ambient air at atmospheric pressure, with aluminum, brass, and nickel electrodes. Solid line represents Paschen's law

predictions and dotted lines represent experiment results. Reprinted with permission from Torres and Dhariwal (1999). © IOP Publishing. Reproduced with permission. All rights reserved.

The trend of decreasing electronic device dimensions requires more robust methods for accurately predicting breakdown voltage, V_b . Correctly predicting V_b for microelectromechanical systems (MEMS), such as pressure sensors (Abeysinghe et al., 2001; Kottapalli et al., 2012), prevents unwanted discharges from destroying sensitive devices. Alternatively, emerging research areas, such as microplasmas (Mahamud & Farouk, 2016; Handa & Minamitani, 2009; Chang et al., 2016) and electric micropropulsion systems (Wright & Ferrer, 2015; Tholeti et al., 2016), require accurate V_b predictions for optimal system design. Thus, accurately predicting V_b at microscale is a necessity.

The deviation from PL at microscale has been explained by field emission, or a tunneling effect where a strong electric field lowers the potential barrier of the cathode, releasing electrons into the system (Go & Venkatraman, 2014; Fowler & Nordheim, 1928). The combination of collisional effects and field emission generates a sufficient current to induce breakdown at lower voltages, leading to the deviation from Paschen's curve first noted by Boyle and Kisliuk (1955). Figure 1.2 shows the initial results from Boyle and Kisliuk demonstrating the failure of Paschen's law at small pd . Thus, PL fails when Townsend effects do not drive breakdown, such as at high pressures and large gap distances, where the electron avalanche causes a high space charge field resulting in streamer formation, or at vacuum, where large electron avalanches cannot form due to insufficient gas density (Go & Venkatraman, 2014).

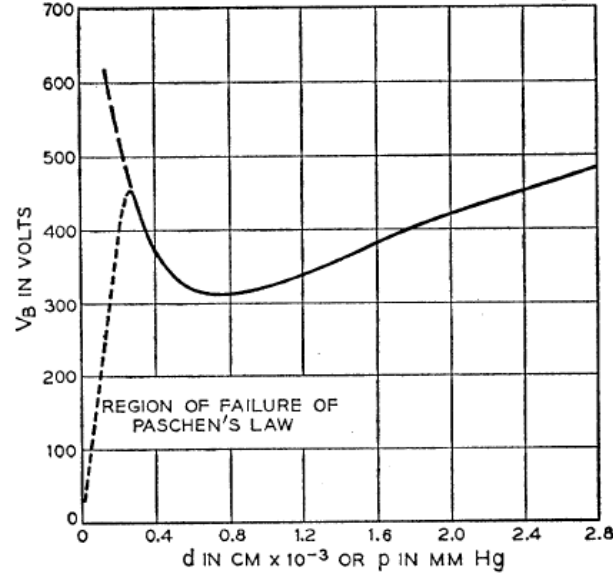


Figure 1.2. Breakdown voltage, V_b , as a function of gap pressure, p , and gap distance, d , demonstrating the deviation from Paschen's law at small pd . The solid line shows Paschen's law results, the large dashes show results with a fixed gap distance of 1 cm, and the small dotted lines (showing the deviation) represent a constant pressure of 1 mmHg. Reprinted from Boyle and Kisliuk (1955), with the permission of AIP Publishing.

Numerous studies (Go & Venkatraman, 2014; Radmilović-Radjenović & Radjenović, 2008a; Radmilović-Radjenović & Radjenović, 2007; Loveless & Garner, 2016; Loveless & Garner, 2017; Venkatraman & Alexeenko, 2012; Go & Pohlman, 2010; Tirumala & Go, 2010; Torres & Dhariwal, 1999; Dhariwal et al., 2000; Chen et al., 2006), have modeled microscale breakdown either empirically or from first principles. Several recent derivations (Go & Venkatraman, 2014; Venkatraman & Alexeenko, 2012; Go & Pohlman, 2010; Venkatraman et al., 2012b) have started from the traditional condition for Townsend avalanche, given by $\gamma_{SE}[\exp(\alpha d) - 1] = 1$ (Venkatraman & Alexeenko, 2012; Go & Pohlman, 2010), where α is the ionization coefficient in the gas, and incorporated ion-enhanced field emission as another current by recasting the secondary emission coefficient as $\gamma_{SE} + \gamma'$. This additional contribution by ion-enhanced field emission, γ' , drives breakdown voltages below those predicted by PL for microscale gaps. These

studies demonstrated that one recovers the traditional condition for Townsend avalanche by sufficiently increasing the gap distance at a given pressure (usually atmospheric pressure) (Venkatraman & Alexeenko, 2012; Go & Pohlman, 2010). Alternatively, sufficiently large gap distances can lead to point discharges, or streamers (Montijn & Ebert, 2006; Leob & Meek, 1941), which the classical PL also does not consider. Streamers occur when the product of the ionization coefficient, α , and the gap distance, d , exceeds Meek's criterion ($\alpha d \approx 18$ for air at atmospheric pressure) (Montijn & Ebert, 2006; Loeb & Meek, 1941).

Many other studies have since experimentally analyzed breakdown behavior for microscale gaps (Go & Venkatraman, 2014; Radmilović-Radjenović et al., 2014; Radmilović-Radjenović & Radjenović, 2008a; Radmilović-Radjenović & Radjenović, 2007) with various electrode configurations, pressures, and gases. Figure 1.3 highlights experimental results for breakdown voltage with various electrode materials, demonstrating the deviation from PL (Go & Venkatraman, 2014). Depending upon the gas and electrodes, some experiments showed that breakdown voltage continued to decrease with decreasing gap distance (Dhariwal et al., 2007) while others showed an extended plateau (Bilici et al., 2016; Klas et al., 2012; Radmilović-Radjenović et al., 2014).

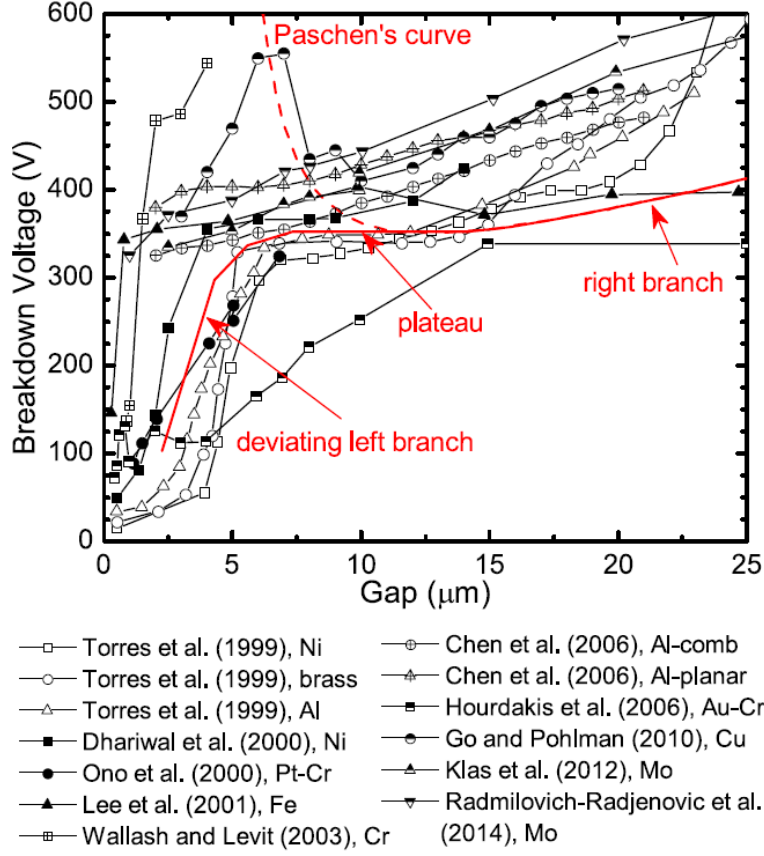


Figure 1.3. Breakdown voltage as a function of gap distance for various electrode materials demonstrating the deviation from Paschen's law. Reproduced from Go and Venkatraman (2014), © IOP Publishing. Reproduced with permission. All rights reserved.

For example, Radmilović-Radjenović and Radjenović (2008a) derived a breakdown condition coupling field emission with Townsend discharge, given by

$$V_b = \frac{d(D_{FN} + Bp)}{\ln(ApdK)}, \quad (1-4)$$

where d is the gap distance, A and B are gas-dependent constants, D_{FN} is a Fowler-Nordheim constant, and K is a material and gas-dependent constant. While the results from this equation match simulation and experimental results, the fact that K is essentially a fitting parameter prevents

(1-4) from offering truly predictive results, and masks the underlying physics in the system. Additionally, Li et al. (2013) derived a coupled breakdown equation given by

$$V_b = \frac{D^2pd}{\{\ln(pd) + \ln[C/\ln(\gamma_i^{-1} + 1)]\}^2}, \quad (1-5)$$

where p is pressure, d is gap distance, C and D are gas-dependent constants, and γ_i is the ion-enhanced field emission coefficient, representing the inverse of the number of ions produced by a single electron. The breakdown condition given by (1-5) and subsequent simulations show that ion-enhanced field emission leads to a deviation from Paschen's curve, resulting in the modified Paschen's curve. This work highlights the importance of fully understanding how field emission affects discharge (Li et al., 2013).

While these microscale breakdown models successfully capture the fundamental physics involved, they are generally solved numerically, which prohibits fully assessing critical limiting behavior, such as the transitional behavior as gap distance continues to decrease, or quantifying the transition from field emission dominated breakdown to Townsend avalanche and the classical PL at microscale. Such transitions become important physically when designing and constructing microscale systems in a practical or industrial environment where one may not want (or even have easy capability) to develop codes, or may not have access to commercial software to numerically solve the equations for their specific cases.

One may also ultimately extend a model coupling field emission and Townsend breakdown to other electron emission and breakdown regimes, as shown schematically in Figure 1.4. Several

studies have explored transitions between these mechanisms piecemeal, such as relating the Child-Langmuir (CL) law for space-charge limited flow at vacuum (Child, 1911; Langmuir, 1913) to the Mott-Gurney law for space-charge limited flow at general pressure (Benilov, 2000) with a single model with increasing pressure (Benilov, 2009). Others have related the CL law to field emission with increasing voltage (Lau et al., 1994; Ragan-Kelley et al., 2009; Jensen, 2003) and Townsend breakdown to streamer theory at increasing pressures and gap distances (Warne et al., 2003). Figure 1.4 depicts a general framework to unify the relevant electron emission and breakdown regimes.

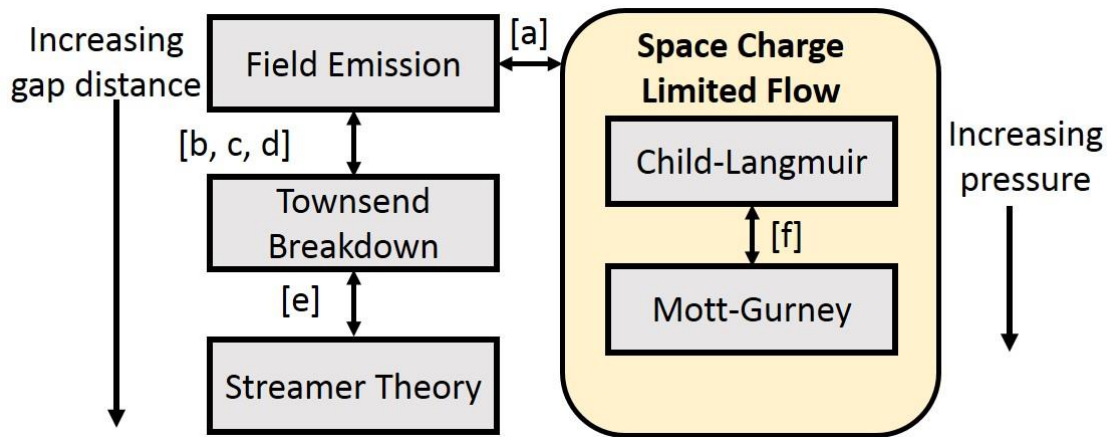


Figure 1.4. Outline of piecemeal connections of various breakdown mechanisms, from [a] Lau et al. (1994), [b]Loveless and Garner (2016), [c]Venkatraman and Alexeenko (2012), [d] Go and Pohlman (2010), [e] Warne et al. (2003), and [f] Benilov (2009).

1.2 Derivation of Breakdown Condition

This dissertation first takes a breakdown parameter coupling field emission and Townsend breakdown derived by Venkatraman and Alexeenko (2012) and derives analytic breakdown voltage equations for various conditions. This section will detail the derivation of the initial breakdown parameter.

To derive a breakdown condition coupling field emission and Townsend breakdown, we begin with the Townsend avalanche criterion given by (Paschen, 1889)

$$\gamma_{SE}[\exp(\alpha d) - 1] = 1, \quad (1-6)$$

where $\alpha = A_p p \exp(-B_p p/E)$ is the ionization coefficient corresponding to the number of ions produced per electron in a given length, p is the gas pressure, E is the electric field, and A_p and B_p are material-dependent constants, and γ_{SE} is the secondary emission coefficient quantifying the probability of electron emission when ions strike the cathode. Field emission is coupled to Townsend breakdown through the Fowler-Nordheim current (Fowler & Nordheim, 1928), which relates the current density of field emitted electrons to the electric field through

$$j_{FN} = C_{FN} E^2 \exp(-D_{FN}/E), \quad (1-7)$$

where $C_{FN} = A_{FN} \beta^2 \exp[(3.79 \times 10^{-4})^2 B_{FN} / \phi^{1/2}] / [\phi t^2(y)]$, β is the field enhancement factor, ϕ is the work function of the cathode, $t^2(y) \approx 1.1$ is a correction factor, and A_{FN} and B_{FN} are constants.

First, (1-6) is modified to include field emission induced ion enhancement by

$$(\gamma_{SE} + \gamma')[\exp(\alpha d) - 1] = 1, \quad (1-8)$$

where γ' is the ion-enhancement coefficient incorporating field emission enhancement from positive space charge. Noting that positive space charge will increase the electric field by some amount $E^+ \ll E$, we can rewrite (1-7) as

$$j'_{FN} = C_{FN}(E + E^+)^2 \exp[-D_{FN}/(E + E^+)]. \quad (1-9)$$

Expanding (1-9) gives

$$j'_{FN} = C_{FN}E^2 \left(1 + \frac{2E^+}{E}\right) \exp\left(\frac{D_{FN}E^+}{E^2}\right) \exp\left(-\frac{D_{FN}}{E}\right). \quad (1-10)$$

Next, we define the steady-state current density as

$$j_{tot} = \frac{j_0 \exp(\alpha d)}{\{1 - \gamma_{SE}[\exp(\alpha d) - 1]\}}, \quad (1-11)$$

where j_0 is the current density at the cathode. Substituting (1-9) into (1-11) for j_0 yields a steady-state current density coupling field emission effects with Townsend effects, given by

$$j_{tot} = j_{FN} \left(1 + \frac{2E^+}{E}\right) \exp\left(\frac{D_{FN}E^+}{E^2}\right) \frac{\exp(\alpha d)}{\{1 - \gamma_{SE}[\exp(\alpha d) - 1]\}}. \quad (1-12)$$

Alternatively, we note that γ_{SE} will increase by an amount γ' with the inclusion of field emission effects, and rewrite (1-11) as

$$j_{tot} = \frac{j_{FN} \exp(\alpha d)}{\{1 - (\gamma_{SE} + \gamma')[\exp(\alpha d) - 1]\}} \quad (1-13)$$

Solving (1-13) for γ' and substituting (1-12) for j_{tot} yields

$$\gamma' = \frac{1 - \{1 - \gamma_{SE}[\exp(\alpha d) - 1]\} \exp(-D_{FN} E^+ / E^2)}{(1 + 2E^+ / E)[\exp(\alpha d) - 1]} - \gamma_{SE}. \quad (1-14)$$

The only unknown in (1-12)-(1-14) is E^+ . To obtain an expression for E^+ , we begin with Poisson's equation

$$\frac{dE}{dx} = \frac{\rho}{\epsilon_0}, \quad (1-15)$$

where ρ is the charge density and ϵ_0 is the permittivity of free space. Assuming the nominal electric field occurs at the center of the gap and a constant charge density between the cathode and the center of the gap allows us to solve (1-15) as

$$\int_E^{E+E^+} dE = \int_0^{d/2} \frac{\rho}{\epsilon_0} dx = E^+ = \frac{\rho d}{2\epsilon_0}, \quad (1-16)$$

where d is the distance from the cathode. Additionally, the charge density can be related to the ion current density and the drift velocity by

$$\rho = \frac{j_{ion}}{v_d}, \quad (1-17)$$

where j_{ion} is the ion current density and v_d is the drift velocity. We can also relate the ion current density to the total current density through

$$j_{ion} = \frac{j_{tot}[\exp(\alpha d) - 1]}{\exp(\alpha d)}. \quad (1-18)$$

Then, substituting (1-12) for j_{tot} gives the ion current density as

$$j_{ion} = j_{FN} \left(1 + \frac{2E^+}{E}\right) \exp\left(\frac{D_{FN}E^+}{E^2}\right) \frac{[\exp(\alpha d) - 1]}{\{1 - \gamma_{SE}[\exp(\alpha d) - 1]\}}. \quad (1-19)$$

We then substitute (1-17) into (1-16) for the charge density, and insert (1-18) for j_{ion} into the resulting equation to obtain an expression for the increase in electric field due to field emission as

$$E^+ = \frac{j_{FN}d(1 + 2E^+/E)\exp(D_{FN}E^+/E^2)}{2v_d\varepsilon_0} \frac{[\exp(\alpha d) - 1]}{\{1 - \gamma_{SE}[\exp(\alpha d) - 1]\}}. \quad (1-20)$$

Multiplying both sides of (1-20) by D_{FN}/E^2 , defining $x = D_{FN}E^+/E^2$, and setting $\bar{E} = E/D_{FN}$ yields

$$x = \frac{D_{FN}dj_{FN}}{2E^2v_d\varepsilon_0} \frac{[\exp(\alpha d) - 1]}{\{1 - \gamma_{SE}[\exp(\alpha d) - 1]\}} (1 + 2\bar{E}x)\exp(x). \quad (1-21)$$

Rearranging yields a breakdown parameter for coupled field emission and Townsend discharge given by

$$\frac{\exp(x) (1 + 2\bar{E}x)}{F_{br}x} = 1, \quad (1-22)$$

where

$$F_{br} = \frac{2E^2 v_d \epsilon_0 \{1 - \gamma_{SE} [\exp(\alpha d) - 1]\}}{D_{FN} dj_{FN} [\exp(\alpha d) - 1]}. \quad (1-23)$$

Breakdown will occur when a pre-breakdown steady-state exists for the microdischarge, or when $f(x) = \exp(x) (1 + 2\bar{E}x)/F_{br}x$, is minimized. Taking the derivative of $f(x)$ and setting it equal to zero yields

$$2\bar{E}x + x - 1 = 0, \quad (1-24)$$

which can be solved for x to obtain

$$x = x_0 = \frac{-1 + \sqrt{1 + 8\bar{E}}}{4\bar{E}}. \quad (1-25)$$

Thus, breakdown occurs when $f(x_0) = 1$.

Rearranging (1-22) to isolate F_{br} and setting $x = x_0$ yields

$$F_{br} = \frac{2E^2 v_d \epsilon_0 \{1 - \gamma_{SE} [\exp(\alpha d) - 1]\}}{D_{FN} dj_{FN} [\exp(\alpha d) - 1]} = \frac{\exp(x_0) (1 + 2\bar{E}x_0)}{x_0}, \quad (1-26)$$

which is a breakdown condition incorporating both field emission and Townsend effects. Numerically solving (1-26) for a specified gap distance and pressure gives the electric field required for breakdown to occur.

While (1-26) gives a breakdown condition coupling field emission to Townsend discharge, it must be solved numerically. Developing analytic expressions for breakdown voltage will elucidate the underlying physics occurring in different regimes and allow for an assessment of breakdown behavior at critical limits. For example, quantifying the point where breakdown transitions from fully field emission driven to coupled field emission and Townsend discharge driven is important for microscale system design. As such, it provides the first step toward developing the capability to predict breakdown voltage for any pressure, gap distance, and gas *a priori*, rather than requiring extensive simulations, numerical solutions, or experimental data.

1.3 Scope of Dissertation

This dissertation derives analytic solutions to the condition for microscale gas breakdown, applies it to various experimental conditions, relates it space-charge-limited conditions at nanoscale, and demonstrates how the approach may be applied to AC and radiofrequency (RF) electric fields.

Chapter 2 presents the derivation of a universal model for gas breakdown theory from microscale to the classical Paschen's law generalized for gas, pressure, and gap distance provided the system remains in the field emission/Townsend avalanche driven regime (Loveless & Garner, 2017b). Chapter 3 utilizes the model derived in Chapter 2 to assess experimental data and demonstrate the regions where field emission and Townsend avalanche drive breakdown (Meng et al., 2018). Chapter 4 uses similar techniques to assess experimental data obtained from a collaborator to identify the transition to Paschen's law based on pressure (Loveless et al., 2019). Chapter 5 details the experimental process to obtain breakdown data, focusing on surface roughness affecting breakdown voltage and applying the theory developed in Chapter 2 (Brayfield et al., 2019). Chapter 6 extends the model developed in Chapter 2 down to nanoscale, incorporating some of the various mechanisms discussed in Figure 1.1 and presents relevant results. Finally, Chapter 7 discusses a dimensionless model developed for AC gas breakdown (Loveless & Garner, 2017c). Concluding remarks are made in Chapter 8.

2. A UNIVERSAL THEORY FOR GAS BREAKDOWN FROM MICROSCALE TO THE CLASSICAL PASCHEN LAW

Reprinted from Loveless, A. M. and Garner, A. L. (2017) A universal theory for gas breakdown from microscale to the classical Paschen law. *Physics of Plasmas*, 24, 113522, with the permission of AIP Publishing.

2.1 Introduction

As mentioned previously, the discrepancy between Paschen's law predictions and experimental data (Go & Venkatraman, 2014; Boyle & Kisliuk, 1955) motivates this work. This chapter details the development of a single unified, universal model for breakdown for classical length scales from the ion-enhanced field emission dominated regime [$\lesssim 1 \mu\text{m}$ at atmospheric pressure (Loveless & Garner, 2017a)] through the combined field emission and Townsend regime [$\sim O(10 \mu\text{m})$ at atmospheric pressure (Loveless & Garner, 2017a)], to the point where we recover the classical Paschen law for *any pressure*. This chapter extends previous work (Loveless, 2017) by modifying the scaling parameters to better assess the transition between breakdown mechanisms. In Section 2.2 we derive analytic expressions that are universal for any gas that can readily be calculated for designing and assessing the behavior of systems ranging from microscale at higher pressures (\sim atmospheric) to larger gaps at lower pressures, which are more characteristic of Paschen's law. Section 2.2 compares the numerical and analytic results from the matched asymptotic analysis to results from the dimensionless Paschen's law and simulation results, while also demonstrating the independent contributions of field emission and Townsend effects. Section 2.3 outlines the derivation of the modified Paschen minimum. We make concluding remarks in Section 2.4. This chapter was published in Loveless and Garner (2017a).

2.2 Matched Asymptotic Analysis

2.2.1 Dimensionless breakdown voltage equation

Incorporating ion-enhanced field emission into the Fowler-Nordheim current density and the resulting increase of electric field due to positive space charge into Poisson's equation yields a breakdown condition given by (Venkatraman & Alexeenko, 2012)

$$\frac{2v_d\epsilon_0E^2\{1 - \gamma_{SE}[\exp(\alpha d) - 1]\}}{D_{FN}j_{fn}d[\exp(\alpha d) - 1]} = \frac{\exp(x_0)(1 + 2\bar{E}x_0)}{x_0}, \quad (2-1)$$

where E is the electric field required for breakdown, $v_d = [(2ekT_gE)/(\pi mp\sigma_{CE})]^{1/2}$ is the ion drift velocity, ϵ_0 is the permittivity of free space, k is Boltzmann's constant, T_g is the temperature of the gas, m is the mass of the gas, p is the pressure, σ_{CE} is the charge exchange cross section, γ_{SE} is the secondary electron emission coefficient, $\alpha = pA_p \exp(-B_p p/E)$ is the ionization coefficient valid for all gases in local equilibrium, d is the gap distance, $x_0 = [(1 + 8\bar{E})^{1/2} - 1]/(4\bar{E})$, \bar{E} is the dimensionless electric field given by $\bar{E} = E/D_{FN}$, $D_{FN} = (0.95B_{FN}\phi^{3/2})/\beta$, $B_{FN} = 6.85 \times 10^7 \text{ V cm}^{-1}\text{eV}^{-3/2}$ is a Fowler-Nordheim constant, ϕ is the electrode work function (we consider 5.15 eV for nickel electrodes), β is the field enhancement factor (we assume 55), $j_{FN} = C_{FN}E^2 \exp(-D_{FN}/E)$ is the Fowler-Nordheim current density, $C_{FN} = [(A_{FN}\beta^2)/(\phi t^2(y))]\exp\{[(3.79 \times 10^{-4})^2 B_{FN}]/\phi^{1/2}\}$, and $A_{FN} = 6.2 \times 10^{-6} \text{ A eV V}^{-2}$ is a Fowler-Nordheim constant. Table 2.1 summarizes the values of A_p and B_p , the E/p range, and E/N range over which they are valid, where N is the gas number density. The A_p ,

B_p , and E/p values are from (Raizer, 1991), and the E/N range is calculated using (Huxley et al., 1966)

$$E/N [\text{Townsend}] = (1.0354 \times 10^{-2} T)(E/p) [\text{V cm}^{-1} \text{Torr}^{-1}], \quad (2-2)$$

where T is the gas temperature in K. While the values of A_p and B_p become inaccurate at the very high E/p values at low pressures considered, they provide a first approximation in lieu of using theories specifically for high E/p values (Davydov, 2006; Friedland, 1974; Li et al., 2013), which will be considered in future studies.

Table 2.1. Values for A_p and B_p from Raizer (1991), and the E/p and E/N ranges for which they are valid. The E/p range is from Raizer (1991) and the E/N range is calculated from (2-2) considering room temperature Huxley et al. (1966).

| Gas | A_p [$\text{cm}^{-1} \text{Torr}^{-1}$] | B_p [$\text{V cm}^{-1} \text{Torr}^{-1}$] | E/p [$\text{V cm}^{-1} \text{Torr}^{-1}$] | E/N [Td] |
|----------|---|---|---|------------|
| Argon | 12 | 180 | 100-600 | ~300-1800 |
| Nitrogen | 12 | 342 | 100-600 | ~300-1800 |
| Neon | 4 | 100 | 100-400 | ~300-1200 |
| Xenon | 26 | 350 | 200-800 | ~600-2400 |

Additionally, we can compare to A_p and B_p values from Marić et al. (2005) and Lieberman & Lichtenberg (2005). Marić et al. (2005) gives A_p and B_p in units of m^2 and Td, respectively, and notes that $1 \text{ Td} = 10^{-21} \text{ Vm}^2$ and $1 \text{ Vcm}^{-1} \text{ Torr}^{-1} = 3.0341 \text{ Td}$ at 293 K. Table 2-2 summarizes the A_p and B_p values as they are presented in Marić et al. (2005) and converted to the units used in Table 2-1 and their corresponding E/N ranges as given in Marić et al. (2005).

Table 2.2 Values for A_p and B_p from Marić et al. (2005) and the corresponding E/N range. The A_p and B_p values are given with the units used in Marić et al. (2005) and converted to the units used in Table 2-1 for comparison.

| Gas | A_p [10^{-21} m ²] | B_p [Td] | A_p [cm ⁻¹ Torr ⁻¹] | B_p [V cm ⁻¹ Torr ⁻¹] | E/N [Td] |
|----------|-------------------------------------|------------|--|--|------------|
| Argon | 34.9 | 534 | 11.5 | 176 | 300-1800 |
| Nitrogen | 35.8 | 986 | 11.8 | 325 | 300-1800 |
| Neon | 13.3 | 337 | 4.4 | 111 | 300-1200 |
| Xenon | 72.8 | 1000 | 24 | 330 | 600-2400 |

The current work uses the A_p and B_p values from columns 2 and 3 of Table 2.1. However, we can easily assess how using the values from columns 3 and 4 of Table 2.2 would change our results.

There is an average percent difference of 5.8% between the two A_p values and 5.9% between the two B_p values. Ultimately, though, we care about how these different values will affect the breakdown voltage. Thus, we *really* care about how V_* changes, since that is what normalizes our breakdown voltage. This value is simply $V_* = E_*L = E_*p_*^{-1}A_p^{-1} = (E_*B_p)/(E_*A_p) = B_p/A_p$.

Table 2.3 summarized the values of V_* calculated using A_p and B_p from Raizer (1991) and Marić et al. (2005).

Table 2.3. V_* calculated from A_p and B_p from Raizer (1991) and Marić et al. (2005).

| Gas | V_* (Raizer, 1991) | V_* (Marić et al., 2005) | % difference |
|----------|----------------------|----------------------------|--------------|
| Argon | 15 | 15.3 | 2.01% |
| Nitrogen | 28.5 | 27.5 | 3.36% |
| Neon | 25 | 25.3 | 1.35% |
| Xenon | 13.5 | 13.7 | 2.19% |

The average percent difference of ~2.2% is well within the margin of error. Thus, these variations in A_p and B_p do not appreciably change the breakdown voltage.

While this model does not consider processes such as backdiffusion, photon- and electron-induced secondaries, or reflection, other work (Phelps, 1999; Li & Go, 2014) has developed methods to

include these phenomena through additional coefficients. For example, Li and Go calculated the transmission and reflection coefficients (Li & Go, 2014) to determine the impact of ion-enhanced field emission on breakdown. Additionally, Phelps and Petrović assessed the effect of secondary electrons produced from the surface and gas phase (Phelps, 1999). Furthermore, Venkatraman and Alexeenko (2012) stated that, while backscattering could be incorporated, it is typically neglected because it only decreases current density by ~5%. One may incorporate all of these physics in the model, but we currently focus on a simpler model to assess the transition from field emission to Townsend avalanche.

Numerically solving (2-1) for a specified pressure and gap distance yields the breakdown electric field. Analogous to previous work (Loveless & Garner, 2016; Loveless & Garner, 2017a), we define dimensionless variables as

$$\bar{E} = EE_*^{-1}, \bar{\tau} = T\tau_*^{-1}, \bar{p} = pp_*^{-1}, \bar{d} = dL^{-1}, \bar{J}_{FN} = j_{FN}j_0^{-1}, \bar{\alpha} = \alpha L, \bar{\phi} = \phi\phi_*^{-1}, \quad (2-3)$$

where \bar{E} is the dimensionless electric field (~0.04), $\bar{\tau}$ is the dimensionless temperature (~0.03), \bar{p} is the dimensionless pressure (~0.01), \bar{d} is the dimensionless gap distance (~500), \bar{J}_{FN} is the dimensionless Fowler-Nordheim current (~10-13), $\bar{\alpha}$ is the dimensionless ionization coefficient (~0.01), and $\bar{\phi}$ is the dimensionless work function (~0.05) with the corresponding scaling terms given by

$$\begin{aligned}
p_* &= E_* B_p^{-1}, \quad L = p_*^{-1} A_p^{-1}, \quad j_0 = (A_{FN} E_*^2) / (t^2(\gamma) \phi_*), \\
\phi_* &= [(3.79 \times 10^{-4})^2 B_{FN}]^2, \quad E_* = 0.95 B_{FN} \phi_*^{3/2}, \\
\tau_* &= \frac{\pi m \sigma_{CE} B_p}{8ek} \left\{ \frac{A_{FN}}{\epsilon_o A_p t^2(\gamma) [(3.79 \times 10^{-4})^2 B_{FN}]^2} \right\}^2.
\end{aligned} \tag{2-4}$$

Note that the definitions differ from our previous analyses (Loveless & Garner, 2016; Loveless & Garner, 2017a) by completely pulling out all ϕ and β terms to better quantify the impact of field emission. While the physical meaning of some scaling terms is obvious (e.g., pressure is scaled with the electric field and a material constant), we derived these parameters based on the mathematical forms of the equations. Table 2.4 shows the scaling parameters for the gases considered here.

Table 2.4 Calculated scaling parameters from (2-4) for argon, nitrogen, neon, and xenon.

| Gas | p_* [Torr] | L [m] | j_0 [A/m ²] | ϕ_* [eV] | E_* [V/m] | τ_* [K] |
|----------|--------------------|------------------------|---------------------------|---------------|-----------------------|--------------|
| Argon | 3.44×10^8 | 2.42×10^{-12} | 2.24×10^{18} | 96.81 | 6.20×10^{12} | 8476 |
| Nitrogen | 1.81×10^8 | 4.60×10^{-12} | 2.24×10^{18} | 96.81 | 6.20×10^{12} | 11288 |
| Neon | 6.20×10^8 | 4.03×10^{-12} | 2.24×10^{18} | 96.81 | 6.20×10^{12} | 21409 |
| Xenon | 1.77×10^8 | 2.17×10^{-12} | 2.24×10^{18} | 96.81 | 6.20×10^{12} | 11539 |

Coupling (2-3) and (2-4) with (2-1) yields

$$\frac{\exp[\bar{\phi}^{3/2}/(\beta \bar{E})]}{\beta \bar{\phi}^{1/2} \exp(\bar{\phi}^{-1/2})} \sqrt{\frac{\bar{\tau} \bar{E}}{\bar{p} \bar{d}^2}} \frac{\{1 - \gamma_{SE} [\exp(\bar{\alpha} \bar{d}) - 1]\}}{[\exp(\bar{\alpha} \bar{d}) - 1]} = \frac{\exp(x_o)(1 + 2\bar{E}x_o)}{x_o}, \tag{2-5}$$

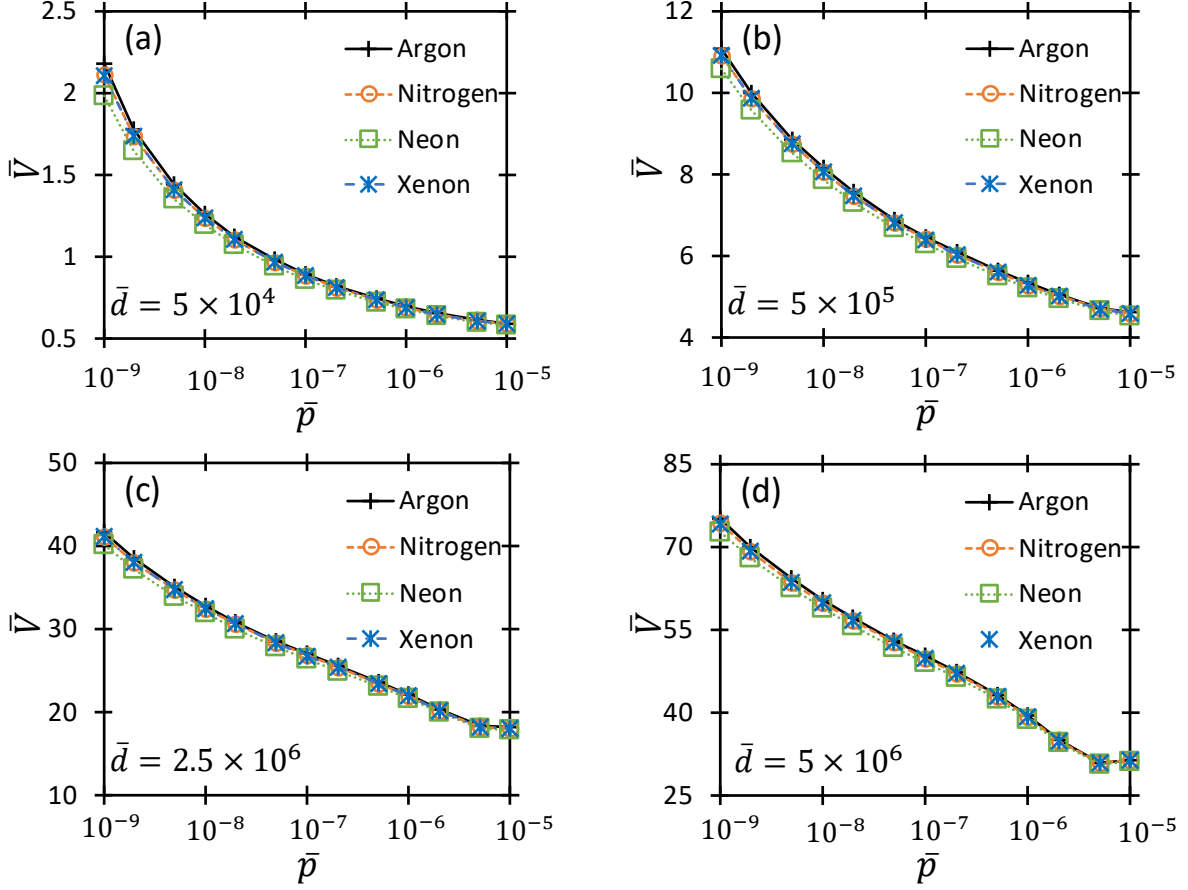


Figure 2.1. Comparison of \bar{V} as a function of \bar{p} for argon, nitrogen, neon, and xenon at dimensionless gap distances, \bar{d} , of (a) 5×10^4 , (b) 5×10^5 , (c) 2.5×10^6 , and (d) 5×10^6 . The average percent difference in \bar{V} between each of the gases is $\sim 1.6\%$, demonstrating the universality of (2-5).

which is a fully nondimensionalized breakdown condition valid for all gases and pressures. Numerically solving (2-5) for \bar{E} and applying $\bar{V} = \bar{E}\bar{d}$ yields the dimensionless breakdown voltage for a given pressure and gap distance. Figure 2.1 shows the numerical solution of \bar{V} as a function of \bar{p} for various gap distances for argon, nitrogen, neon, and xenon. We selected the gap distances (~ 100 nm to ~ 30 μm) and pressures (~ 1 Torr to ~ 5000 Torr) to avoid quantum effects at smaller gaps (Go & Venkatraman, 2014; Baille et al., 1981; Slade & Taylor, 2002) and streamer effects at larger gaps (Montijn & Ebert, 2006; Loeb & Meek, 1941) to ensure that field emission

and Townsend effects drive breakdown. The average percent difference in \bar{V} between all gases is $\sim 1.6\%$, which indicates that (2-5) is a *universal* equation for dimensionless breakdown voltage without any material dependence. This universality permits us to only consider the specific results of argon for the remainder of our analysis without loss of generality.

As previously mentioned, we consider $\beta = 55$. However, the value of β is generally unknown *a priori*, and is commonly used as a fitting parameter, which introduces some degree of uncertainty. Bilici, et al. have experimentally determined breakdown voltage as a function of gap distance for argon at atmospheric pressure, showing the spread of the breakdown voltage (Bilici et al., 2016). By nondimensionalizing this data, we can use (2-5) to numerically determine the β values that give the maximum and minimum breakdown voltage for each gap distance, and determine the associated standard deviations. Figure 2.2 shows the standard deviation of dimensionless breakdown voltage, $\sigma_{\bar{V}}$, and field enhancement factor, σ_{β} , as a function of dimensionless gap distance, \bar{d} , for gap distances ranging from 1-20 μm . Figure 2.2 demonstrates that at small gap distances, the spread of the data (and, subsequently, the discrepancy in β values) is relatively small, and increases with increasing gap distance. Interestingly, the variation of β is smallest at the gap distances corresponding to the largest contribution of field emission (Loveless & Garner, 2017a).

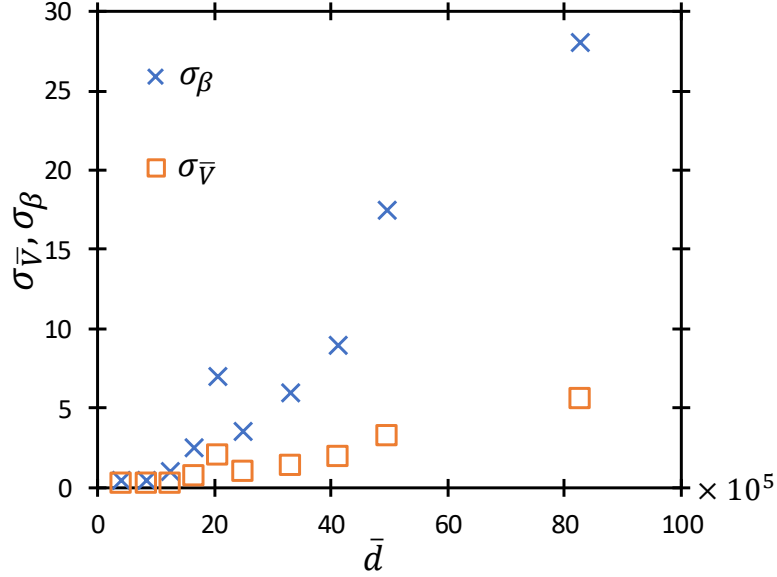


Figure 2.2. Comparison of the standard deviation of dimensionless breakdown voltage, $\sigma_{\bar{V}}$, and field enhancement factor, σ_{β} , as a function of dimensionless gap distance, \bar{d} , for gap distances ranging from 1-20 μm using the experimental results of (Bilici et al., 2016). Fitting the numerical solution of (2-5) to the experimental data from (Bilici et al., 2016) yielded the values of β for each gap distance.

2.2.2 Asymptotic equation derivation

While our previous work (Loveless & Garner, 2016; Loveless & Garner, 2017a) derived analytic equations based on $\bar{p}\bar{d} \ll 1$ or $\bar{p}\bar{d} \gg 1$, we focus here on whether $\bar{\alpha}\bar{d} \ll 1$ or $\bar{\alpha}\bar{d} \gg 1$ because varying both pressure and distance across a wide range of values will influence \bar{E} , which affects $\bar{\alpha}$. Considering $\bar{p}\bar{d} \ll 1$ or $\bar{p}\bar{d} \gg 1$ was sufficient at atmospheric pressure (Loveless & Garner, 2016; Loveless & Garner, 2017a) because the behavior of $\bar{\alpha}\bar{d}$ matched $\bar{p}\bar{d}$ (i.e. increasing gap distance increased both $\bar{\alpha}\bar{d}$ and $\bar{p}\bar{d}$) for the range of gap distances examined. However, this same trend does not hold once we vary pressure. Figure 2.1,c-d clearly show (Figure 2.1,a-b suggest, but it is more difficult to definitively state that they show) that there exists a critical pressure, \bar{p}_c , above which \bar{V} begins to increase for a given gap distance. Figure 2.3 shows both $\bar{\alpha}\bar{d}$ and \bar{p}/\bar{E} as functions of \bar{p} for various gap distances. At $\bar{p} = \bar{p}_c$, $\bar{p}/\bar{E} \approx 0(1)$. For $\bar{p} < \bar{p}_c$, $\bar{\alpha}\bar{d}$ increases with

increasing \bar{p} as in our previous microscale studies (Loveless & Garner, 2016; Loveless & Garner, 2017a), however, for $\bar{p} > \bar{p}_c$ $\bar{\alpha}\bar{d}$ *decreases* with increasing \bar{p} while $\bar{p}\bar{d}$ continues to increase. Thus, we must consider $\bar{\alpha}\bar{d}$ instead of $\bar{p}\bar{d}$ when generalizing the model for both pressure and gap distance. Since both α and d scale with L , $\bar{\alpha}\bar{d} = \alpha d$, which is simply the product of the ionization coefficient and gap distance, $\bar{\alpha}\bar{d} \ll 1$ corresponds to the region where few ionizing collisions occur (i.e. where field emission dominates) and $\bar{\alpha}\bar{d} \gg 1$ corresponds to the region where many ionizing collisions occur (i.e. where Townsend processes dominate). To the right of the minimum, the transition to *fully* Townsend-driven breakdown begins, meaning Paschen's law governs breakdown.

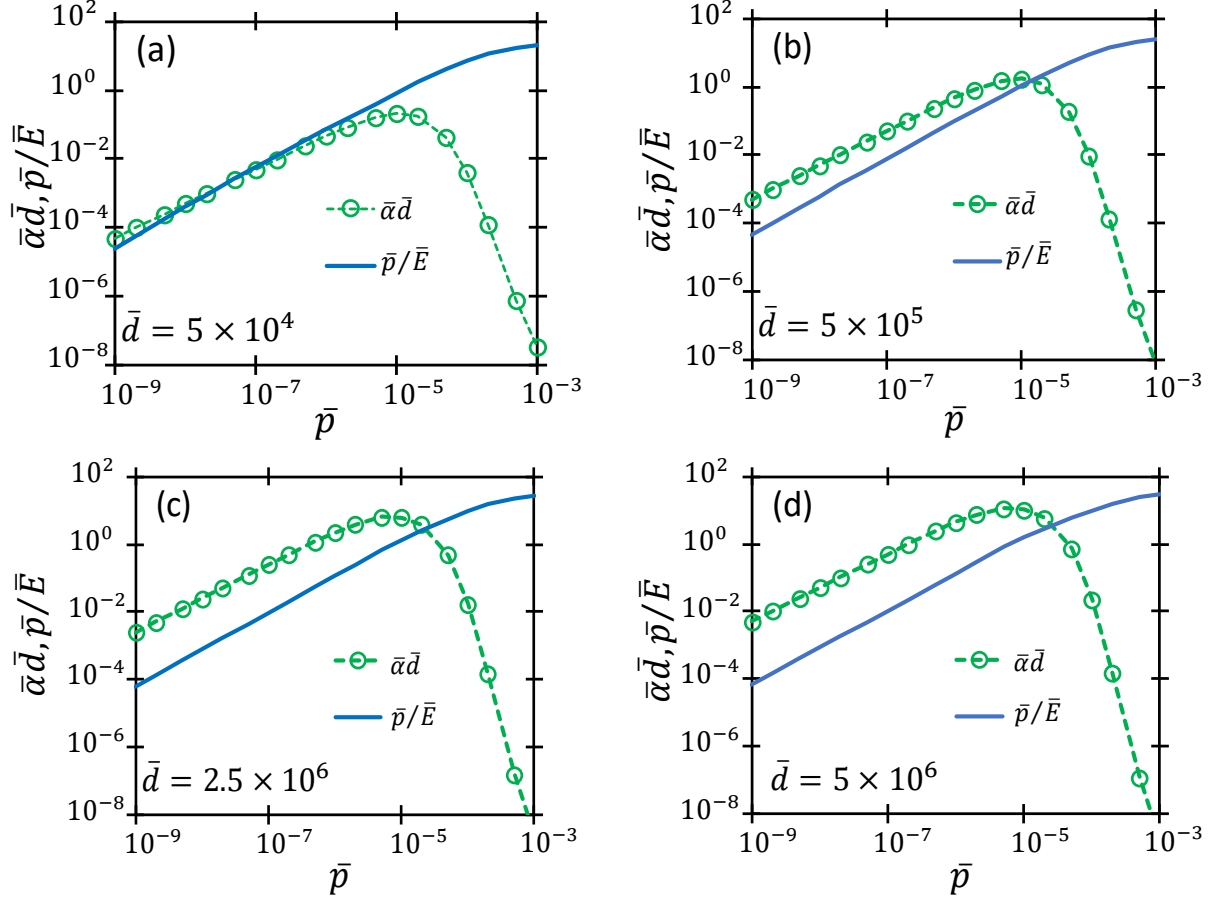


Figure 2.3. Comparison of $\bar{\alpha}\bar{d}$ as a function of \bar{p} for dimensionless gap distances, \bar{d} , of (a) 5×10^4 , (b) 5×10^5 , (c) 2.5×10^6 , and (d) 5×10^6 . As \bar{p} increases, $\bar{\alpha}\bar{d}$ increases until $\bar{p}/\bar{E} \approx 1$, at which point $\bar{\alpha}\bar{d}$ decreases.

To derive analytic solutions, we first note that $\bar{E} \ll 1$ for all gap distances and pressures considered here, which we observe from numerical solutions of (2-5) at various pressures and gap distances. Physically, since $\bar{J}_{FN} \propto \bar{E}^2 \exp(-\bar{E}^{-1})$ and $\bar{E} \ll 1$, $\bar{J}_{FN} \rightarrow 0$, as we stated above with our estimate of $\bar{J}_{FN} \approx 1 \times 10^{-13}$. Combining this simplification with simple series expansions allows us to derive analytic expressions for \bar{V} for $\bar{\alpha}\bar{d} \ll 1$ as

$$\bar{V} = \bar{d} \left[\frac{-\Delta_1 - \sqrt{\Delta_1^2 - 2\Lambda_1(\bar{\phi}^{3/2}/\beta + \gamma_{SE}\bar{p}^2\bar{d} + \bar{p})}}{\Lambda_1} \right], \quad (2-6)$$

where

$$\Delta_1 = \frac{\ln[\bar{\tau}\bar{p}^{-1}\bar{d}^{-2}]}{2} - \ln[\beta\bar{\phi}^{1/2}] - \bar{\phi}^{-1/2} - \frac{\ln[\Lambda_1]}{2} - \ln[\bar{p}\bar{d}] - \gamma_{SE}\bar{p}\bar{d} - \frac{3}{2} \quad (2-7)$$

and $\Lambda_1 = 4 \times 10^4$, and for $\bar{\alpha}\bar{d} \gg 1$ as

$$\bar{V} = \bar{d} \left[\frac{-\Delta_2 - \sqrt{\Delta_2^2 - 2\Lambda_2\bar{\phi}^{3/2}/\beta}}{\Lambda_2} \right], \quad (2-8)$$

where

$$\begin{aligned} \Delta_2 = & \frac{\ln[\bar{\tau}\bar{p}^{-1}\bar{d}^{-2}]}{2} - \ln[\beta\bar{\phi}^{1/2}] - \bar{\phi}^{-1/2} - \frac{\ln[\Lambda_2]}{2} + \ln \left\{ 1 - \gamma_{SE} \left[\exp \left(\frac{\bar{p}\bar{d}}{\exp(1)} \right) \right] \right\} \\ & - \ln \left[\exp \left(\frac{\bar{p}\bar{d}}{\exp(1)} \right) - 1 \right] - \frac{3}{2}, \end{aligned} \quad (2-9)$$

and $\Lambda_2 = 1 \times 10^5$. We chose the roots of the quadratic equations for (2-6) and (2-8) such that $\bar{V} >$

0. Appendix A provides detailed derivations of (2-6) through (2-9).

2.2.3 Transition to Paschen's law

A major difference between the analytic equations derived in (2-6)-(2-9) and those we derived previously (Loveless & Garner, 2016; Loveless & Garner, 2017a) is that we include γ_{SE} . This allows us to assess the impact of γ_{SE} on breakdown voltage and ultimately link our analyses to the classical Paschen law, which depends upon γ_{SE} (cf. (2-1)). Figure 2.4 shows the effects of increasing γ_{SE} on \bar{V} for various \bar{d} as a function of pressure from numerically solving (2-5). At small \bar{p} and \bar{d} (Figure 2.4a-b), increasing γ_{SE} has a negligible effect. However, there is a significant reduction in \bar{V} at larger \bar{p} , \bar{d} , and γ_{SE} (Figure 2.4c-d).

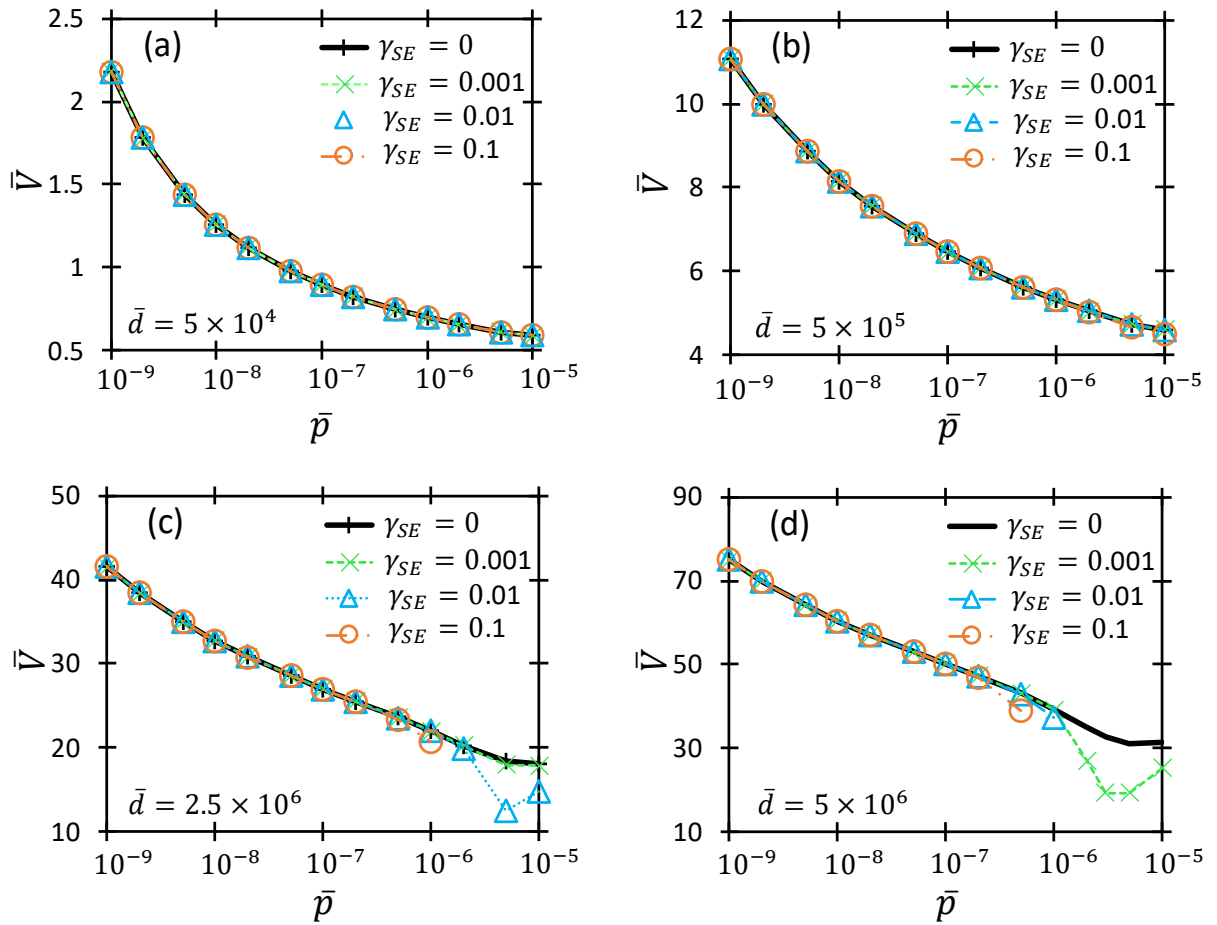


Figure 2.4. Comparison of dimensionless breakdown voltage, \bar{V} , calculated from numerically solving (2-6) as a function of dimensionless pressure, \bar{p} , for various values of γ_{SE} for dimensionless gap distances, \bar{d} , of (a) 5×10^4 , (b) 5×10^5 , (c) 2.5×10^6 , and (d) 5×10^6 .

In Figure 2.4c, numerical solutions for $\gamma_{SE} = 0.1$ do not exist for $\bar{p} \gtrsim 10^{-6}$, and Figure 2.4d shows that numerical solutions for $\gamma_{SE} = 0.1$ and for $\gamma_{SE} = 0.01$ do not exist for $\bar{p} \gtrsim 5 \times 10^{-7}$ and $\bar{p} \gtrsim 10^{-6}$, respectively. Equation (2-5) shows that sufficiently large $\bar{\alpha}\bar{d}$ and γ_{SE} will ultimately lead to $\{1 - \gamma_{SE}[\exp(\bar{\alpha}\bar{d}) - 1]\} = 0$. When this point is reached, we cannot obtain a numerical solution for \bar{V} in (2-5) because it will either be zero or negative (thus, nonphysical). Therefore, Townsend effects completely drive breakdown, and field emission effects are negligible. We can rearrange (2-5) as

$$1 - \gamma_{SE}[\exp(\bar{\alpha}\bar{d}) - 1] = \frac{\beta\bar{\phi} \exp(\bar{\phi}^{-1/2})}{\exp(\bar{\phi}^{3/2}/\beta\bar{E})} \sqrt{\frac{\bar{p}\bar{d}^2 \exp(x_0) (1 + 2\bar{E}x_0)[\exp(\bar{\alpha}\bar{d}) - 1]}{\bar{T}\bar{E} x_0}} \quad (2-10)$$

to highlight the relevant term. Once the transition to fully Townsend-driven breakdown has occurred, the right-hand side of (2-10) is ≈ 0 (or, at the very least, $\ll 1$), leading to $\{1 - \gamma_{SE}[\exp(\bar{\alpha}\bar{d}) - 1]\} \approx 0$. Substituting $\bar{\alpha} = \bar{p} \exp(-\bar{p}/\bar{E})$ and solving for \bar{V} yields

$$\bar{V} = \frac{\bar{p}\bar{d}}{\ln[\bar{p}\bar{d}] - \ln[\ln(1 + \gamma_{SE}^{-1})]}, \quad (2-11)$$

which is a dimensionless, universal form of Paschen's law. Thus, we can recover the classical Paschen law from the coupled field emission-Townsend breakdown of (2-5) under appropriate conditions and, therefore, link field emission and Paschen's law by a series of analytic expressions

across classical length scales from the electron mean free path until Meek's criterion to remain outside of the streamer discharge regime. Section 2.3 explores this transition in more detail, showing specific examples.

2.3 Analysis

2.3.1 Calculation of \bar{V}

Figure 2.5 shows \bar{V} as a function of \bar{p} at $\bar{d} = 2.5 \times 10^6$ and $\bar{d} = 5 \times 10^6$, with $\gamma_{SE} = 1 \times 10^{-3}$ or $\gamma_{SE} = 1 \times 10^{-2}$ to display the agreement between the numerical solution of (2-5), the analytic solutions of (2-6) and (2-8), and the universal Paschen law of (2-11). Figure 2.5 shows that as we increase gap distance and γ_{SE} , (2-11) agrees better with the numerical solution of (2-5). Additionally, (2-6) deviates from (2-5) as $\bar{\alpha}\bar{d}$ increases (i.e. leading up to the minimum). Conversely, (2-8) agrees better with (2-5) as $\bar{\alpha}\bar{d}$ increases. Both of these trends are expected since (2-6) assumed $\bar{\alpha}\bar{d} \ll 1$ and (2-8) assumed $\bar{\alpha}\bar{d} \gg 1$. Furthermore, the disagreement of both (2-6) and (2-8) with (2-5) as \bar{d} and γ_{SE} increase is expected, since that is the point where the system is transitioning to the classical Paschen law, leading to a better agreement of (2-11) with (2-5) in this region. Analogous to previous work (Loveless & Garner, 2017a), we can define $\mu = \ln[\beta\bar{\phi}^{1/2}] + \bar{\phi}^{-1/2}$ and $\nu = -\ln[\bar{\tau}\bar{p}^{-1}\bar{d}^{-2}]/2 + \ln[\Lambda_2]/2 - \ln\{1 - \gamma_{SE}[\exp(\bar{p}\bar{d}\exp(-1))]\} + \ln[\exp(\bar{p}\bar{d}\exp(-1)) - 1] + 3/2$ to recast (10) as $\Delta_2 = -(\mu + \nu)$ to quantify the field emission and Townsend contributions, respectively. Figure 2.6 shows μ and ν as functions of \bar{p} for various \bar{d} and γ_{SE} , and demonstrates the transition from field emission to Townsend avalanche as \bar{d} and \bar{p} increase. Furthermore, the absence of solutions for ν when $\gamma_{SE} = 0.1$ at the larger pressures and gap distances (for example, the last point in Figure 2.6b) indicates the transition to the classical Paschen law.

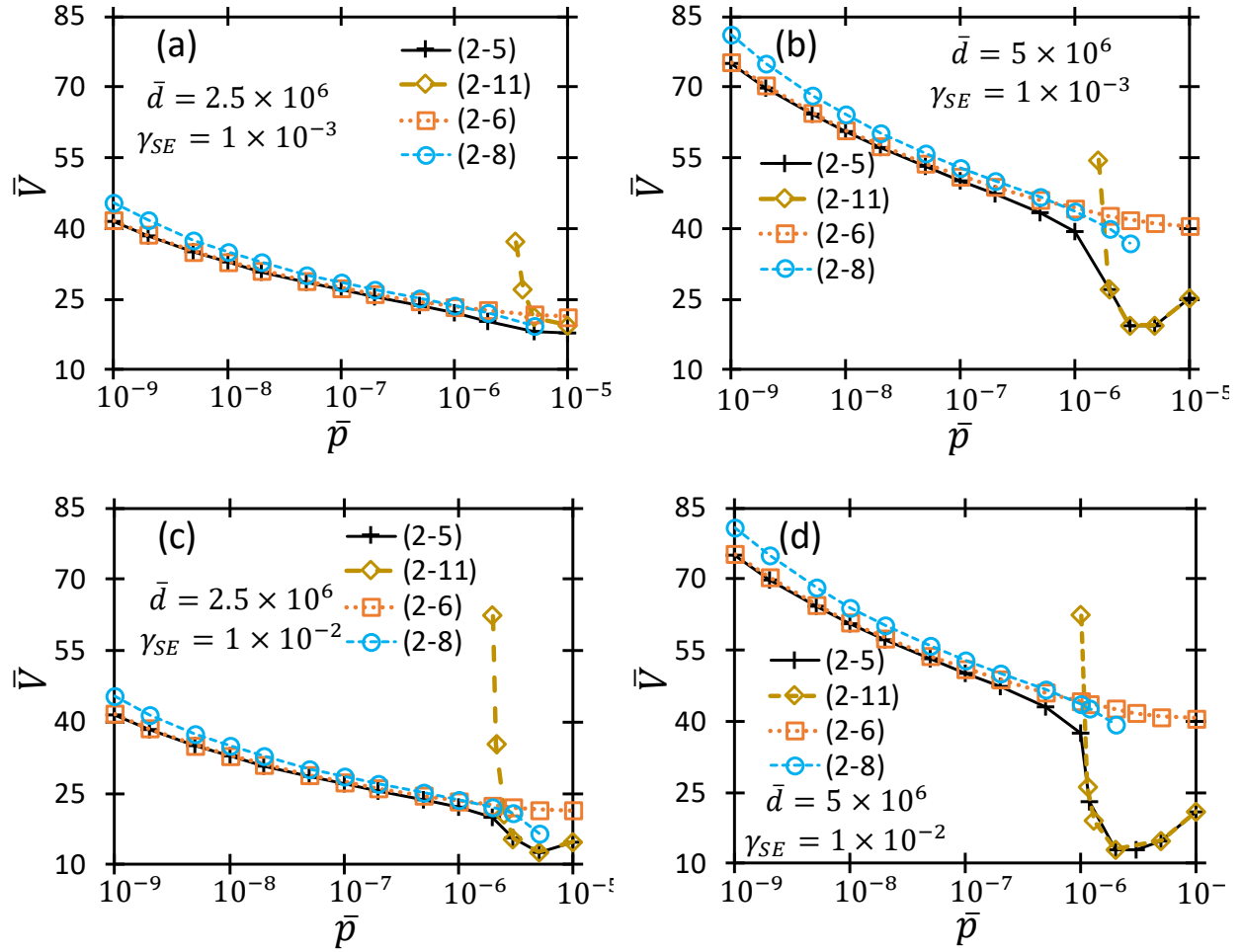


Figure 2.5. Comparison of dimensionless breakdown voltage, \bar{V} , as a function of dimensionless pressure, \bar{p} , determined from numerically solving (2-5), and calculating (2-6), (2-8), and (2-11) for (a) $\bar{d} = 2.5 \times 10^6$ and $\gamma_{SE} = 0.001$, (b) $\bar{d} = 5 \times 10^6$ and $\gamma_{SE} = 0.001$, (c) $\bar{d} = 2.5 \times 10^6$ and $\gamma_{SE} = 0.01$, and (d) $\bar{d} = 5 \times 10^6$ and $\gamma_{SE} = 0.01$.

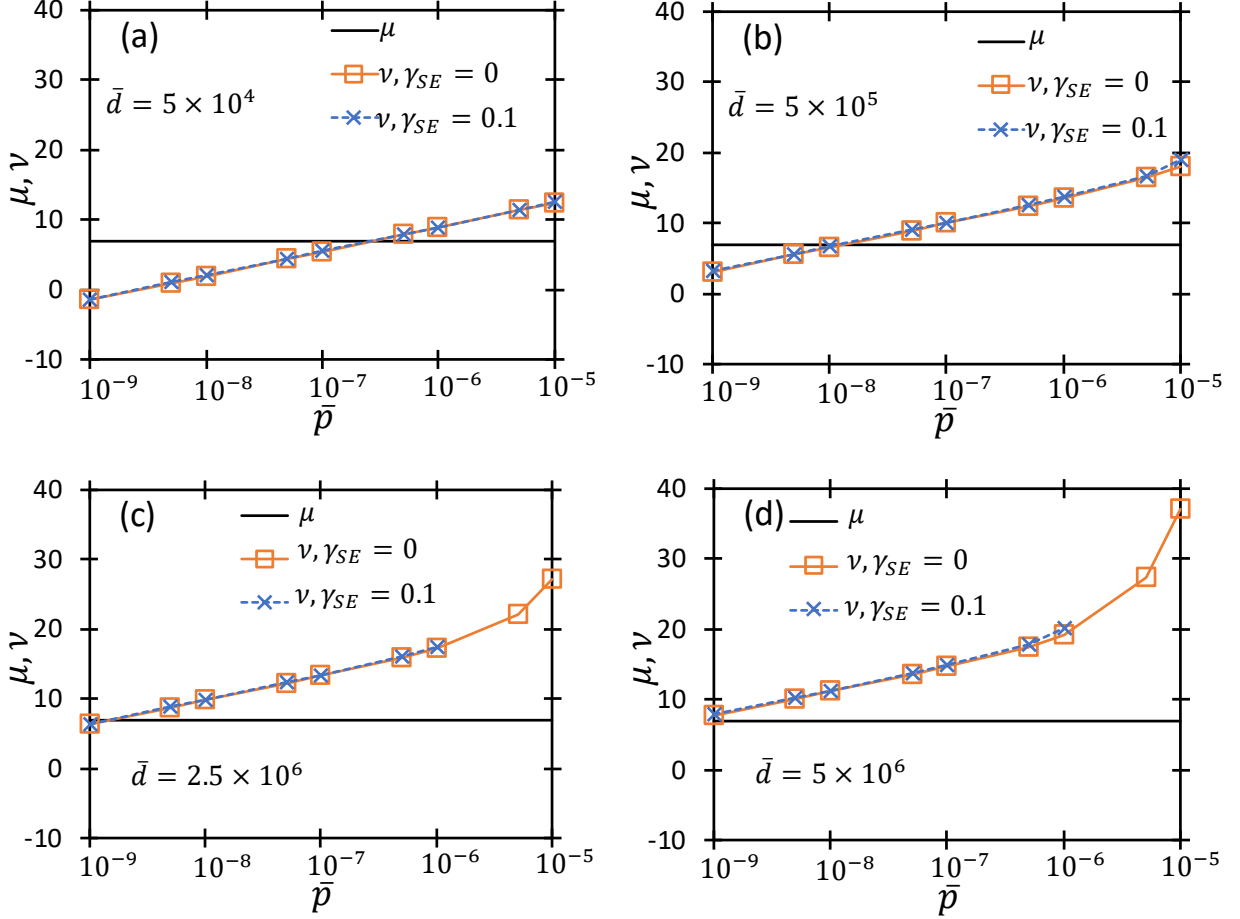


Figure 2.6. Comparison of μ and ν as a function of dimensionless pressure, \bar{p} , for $\gamma_{SE} = 0$ and $\gamma_{SE} = 0.1$ for dimensionless gap distances, \bar{d} , of (a) 5×10^4 , (b) 5×10^5 , (c) 2.5×10^6 , and (d) 5×10^6 . Figure 6c shows that transition from field emission effects dominating to Townsend effects dominating. For $\gamma_{SE} = 0.1$, we note that we can no longer solve for ν for $\bar{p} \gtrsim 10^{-6}$ in (c) and (d), due to the dominance of the Townsend avalanche and the transition to the classical Paschen law.

Figure 2.7 shows \bar{V} as a function of \bar{p} for various \bar{d} , comparing the numerical results from (2-5) with the analytic results from (2-6) and (2-8), and particle-in-cell (PIC) simulations using the one-dimensional in space and three-dimensional in velocity (1D-3v) code XPDP1 (Verboncoeur et al., 1993), which has been extended to include field emission (Venkatraman et al., 2012; Venkatraman, 2012). The average percent difference between (2-5) and XPDP1 simulations is

~10%, with better agreement generally occurring at lower pressures. Figure 2.8 shows the percent differences between (2-6) and (2-8) compared to (2-5).

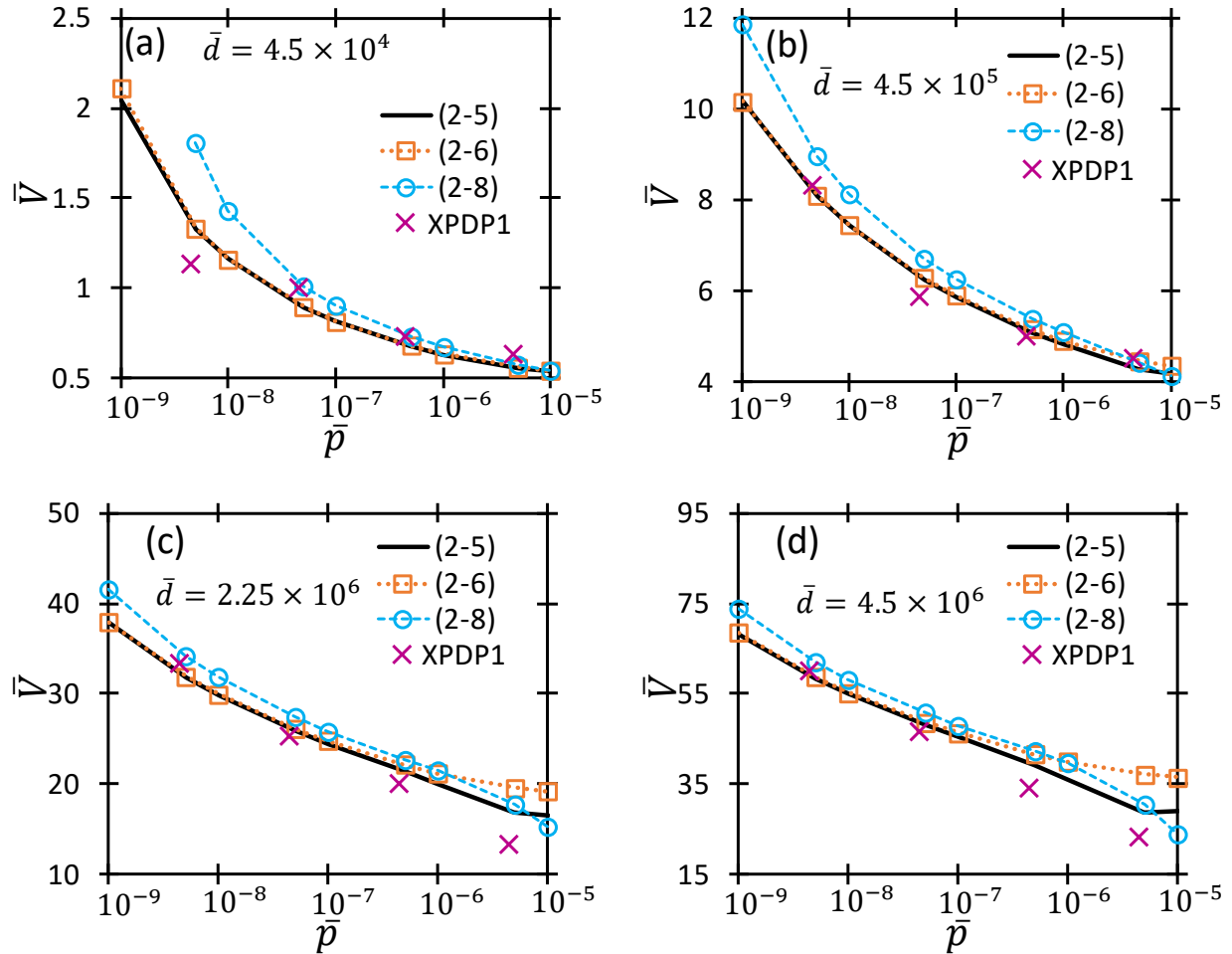


Figure 2.7. Comparison of dimensionless breakdown voltage, \bar{V} , as a function of dimensionless pressure, \bar{p} , with $\gamma_{SE} = 0$ from the numerical solution of (2-5), the analytic solution of (2-6) with $\bar{\alpha}\bar{d} \ll 1$, the analytic solution of (2-8) with $\bar{\alpha}\bar{d} \gg 1$, and XPDP1 simulations at dimensionless gap distances, \bar{d} , of (a) 4.5×10^4 , (b) 4.5×10^5 , (c) 2.25×10^6 , and (d) 4.5×10^6 . These dimensionless gap distances correspond to $\sim 0.1 \mu\text{m}$, $\sim 1 \mu\text{m}$, $\sim 5 \mu\text{m}$, and $\sim 10 \mu\text{m}$, respectively, for argon.

Figures 2.8,c-d clearly demonstrate (and Figs. 2.8,a-b suggest) that the percent difference between (2-6) and (2-5) increases with increasing pressure. In other words, \bar{V} calculated with (2-6)

increasingly deviates from \bar{V} determined from (2-5). Conversely, the accuracy of \bar{V} predicted from (2-8) increases with increasing \bar{p} . Figures 2.8c-d show that \bar{V} reaches a minimum at $\bar{p} \approx 3 \times 10^{-6}$. This occurs because (2-6) and (2-8) assumed $\bar{\alpha}\bar{d} \ll 1$ and $\bar{\alpha}\bar{d} \gg 1$, respectively, and $\bar{\alpha}\bar{d}$ increases with increasing \bar{p} until the minimum breakdown voltage is reached, at which point $\bar{\alpha}\bar{d}$ reaches a maximum and begins to decrease, as demonstrated in Figure 2.2. We more clearly demonstrate this by calculating \bar{V} with (2-5), (2-6), and (2-8) for $\bar{p} > \bar{p}_c$. Figure 2.9 shows that the agreement between (2-5) and (2-6) improves for $\bar{p} > \bar{p}_c$ while (2-5) and (2-8) increasingly disagree. Specifically, the agreement between (2-5) and (2-6) decreases as $\bar{\alpha}\bar{d}$ increases, and then increases past the minimum breakdown voltage, when $\bar{\alpha}\bar{d}$ begins to decrease again. Conversely, the agreement between (2-5) and (2-8) increases as $\bar{\alpha}\bar{d}$ increases up to the minimum breakdown voltage, and then decreases as $\bar{\alpha}\bar{d}$ begins to decrease. The secondary vertical axis shows that $\bar{\alpha}\bar{d}$ reaches its peak at $\bar{p} \approx \bar{p}_c$ and quickly decreases below one for $\bar{p} > \bar{p}_c$. It is important to note that the largest pressure considered here is nonphysical (~ 1000 atm), but we extend up to this value to demonstrate the effectiveness of the $\bar{\alpha}\bar{d}$ analytic solutions and the matched asymptotic behavior. The matched asymptotic behavior is demonstrated by the agreement of the analytic solutions with the numerical solution in their appropriate regimes (i.e. (2-6) agreeing with (2-5) when $\bar{\alpha}\bar{d} \ll 1$ and (2-8) agreeing with (2-5) when $\bar{\alpha}\bar{d} \gg 1$).

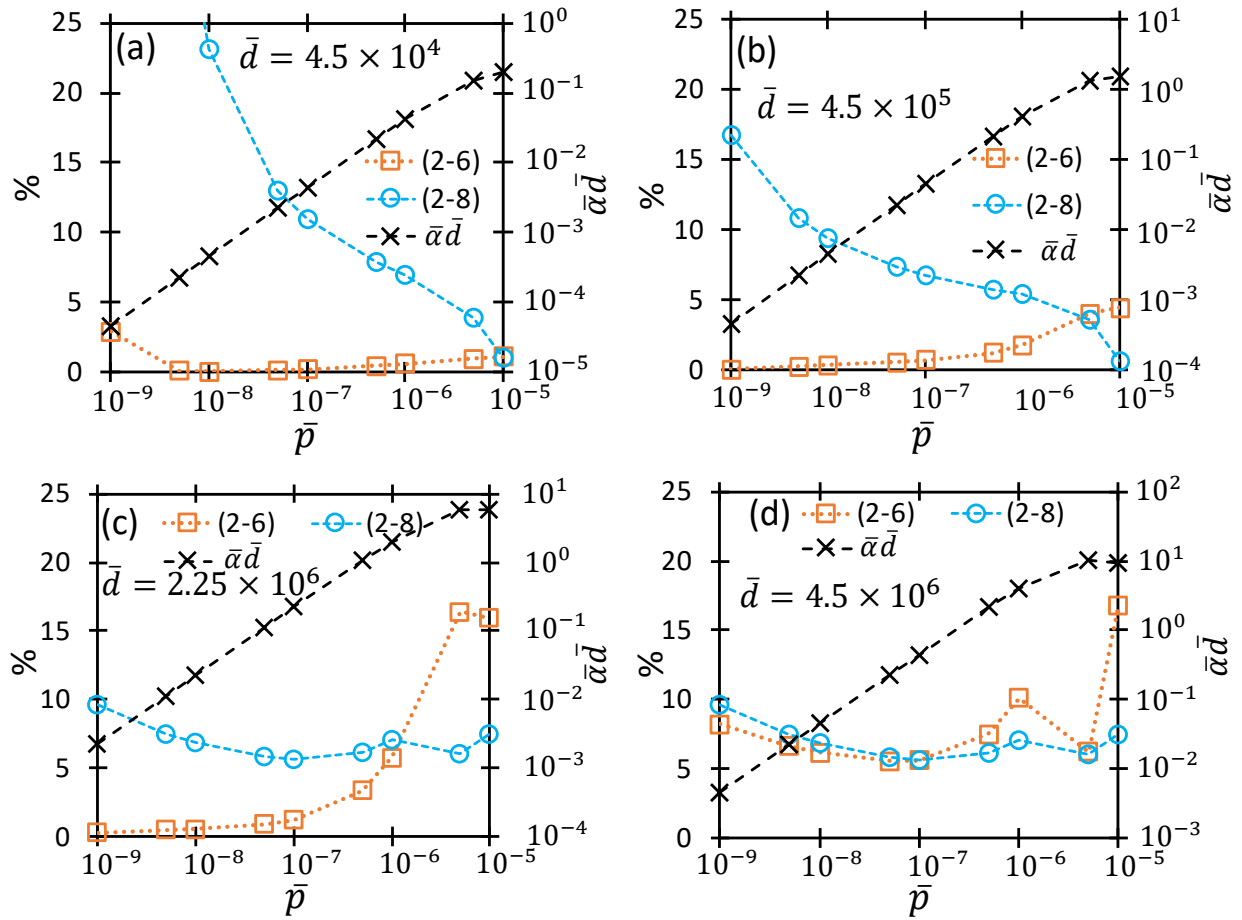


Figure 2.8. Percent difference in dimensionless breakdown voltage, \bar{V} , from (2-6) ($\bar{\alpha}\bar{d} \ll 1$) and (2-8) ($\bar{\alpha}\bar{d} \gg 1$) compared to numerical solutions from (2-5) with $\gamma_{SE} = 0$.

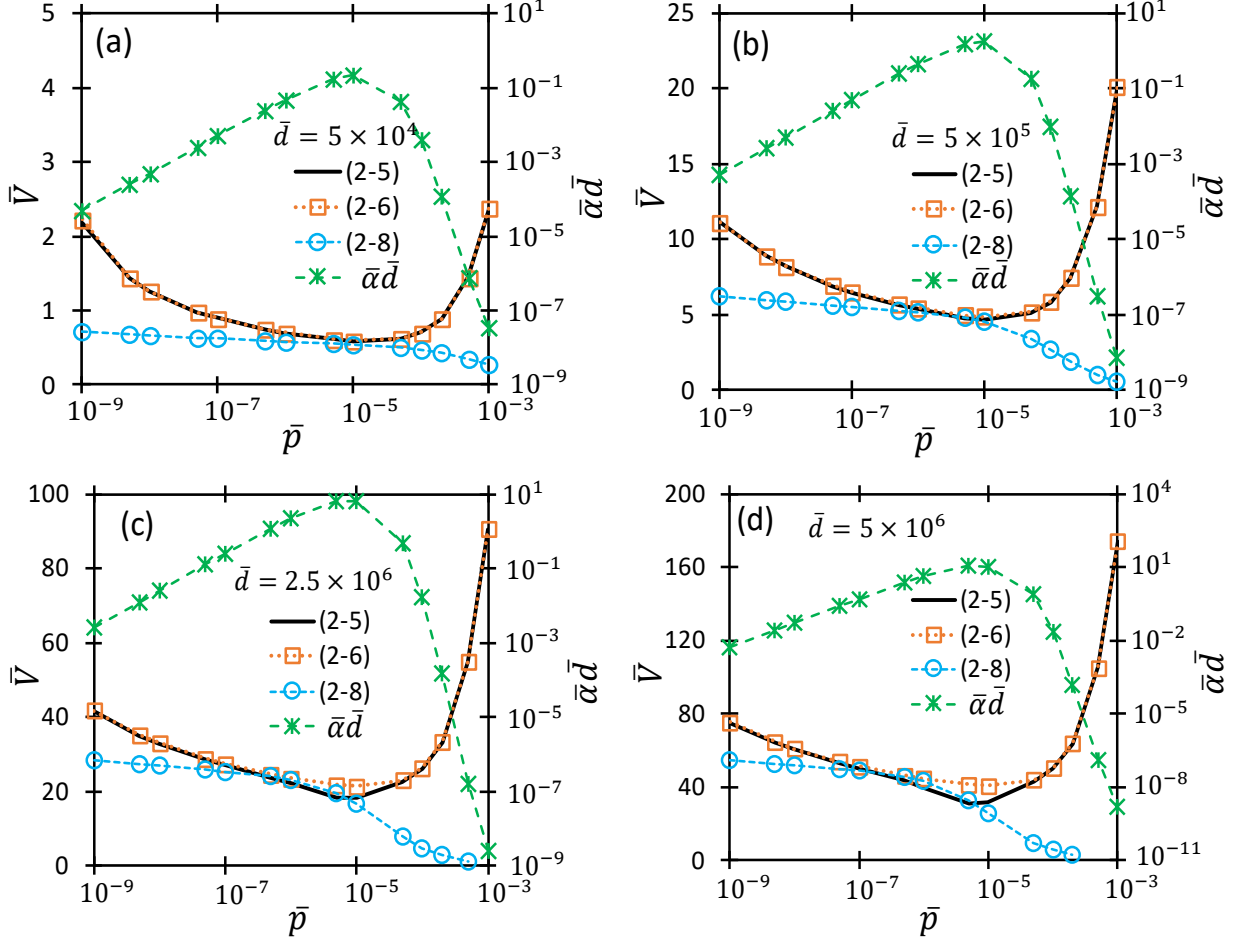


Figure 2.9. Comparison of \bar{V} from (2-5), (2-6), and (2-8) as a function of \bar{p} for \bar{d} of (a) 5×10^4 , (b) 5×10^5 , (c) 2.5×10^6 , and (d) 5×10^6 with $\gamma_{SE} = 0$. The pressure range is extended beyond that considered in Figure 2.6 to clearly show the matched asymptotic behavior of (2-6) and (2-8).

2.3.2 Minimum breakdown voltage derivation

As mentioned previously, a critical pressure, \bar{p}_c , exists corresponding to the minimum breakdown voltage for a given gap distance. Initially, we numerically solve (2-5) at different pressures for a specific \bar{d} and γ_{SE} to iteratively determine \bar{p}_c . Once we have this solution for comparison, we can solve for \bar{p}_c by setting

$$d\bar{V}/d\bar{p} = 0, \quad (2-12)$$

and using (2-6) for \bar{V} . This derivative allows us to numerically solve for the \bar{p}_c predicted by the analytic equation for \bar{V} given in (2-6). Next, using relevant series expansions as shown in detail in appendix B, we derive an analytic equation for \bar{p}_c using (2-6) for \bar{V} as

$$\bar{p}_c = \frac{-3\bar{\phi}^{3/2}X}{2\beta X^2 + 2\Lambda_1\bar{\phi}^{3/2} + 3X\beta}, \quad (2-13)$$

where $X = \ln(\bar{\tau}/\bar{d}^2)/2 - \ln[\beta\bar{\phi}^{1/2}] - \bar{\phi}^{-1/2} - \ln(\bar{d}) - \ln(\Lambda_1)/2 - 1/2 + \ln(\chi)$, and $\chi = 2 \times 10^7$, as detailed in Appendix B. It is important to note that, even though γ_{SE} was included in the equation for \bar{V} , no γ_{SE} dependence arises in (2-13) as the influence was negligible. We do not derive an analytic equation for \bar{p}_c using (2-8) (when $\bar{\alpha}\bar{d} \gg 1$) for \bar{V} because, in this regime, the transition to Paschen's law occurs. Thus, for $\bar{\alpha}\bar{d} \gg 1$, we must use (2-11) for \bar{V} . Solving (2-12) using (2-11) for \bar{V} yields an analytic equation for the critical pressure in the Paschen regime given by

$$\bar{p}_c = \frac{e}{\bar{d}} \ln\left(1 + \frac{1}{\gamma_{SE}}\right). \quad (2-14)$$

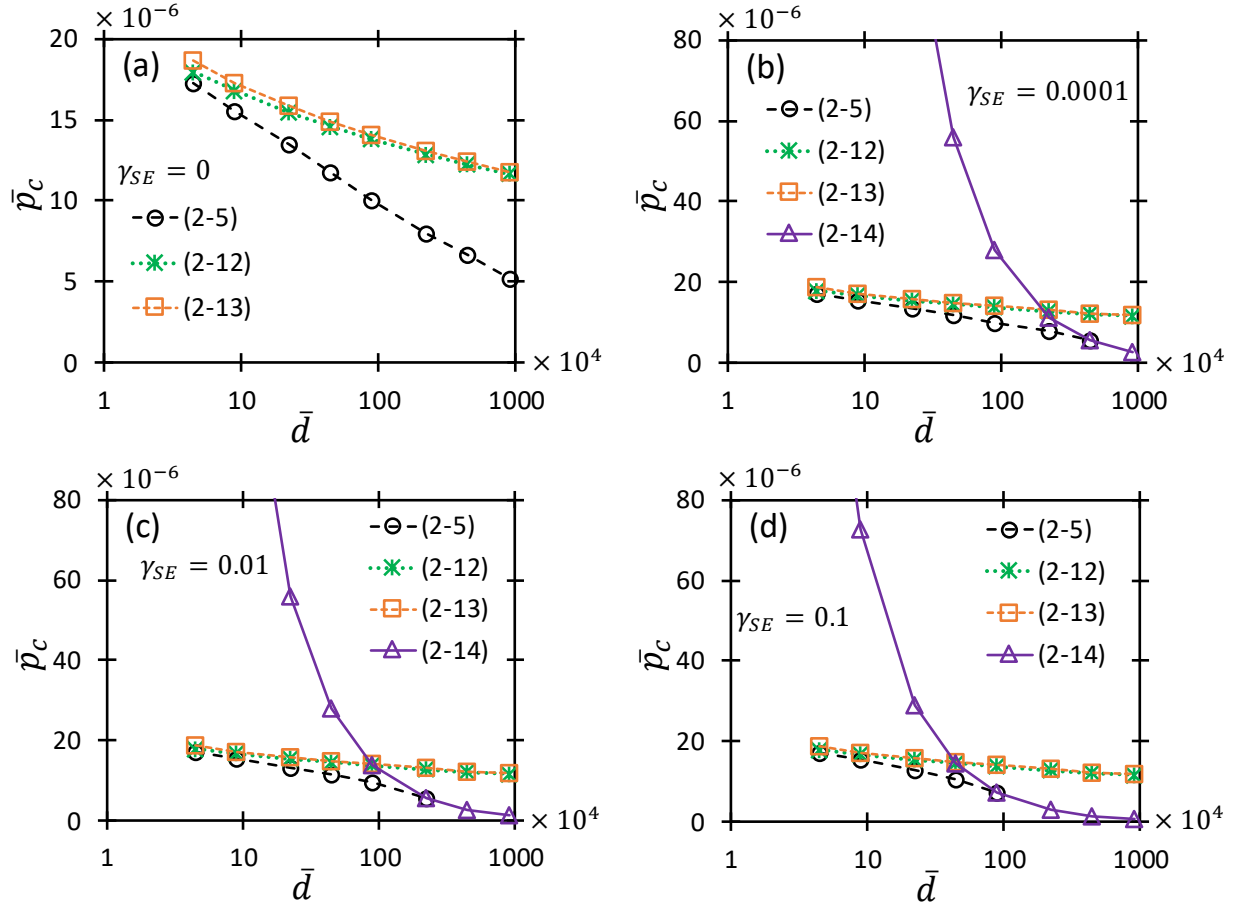


Figure 2.10. Comparison of the critical pressure at which the minimum breakdown voltage occurs, \bar{p}_c , as a function of dimensionless gap distance, \bar{d} , from the numerical solution of (2-5), the numerical solution of (2-12) using (2-6) for \bar{V} , the analytic solution for $\bar{\alpha}\bar{d} \ll 1$ given by (2-13), and the analytic solution for the Paschen regime given by (2-14).

Figure 2.10 compares \bar{p}_c as a function of \bar{d} obtained from the numerical solution of (2-5), the numerical solution of (2-12) using (2-6) for \bar{V} , and the analytic solutions of (2-13), and (2-14) as a function of \bar{d} for different γ_{SE} . Figure 2.10a shows that the numerical solution of (2-12) and the analytic solution of (2-13) agree fairly well with the numerical results of (2-5) at small \bar{d} , and then deviate as \bar{d} increases (as expected, since (2-12) and (2-13) are based on $\bar{\alpha}\bar{d} \ll 1$). Similarly, Figure 2.10,b-d show that the numerical solution of (2-12) and the analytic solution of (2-13) agree at small \bar{d} and deviate as both \bar{d} and γ_{SE} increase. While Figures 2.10,b-d show (2-14) increasing in agreement with (2-5) as \bar{d} and γ_{SE} increase, the inability to numerically solve (2-5) at the largest

\bar{d} and γ_{SE} combinations (due to the transition to the classical Paschen law previously discussed) prevents directly comparing these equations in this region. Simulations need to be performed to determine the accuracy of (2-14) in the Paschen regime where (2-5) is unable to provide results.

2.3.3 Comparison to experiment

In addition to comparing our results to simulation, we can use β as a fitting parameter and compare to experimental results. Here, we consider experimental results for argon at gap distances of 5 μm , 10 μm , 40 μm , and 500 μm using platinum electrodes ($\phi = 6.35$ eV) (Ito et al., 2001). Figure 2.11 compares the numerical solution from (2-5) with the experimental results from (Ito et al., 2001) and the solution from (2-11) assuming $\gamma_{SE} = 0.001$, which was selected to best fit the data. While the β values in Figure 2.11d are an order of magnitude higher than for Figure 2.11a-c, the trend of β increasing with increasing gap distance is consistent, although the physical reason is unclear. The region where β is roughly constant could indicate where field emission dominates with the magnitude of β decreasing as its importance declines due to the transition to Paschen's law. Interestingly, β increases with increasing gap size, although the physical reason for this is unclear. Future work will further investigate this behavior.

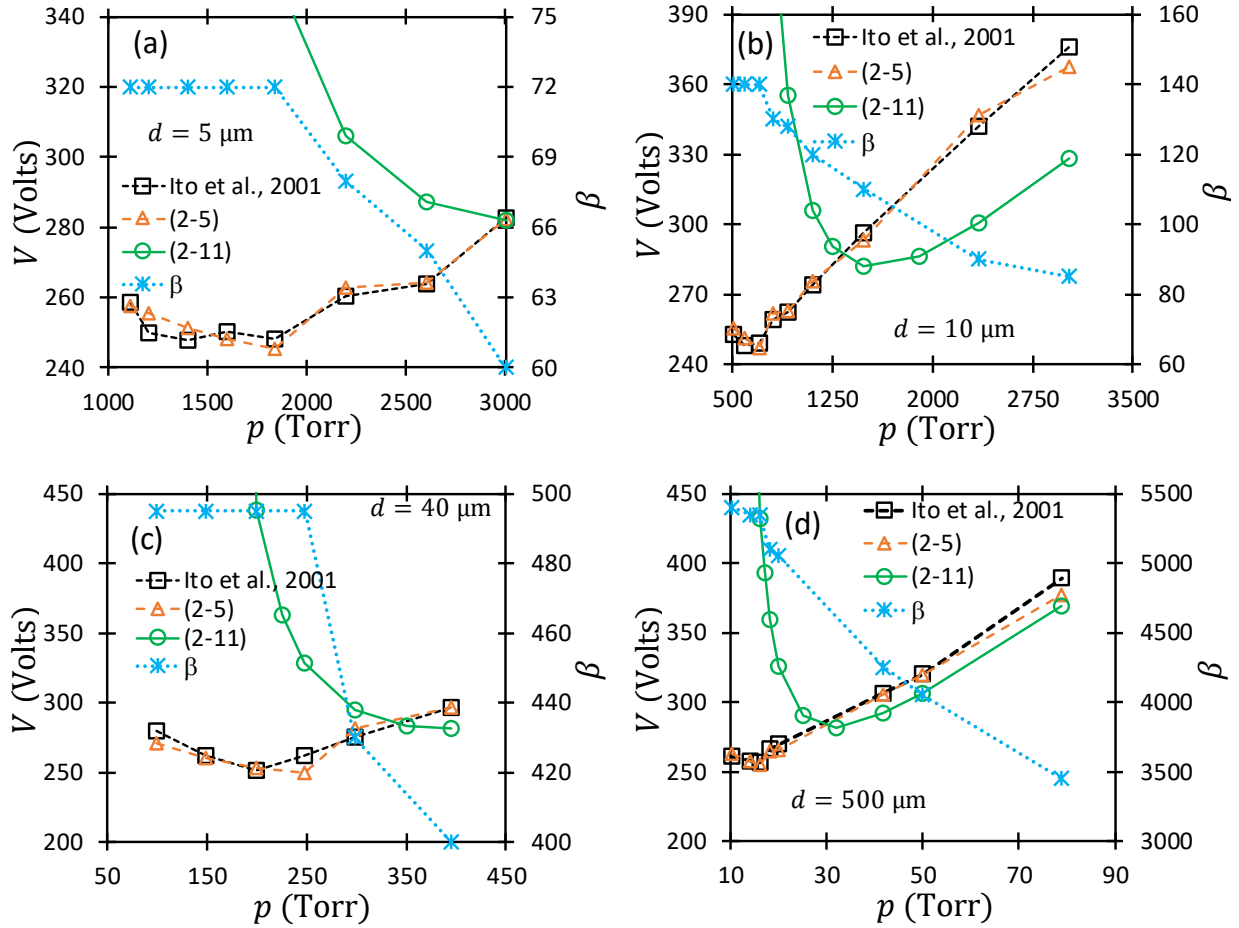


Figure 2.11 Comparison of breakdown voltage, V , as a function of pressure, p , from the experimental results of (Ito et al., 2001), the numerical solution of (2-5), and the analytic solution of (2-11) with $\gamma_{SE} = 0.001$. The field enhancement factor, β , is used as a fitting parameter, and the values selected are displayed on the secondary vertical axes.

2.4 Conclusion

This study derived universal, analytic equations for breakdown voltage coupling field emission and Townsend effects generalized for both pressure, gas, and secondary emission. These equations clearly demonstrated the transition from the field emission dominated region, across the coupled field emission-Townsend regime, to the classical Paschen law. Thus, we have derived a dimensionless, universal form of Paschen's law across classical length scales ranging from the mean free path of an electron to the transition to streamer discharge given by Meek's criterion. We

showed that (2-6) agrees with (2-5) at small $\bar{\alpha}\bar{d}$, (2-8) agrees well with (2-5) at large $\bar{\alpha}\bar{d}$, and (2-11) agrees well at large values of \bar{p} , \bar{d} , and γ_{SE} .

Due to the difficulty of calculating γ_{SE} and the computational expense involved in running particle-in-cell simulations for $\gamma_{SE} \neq 0$, we assumed $\gamma_{SE} = 0$ and showed that the numerical solution of (2-5) with $\gamma_{SE} = 0$ agrees well with particle-in-cell simulations, and (2-6) and (2-8) agree with (2-5) in their respective limits. Additionally, we presented analytic expressions for the modified Paschen minimum including field emission, showing that (2-13) agrees with numerical results at small $\bar{\alpha}\bar{d}$ where we are closer to the microscale gap sizes characteristic of the deviation from Paschen's law (Fowler & Nordheim, 1928), and (2-14) agrees with numerical results at large $\bar{p}\bar{d}$ where the pressure and gap distance places one in the classical Paschen regime. However, more analysis is required to assess the accuracy of (2-14) at sufficiently large \bar{d} and γ_{SE} when numerical results cannot be determined. Finally, we compared numerical results of (2-5) to experimental data, showing excellent agreement with a variety of gap distances and pressures when using β as a fitting parameter.

While the current study develops universal equations independent of material properties, experimentalists will ultimately substitute material properties to assess their experimental data. This leads to challenges that remain to be overcome. For instance, the field enhancement factor, β , plays a critical role in predicting experimental results for microscale gaps due to the dominance of field emission; however, accurately determining β *a priori* can be difficult as it depends upon both geometry and space-charge (Roveri et al., 2016; Miller et al., 2007; Feng et al., 2008), which will often depend upon the surface roughness of the electrodes. Experimental, theoretical, and

simulation studies assessing the impact of surface roughness on these parameters may provide bounds that guide experimentalists in predicting breakdown voltage, which becomes even more critical at smaller gap distances. Even the work function, ϕ , which is typically assumed constant in field emission calculations, has been noted to vary with surface roughness (Li & Li, 2005), which could motivate future studies in benchmarking potential variations. The secondary emission coefficient is the most critical parameter as one increases the gap distance toward the classical Paschen law regime, and it can vary with the ratio between the electric field and pressure for various gases, and can also depend upon the surface (Phelps, 1999; Nagorny & Drallos, 1997). Ultimately applying the model derived here across all gap distances and conditions will require elucidating the impacts of surface effects, which may require molecular dynamics simulations (Torfasen, 2016), to create a reasonable bound for breakdown voltage as a function of pressure, gap distance, and secondary emission characteristics. Farish et al. (1976) assessed the effect of surface roughness on breakdown voltage in mixtures of nitrogen and SF₆ gas for large gaps and found that adding nitrogen to SF₆ reduces the effects of surface roughness on breakdown (Farish et al., 1976). Additionally, Ursu et al. (1984), used electron microscopy to analyze the change in breakdown threshold after application of laser irradiation to a metallic surface and determined that defects produced by the irradiation lowered vaporization threshold, which could lower the breakdown voltage of a nearby gas. Another study assessed the impact of surface polishing on flashover properties in alumina ceramics (Asokan & Sudarshan, 1993). This study found that surface breakdown depended on the abrasiveness of the polishing material and direction of polishing sequence (coarse to fine or fine to coarse) (Asokan & Sudarshan, 1993). While these studies provide valuable information about how surface properties can impact breakdown voltage, a comprehensive study directly quantifying these relationships (e.g. how a discharge changes work

function, how different sizes and shapes of surface features effect breakdown) is still needed to eliminate the need for a fitting parameter in the present model. Furthermore, a detailed analysis quantifying the impact of uncertainties and variation in the parameters will provide insight into the bounds of the predictions for application to system design. The model presented here provides a framework for beginning such work and ultimately provides a way to develop first order predictions for system parameter design that would ultimately require confirmation with simulation and experiment.

Finally, the ultimate goal is to incorporate additional breakdown and emission mechanisms as outlined in the introduction, such as streamers, nanoscale effects, and space-charge effects. While the present study focused on specifically coupling field emission to Townsend breakdown, the overall goal is to develop a unified breakdown equation incorporating all breakdown mechanisms and clearly show the transition to each.

3. DEMONSTRATION OF FIELD EMISSION DRIVEN MICROSCALE GAS BREAKDOWN FOR PULSED VOLTAGES USING IN-SITU OPTICAL IMAGING

Reprinted from Meng, G., Gao, X., Loveless, A. M., Dong, C., Zhang, D., Wang, K., Zhu, B., Cheng, Y., and Garner, A. L. (2018) Demonstration of field emission driven microscale gas breakdown for pulsed voltages using in-situ optical imaging. *Physics of Plasmas*, 25, 082116, with the permission of AIP Publishing.

3.1 Introduction

Chapter 2 provided a detailed derivation of a dimensionless, universal gas breakdown model for microscale gaps where field emission and Townsend avalanche govern breakdown. This chapter focuses on applying the theory developed in Chapter 2 to experimental data collected and analyzed with in-situ optical imaging. Section 3.2 details the experimental setup and procedure and Section 3.3 shows the breakdown theory considered. Results and implications to device design are detailed in Section 3.4, and concluding remarks are made in Section 3.5. This chapter was published in Meng, et al. (2018).

3.2 In-Situ Electrical-Optical Measurement System

This section outlines the experimental work, which was carried out by our collaborators at Xi'an Jiaotong University. While it is straightforward to perform optical measurements with either micron spatial resolution or nanosecond temporal resolution, elucidating the dynamic physics of microscale breakdown requires simultaneously observing the breakdown channel and propagation trajectory at microscale and capturing the optical emission of charged particles in nanoseconds. It is also challenging to integrate the measurement equipment and adjust the multiple triggering signals. Simultaneously fulfilling these requirements motivated the construction of the specific measurement setup shown in Figure 3.1. The system consists of a nanosecond pulse generation

unit, a synchronous and delay triggering unit, an in-situ optical imaging unit and an electrical parameter measurement unit. The nanosecond pulse is generated by feeding DC voltage into a high voltage solid-state switch (BEHLKE HTS-50-08-UF), which delivered adjustable nanosecond pulses with a maximum amplitude up to 5 kV. A function generator (RIGOL DG3101A) provided synchronous triggering. The in-situ optical imaging unit integrates the optical microscope for micron-scale spatial resolution and the high-speed gated ICCD camera for nanosecond-scale temporal resolution. The metallographic microscope (OLYMPUS BX51M) magnifies the micron-scale test specimen with a long work distance objective lens (50×). The high-speed gated ICCD camera (ANDOR iStar 334T) detected the light emission appearance during microscale breakdown with a minimum gate width of 2 ns. An adapter flange integrated the microscope and ICCD camera to ensure the magnification and recording of the breakdown luminescence. We used a current coil (Pearson 6585) to monitor the pulse current, an attenuator probe (100:1) to monitor the pulse voltage, and a digital oscilloscope (LeCroy 104MXs-B) to record the electrical signals.

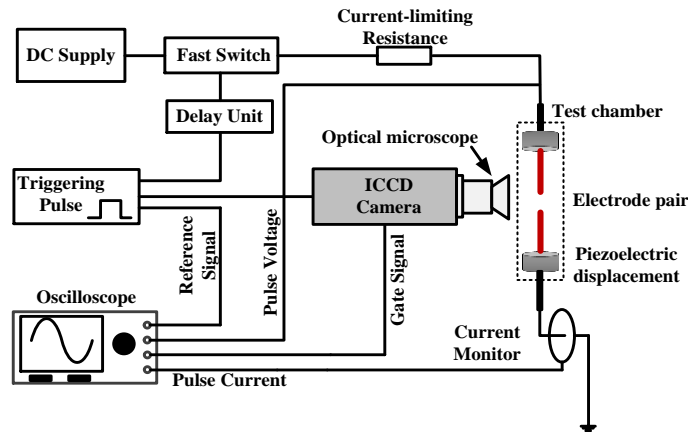


Figure 3.1. Schematic diagram of in-situ optical measurement system

Figure 3.2 shows the electrode configuration used in the experiments. The tungsten electrodes were fabricated by electrochemical etching and Joule melting, as reported elsewhere (Meng et al.,

2014). The sphere electrodes had a regular and contaminant-free surface with a radius of 20 μm . The three-dimensional piezoelectric displacement could align the electrode pair with the aid of an optical microscope, allowing precise gap adjustment from 1 μm to 25 μm . Figure 3.3 shows the waveforms for the voltages applied to the gap, the breakdown voltage, and the resulting current. As indicated in the figure, the breakdown event can be defined as the moment that the applied voltage collapses and the current dramatically rises. The applied voltage is a positive polarity nanosecond pulse, with a rise-time of approximately 20 ns and a pulse width of approximately 500 ns. The voltage waveforms demonstrate good repeatability, which ensures the reproducibility of the experimental results. Figure 3.3b compares the temporal development of a typical applied voltage below the breakdown threshold to the breakdown voltage during a typical breakdown condition.

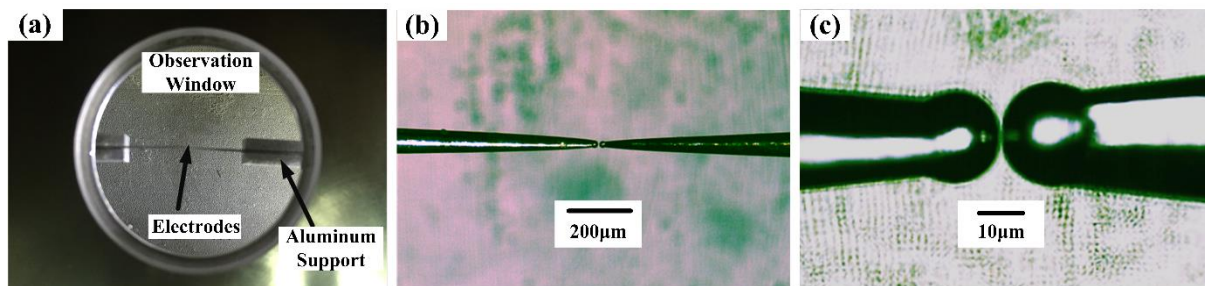


Figure 3.2. Images of the sphere-to-sphere electrode configuration used in the experiments at (a) 10 \times , (b) 50 \times , and (c) 500 \times magnification.

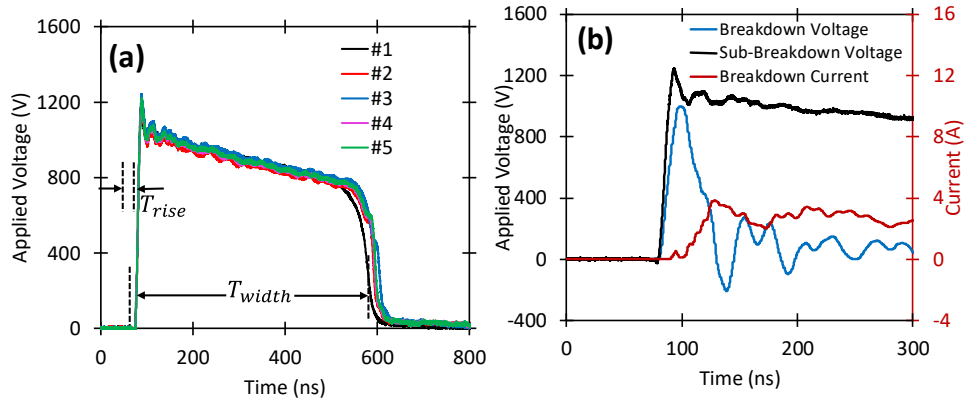


Figure 3.3. (a) A set of voltage waveforms applied to the gap below the breakdown threshold. (b) Typical breakdown voltage and breakdown current waveforms compared to a typical sub-breakdown applied voltage from (a).

The synchronous trigger is critical for accurately capturing the transient breakdown process. In principle, it is essential to measure all the potential delays in the imaging system to establish the temporal sequence of triggering, including the breakdown delay, ICCD shutter delay, and propagation delay. Figure 3.4 demonstrates the temporal sequence for the system components with the red arrows representing the propagation path of light emission due to microgap breakdown. A function signal generator produces two +5V TTL trigger signals with one for triggering the electrical breakdown across the microgap (CH1) and the other for triggering the optical imaging of the ICCD camera (CH2). In this case, the delay time of the pulse formation T_1 , gap breakdown T_2 and ICCD shutter T_3 are approximately 160 ns, 50 ns, and 70 ns, respectively. Based on the sequential relationship between the electrical and optical systems, one can program the relative delay time of the two trigger signals to synchronize electrical breakdown and the onset of the ICCD shutter. The light emission signal can be collected, magnified, and captured by the optical diagnosis system in real-time during breakdown. By activating the shutter with different delay times (T_3' , T_3'' , ..., $T_3^{(n)}$), the ICCD camera could capture a series of transient optical images

during microgap breakdown to evaluate the evolution and physical mechanism of microgap breakdown.

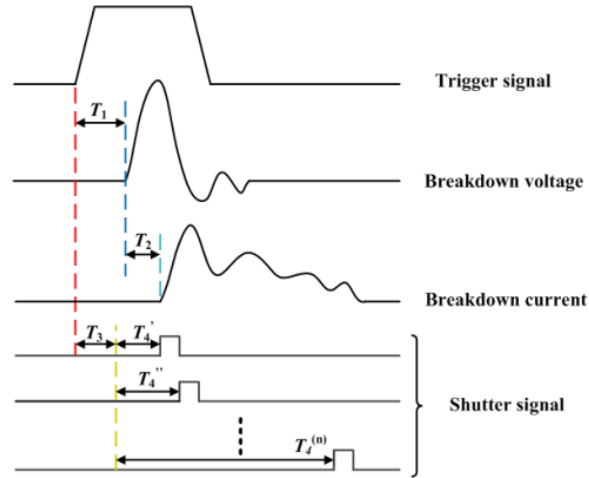


Figure 3.4. The temporal sequence of the optical and electrical processes

3.3 DC Microscale Gas Breakdown Theory

Previous studies have coupled Townsend avalanche to field emission to derive closed form solutions for gas breakdown at microscale for argon at atmospheric pressure (Loveless & Garner, 2016) any gas at atmospheric pressure (Loveless & Garner, 2017a), and any gas at any pressure (Loveless & Garner, 2017b). The general, universal (independent of gas) closed form equation across pressure and gas may be simplified for the physically relevant condition of $\alpha d \ll 1$, with $\alpha = pA_p \exp(-B_p p/E)$ the ionization coefficient and d the gap width, in the field emission dominated regime and the universal Paschen's law in the Townsend avalanche regime (Wallash & Levit, 2003). For $\alpha d \ll 1$, one obtains (Loveless & Garner, 2017b)

$$\bar{V} = \frac{\bar{d}}{\Lambda_1} \left[-\Delta_1 - \sqrt{\Delta_1^2 - 2\Lambda_1 \left(\frac{\bar{\phi}^{3/2}}{\beta} + \gamma_{SE} \bar{p}^2 \bar{d} \delta + \bar{p} \right)} \right], \quad (3-1)$$

where

$$\Delta_1 = - \left[\ln(\beta \bar{\phi}^{1/2}) + \bar{\phi}^{-1/2} + \frac{\ln(\Lambda_1)}{2} + \ln(\bar{p} \bar{d} \delta) + \gamma_{SE} \bar{p} \bar{d} + \frac{3}{2} - \frac{\ln[\bar{T}/(\bar{p} \bar{d}^2)]}{2} \right], \quad (3-2)$$

$\Lambda_1 = 4 \times 10^4$, and the bars denote dimensionless parameters given by

$$\begin{aligned} \bar{T} &= T \left[\frac{\pi m \sigma_{CE} B_p}{8ek} \left\{ \frac{A_{FN}}{\epsilon_o A_p t^2 (\gamma) [(3.79 \times 10^{-4})^2 B_{FN}]^2} \right\}^2 \right]^{-1}, \\ \bar{p} &= p B_p (0.95 B_{FN} \phi_*^{3/2})^{-1}, \\ \bar{d} &= 0.95 B_{FN} \phi_*^{3/2} \frac{A_p}{B_p} d, \bar{V} = V \frac{A_p}{B_p}, \bar{\alpha} = \alpha \left(0.95 B_{FN} \phi_*^{3/2} \frac{A_p}{B_p} \right)^{-1}, \\ \bar{\phi} &= \frac{\phi}{\phi_*} \end{aligned} \quad (3-3)$$

with $\phi_* = [(3.79 \times 10^{-4})^2 B_{FN}]^2$, $\delta = 1 - \exp \left\{ - [(\bar{d}/\bar{\lambda} - 1)/3.1]^{0.8} \right\}$, and Table 3.1 defining these variables and giving typical values. Here, we have corrected α for the mean free path by introducing δ from Ref. (Venkattraman & Alexeenko, 2012). Noting that $\Delta_1 < 0$, we define the field emission component of (3-2) as

$$\tilde{\mu} = \frac{\ln(\Lambda_1)}{2} + \ln(\beta\bar{\phi}^{1/2}) + \bar{\phi}^{-1/2} + \frac{3}{2} \quad (3-4)$$

and the avalanche component of (3-2) as

$$\tilde{\nu} = \ln(\bar{p}\bar{d}) + \gamma_{SE}\bar{p}\bar{d} - \frac{\ln[\bar{T}/(\bar{p}\bar{d}^2)]}{2}, \quad (3-5)$$

to obtain

$$\Delta_1 = -[\tilde{\mu} + \tilde{\nu}]. \quad (3-6)$$

Factoring $|\Delta_1|$ from the radical in (3-1) and then applying the binomial expansion to the resulting expression inside the radical yields

$$\bar{V} = \frac{\bar{d}}{\Delta_1} \left(\frac{\bar{\phi}^{3/2}}{\beta} + \gamma_{SE}\bar{p}^2\bar{d}\delta + \bar{p} \right). \quad (3-7)$$

For gap widths where field emission drives breakdown, the first term in the parentheses of (3-7) dominates, yielding

$$\bar{V} \approx \left(\frac{\bar{\phi}^{3/2}}{\beta\Delta_1} \right) \bar{d}, \quad (3-8)$$

where the term in the parentheses in (3-8) represents the components of field emission driving breakdown at microscale as a function of gap width. Figure 3.5a shows that $22 \lesssim |\Delta_1| \lesssim 28$ for $1 \mu\text{m} < d < 20 \mu\text{m}$, indicating that Δ_1 is approximately constant in the combined field emission and Townsend regime; therefore, (3-8) analytically indicates that the breakdown voltage varies linearly with gap width in the field emission driven regime. For any given \bar{p} and γ_{SE} , the change of $|\Delta_1|$ with respect to \bar{d} is driven by $\gamma_{SE}\bar{p}$ in (3-8) since the other two terms vary with $\ln(\bar{d})$ and $\ln(1/\bar{d})$, which grow more slowly. Changes in $\bar{\phi}$ and β do not impact the slope, or relative change, of $|\Delta_1|$. Note that changes in γ_{SE} will impact the slope, but are also very likely to change the phenomenon as small γ_{SE} will make field emission dominant and large γ_{SE} causes Townsend avalanche to dominate.

Table 3.1. Parameters and typical values for the model

| Variable | Parameter | Typical Value |
|-----------------|---|--|
| \bar{T} | Dimensionless temperature | ~ 0.03 |
| \bar{p} | Dimensionless pressure | ~ 500 |
| \bar{J}_{FN} | Dimensionless Fowler-Nordheim current | $\sim 10^{-13}$ |
| $\bar{\alpha}$ | Dimensionless ionization coefficient | ~ 0.01 |
| $\bar{\phi}$ | Dimensionless work function | ~ 0.05 |
| $\bar{\lambda}$ | Dimensionless mean free path | 1.27×10^5 |
| ϵ_0 | Permittivity of free space | 8.854×10^{-12} F/m |
| k | Boltzmann's constant | 1.38×10^{-23} J/k |
| m | Mass of gas (argon) | 6.63×10^{-26} kg |
| σ_{CE} | Charge exchange cross section | 1×10^{-18} m ² |
| γ_{SE} | Secondary electron emission coefficient | 0.001 |
| e | Electron charge | 1.6×10^{-19} C |
| A_{FN} | Fowler-Nordheim constant | 6.2×10^{-6} A eV V ⁻² |
| B_{FN} | Fowler-Nordheim constant | 6.85×10^7 V cm ⁻¹ eV ^{-3/2} |
| β | Field enhancement factor | 8-70 |
| $t^2(y)$ | Fowler-Nordheim correction factor | 1.1 |
| A_p | Material constant | $15 \text{ cm}^{-1} \text{ Torr}^{-1}$ |
| B_p | Material constant | $365 \text{ V cm}^{-1} \text{ Torr}^{-1}$ |

Previous analysis for argon at atmospheric pressure (Loveless & Garner, 2016) yielded $\bar{V} \propto \bar{d}/\ln(C\bar{d}^2)$ with C a function of pressure and temperature, which were both fixed for that study. Although this relationship indicates that $\bar{V} \propto 1/\ln(C\bar{d}^2)$ for small \bar{d} , this limit is not physically relevant since this equation must be modified as the gap width approaches the electron mean free path due to the correction in the ionization coefficient introduced in (3-1) (Venkatraman & Alexeenko, 2012). Thus, both the simple case and the more detailed analysis of the general pressure/general gas model indicate that $\bar{V} \propto \bar{d}$ when field emission dominates microscale breakdown.

As the gap width increases, Townsend avalanche becomes more important and the coupled field emission and Townsend avalanche model yields the universal Paschen's law, given by

$$\bar{V} = \frac{\bar{p}\bar{d}}{\ln(\bar{p}\bar{d}) - \ln[\ln(1 + \gamma_{SE}^{-1})]} \quad (3-9)$$

Figure 3.5(b) shows that $\tilde{\mu} > \tilde{\nu}$ for $d \lesssim 10 \mu\text{m}$ with $\tilde{\nu}$ decreasing as d decreases below $10 \mu\text{m}$, indicating a reduction in the contribution of Townsend avalanche for smaller gap sizes. For $10 \mu\text{m} \lesssim d \lesssim 20 \mu\text{m}$, $\tilde{\nu}$ approaches and exceeds $\tilde{\mu}$, indicating that the contribution of Townsend avalanche exceeds field emission. For $d \gtrsim 20 \mu\text{m}$, $\tilde{\nu} > \tilde{\mu}$, indicating that Townsend avalanche dominates and (3-9) should match experimental results. We will assess the appropriateness of (3-1), (3-8), and (3-9) for predicting experimental results in Section 3.4.

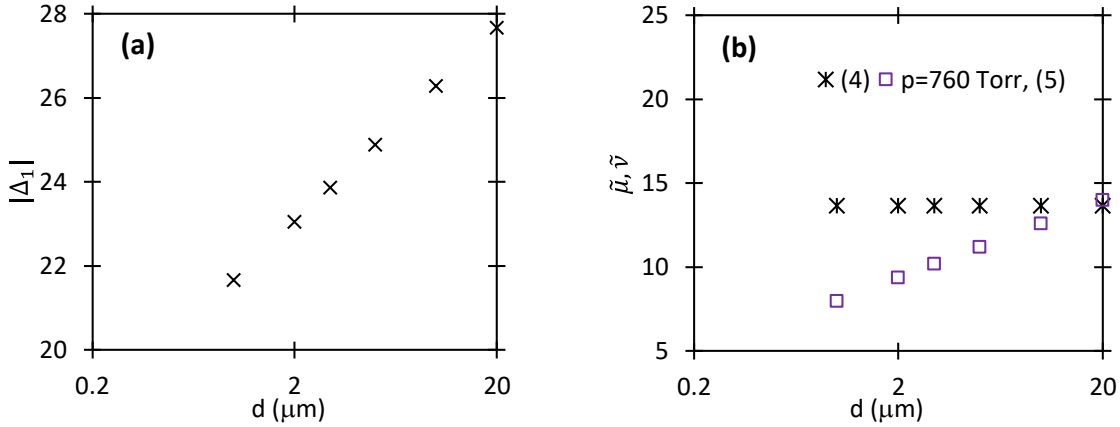


Figure 3.5. (a) Demonstration that $|\Delta_1|$ is approximately constant in the relevant gap width regime (b) Relative contributions of field emission and Townsend avalanche, given by $\tilde{\mu}$ and $\tilde{\nu}$, respectively, showing that field emission dominates until the gap width is $\sim 10 \mu\text{m}$.

3.4 Results and Discussion

3.4.1 Results

Figure 3.6(a) shows the breakdown thresholds as a function of gap width in atmospheric air (101 kPa) at room temperature (298.15 K). The electrode configuration is sphere to sphere with gap widths from $1 \mu\text{m}$ to $25 \mu\text{m}$ and Figure 3.6b compares the experimental results to the theoretical predictions from (3-1), (3-8), and (3-9) using β as a fitting parameter and $\gamma_{SE} = 5 \times 10^{-6}$ in (3-9). The low value of γ_{SE} may arise due our determining it at a small gap distance at the transition from the field emission regime. Although we may be in the Townsend regime, it is possible that the existing contribution of field emission is still sufficient that the fit value of γ_{SE} is small. Future experiments at larger gaps may better characterize this value, but this calculation suffices for now to demonstrate the transition between regimes. The variation of β by approximately an order of magnitude for these gap distances is reasonable given similar experiments reporting an order of magnitude change in β from 1 to $5 \mu\text{m}$ (Bilici et al., 2016).

The breakdown mechanisms change at 5 μm and 10 μm . For gap widths less than 5 μm , the breakdown voltage decreases with decreasing gap width and may be fit with $U = ad^k$, where U is the breakdown voltage, d is the gap width, and a and k are fitting parameters. This fitting expression agrees well with field emission driven breakdown (Lyon & Hubler, 2012; Staprans, 1966), as demonstrated by its agreement with (3-8) with $k = 1$, $a = \bar{\phi}/(\beta\Delta_1)$, and Δ_1 approximately constant for relevant gap widths, as shown in Figure 3.5a. For gap widths between 5 μm and 10 μm , $U \approx 490$ V, demonstrating a “plateau” stage. Although numerous microscale breakdown studies have noted this plateau (Go & Venkatraman, 2014), a strong hypothesis has not yet been developed. For gap widths larger than 10 μm , breakdown voltage increases dramatically with increasing gap width, indicating the increasing importance of Townsend avalanche. This agrees well with the theory, which indicates that the relative contributions of Townsend avalanche and field emission become equal between 10 μm and 20 μm , as shown in Figure 3.5b. Figure 3.6b shows that Paschen’s law agrees well with breakdown voltage for gap widths above 20 μm , which corresponds to the gap width at which point Townsend avalanche exceeds field emission in Figure 3.5b. Thus, the coupled model for DC microscale breakdown coupling field emission and Townsend avalanche agrees well with microscale breakdown behavior under nanosecond pulsed voltage, indicating a strong similarity in the fundamental phenomena driving each mechanism.

Note that the breakdown voltage varies from 386 V for a gap width is 1 μm to 842 V for a gap width of 25 μm . As the gap width shrinks to several microns, the number of gas molecules inside the gap is insufficient for the impact ionization, necessitating a higher field strength for electron avalanche. For gap widths below 5 μm , the breakdown electric field is $\sim 10^8$ V/m, which

corresponds to the threshold of field electron emission from the electrode surface. The obvious transition in the curves indicates that cathode field emission plays a dominant role in generating free electrons.

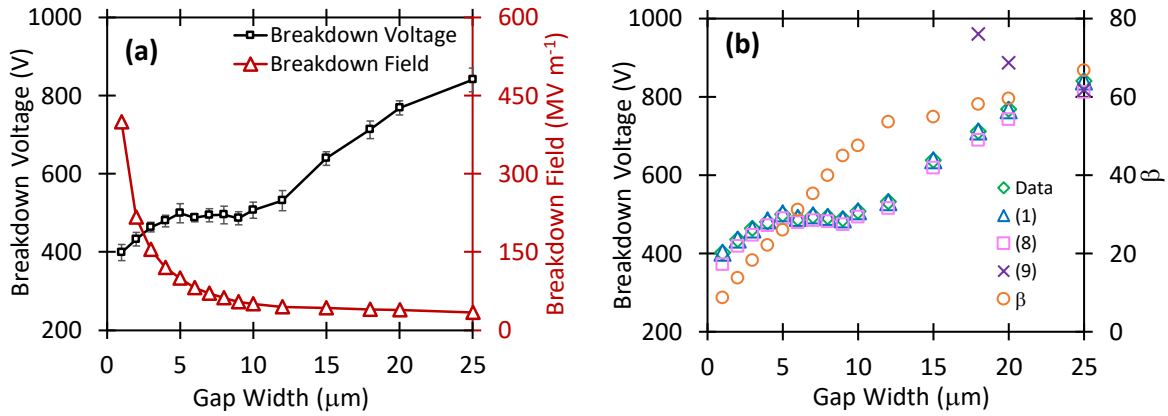


Figure 3.6. (a) Measured breakdown voltage and electric field as a function of gap width, the error bars represent the standard deviation of the measured breakdown voltage. (b) Comparison of measured breakdown voltage, matched asymptotic prediction of breakdown voltage using (3-1), simplified equation for breakdown voltage using (3-8), and universal Paschen's law using (3-9) with the fitted field enhancement factor, β , used in (3-1) and (3-8) as a function of gap width.

We next apply the in-situ electrical-optical diagnosis system to investigate the dynamic process of electric breakdown across various microgaps. Figure 3.7 shows the breakdown morphology and discharge paths for various gap widths ranging from 1 μm to 20 μm. We employed the sphere-electrodes in atmospheric air with the triggering time of the ICCD shutter set to 10 μs prior to breakdown initiation and an exposure time of 200 ms to guarantee the capture and recording of the entire breakdown process within one shot. Figure 3.7(a)-(c) show that the luminescence fills the entire gap and surroundings for gap widths of 20 μm, 15 μm and 12 μm, respectively. Theoretically, the discharge plasma should propagate along the shortest width between the electrodes with the point with the maximum electric field strength at the apex of the sphere

electrodes; therefore, the straight line connecting the apexes would be considered as the shortest breakdown path, as demonstrated by the captured images. Interestingly, Figure 3.7,d-f show that the intense light channel does not follow a straight line between the electrodes for gap widths of 9 μm , 7 μm and 5 μm , respectively. Instead, breakdown initiates from the cathode apex and propagates along a curved line to the neighbor region of the anode apex, which is a significant deviation from the theoretical prediction. Furthermore, the curvature of the breakdown increases with reducing gap size. Figure. 3.7,g-i show that the entire gap is full of luminescence with no significant breakdown channel arising for gap widths of 3 μm , 2 μm , and 1 μm . While a channel may arise for the 2 μm and 3 μm gaps, it is much fainter compared to overall luminous intensity of the remainder of the diffuse discharge, unlike the noticeably higher intensity channels that connect both electrodes at larger gaps. Based on the breakdown channel images in Figure 3.7, the effective length of breakdown paths in various gaps were measured through the measurement function of the segment line length with the image-processing program ImageJ, which are summarized in Figure 3.8. It is particularly noteworthy that the curved paths in Figure 3.7,d-f are almost the same (about 11.7 μm), independent of the gap width, which is consistent with the plateau in breakdown voltage observed from 5 μm to 10 μm in Figure 3.6a.

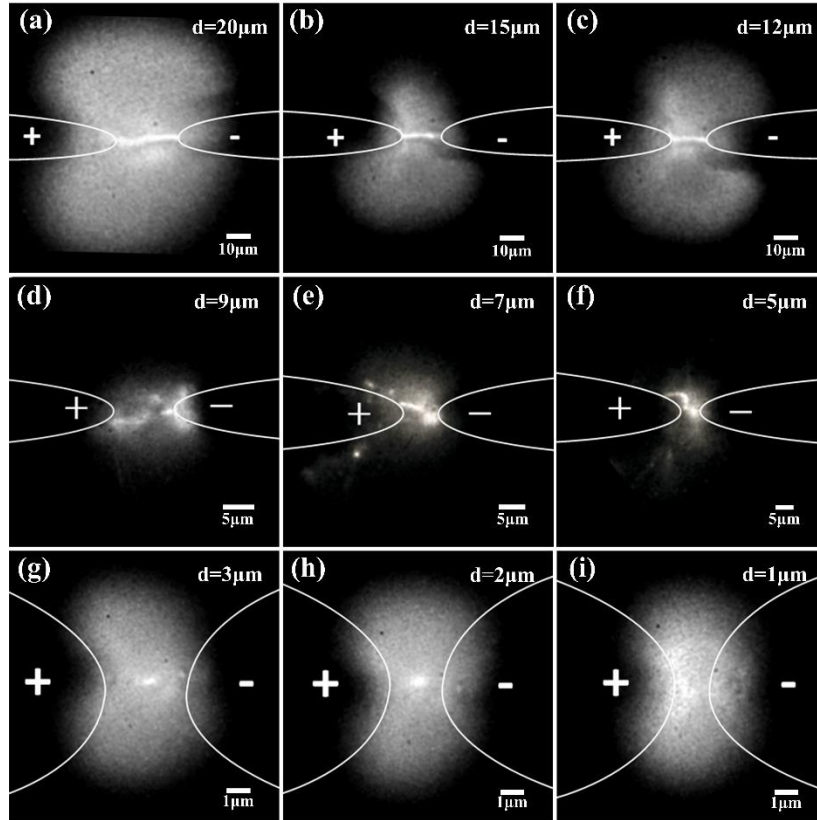


Figure 3.7. Breakdown morphology at gap widths from 1 μm -20 μm . (a)-(c) show the breakdown propagating along the shortest path with luminescence filling the surrounding area, (d)-(f) show the roughly constant path lengths regardless of gap width which is consistent with the plateau of breakdown voltage in this region, and (g)-(i) indicate no obvious breakdown channel arising at these smallest gap distances.

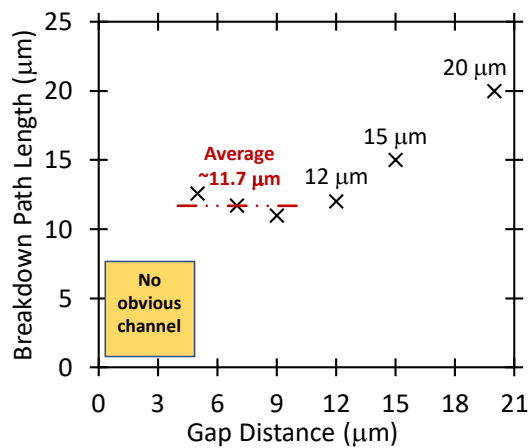


Figure 3.8. The effective lengths of breakdown path for various gap widths

In fact, the behavior for gap widths between 5 μm and 10 μm is critical for understanding the transition in breakdown mechanism both experimentally and theoretically. The correspondence between the plateau in breakdown voltage and the constant breakdown path length for gap widths in this regime implies that the extension of breakdown path provides more collision ionization and electron avalanches for the breakdown. This indicates that Townsend avalanche alone is insufficient to drive breakdown, so ion-enhanced field emission must also contribute, resulting in the “plateau” stage for breakdown voltage. Therefore, the breakdown mechanisms transition from Townsend avalanche to ion-enhanced field emission as one reduces the gap width in this regime such that field emission dominates for gaps shorter than 5 μm in this study. This also agrees with the theoretical results comparing the contribution of Townsend avalanche and field emission to gas breakdown shown in Figure 3.5b, which shows that field emission begins to dominate over Townsend avalanche for gaps greater than approximately 10 μm and Townsend avalanche becomes continuously less important for smaller gaps.

Based on the captured physical breakdown morphology across various microgaps and analytical derivation of the breakdown thresholds, we can summarize the physical mechanisms for microscale gas breakdown for the sphere-sphere electrode configuration for the three different regions as follows:

- (i) For gap widths larger than 10 μm , Townsend avalanche dominates the breakdown process and Paschen’s law predicts breakdown for sufficiently large (~ 20 μm) gaps. The breakdown demonstrates a clear electron avalanche plasma trajectory connecting the cathode tip and the anode tip by a straight path, as shown in Figure 3.9a.

(ii) For gap widths from 10 μm to 5 μm , Townsend avalanche still plays a role in breakdown but the contribution of ion enhanced field emission becomes more important. Although the gap length is not long enough for the collision ionization, the initial electron avalanche is generated in the vicinity of cathode and propagates along a curved path following the electric field lines. This could extend the effective propagation width and then may increase the collision ionization probability and frequency. The successive electron avalanches would be produced and may ultimately contribute to inducing breakdown, as shown in Figure 3.9b. Therefore, the breakdown voltage remains at the level for 10 μm for gap widths from 5-10 μm . Theoretically, we show that the breakdown voltage in this regime depends almost equally on ion enhanced field emission and Townsend avalanche at $\sim 10 \mu\text{m}$ with the dependence on field emission becoming stronger as the gap width shrinks to 5 μm .

(iii) For gap widths from 5 μm to 1 μm , the initial electron avalanche is generated in the vicinity of the cathode tip by the electrons quantum tunneling from the cathode and then colliding with the gas molecules inside the gap due to the high electric field. The higher electric field reduces the potential barrier of the cathode enough for electrons to tunnel through and be released into the gap. The gap length is comparable to the electron mean free path; therefore, the emitted electrons drift to the anode under the electric field and collide with the anode directly, heating the anode materials and the cathode due to the Nottingham effect, as shown in Figure 3.9c. Then, thermal electron emission would turn on and more electrons would be generated by the combination of field emission and thermal emission. The outgas and atoms would fill the gap, increasing the pressure. This causes a steep decline in breakdown voltage due to field emission for gaps less than 5 μm . Theoretically, the increased importance of the field emission contribution to breakdown shown in Figure 3.5b and the agreement of (3-8), which depends

solely on field emission since one may consider Δ_1 as a constant, with experimental data indicate the dominance of field emission as the breakdown mechanism for this range of gap widths.

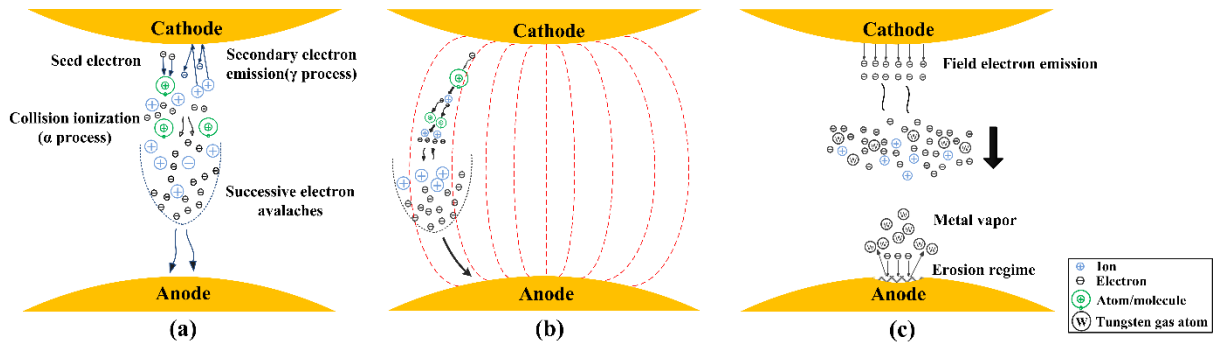


Figure 3.9. The physical process unifying Townsend avalanche and field emission for microscale breakdown for (a) $d > 10 \mu\text{m}$, (b) $d = 5 \mu\text{m} - 10 \mu\text{m}$, (c) $d = 1 \mu\text{m} - 5 \mu\text{m}$.

3.4.2 Implications to engineering of microplasma devices

Understanding the fundamental mechanism of gas breakdown at microscale will have far reaching impact on practical devices due to the numerous applications that leverage microplasmas (Becker, 2017), including excimer lamps with emissions in the VUV (Kogelschatz, 2012), ozone generators (Kim, Park, & Eden, 2007), arrays for flat panel light sources (Eun & Gianchandani, 2012), nanoparticle synthesis (Lin & Wang, 2015), medicine (Iza et al., 2008), environmental remediation (Becker, 2010), detectors (Zhu et al., 2008; Joffrion et al., 2017), microthrusters (Baranov, 2018), and combustion (Elkholy et al., 2018). Even within each of these categories, the application space can be quite broad. For instance, medical applications of microplasmas may range from eradicating microorganisms (Park et al., 2018) to treating scars (Wang et al., 2017). Given this breadth of application, microplasma system parameters may have different voltage modalities (e.g. DC, AC,

RF, or microwave), gases (e.g. air, noble gases), and use various electrode materials. All these parameters will impact the discharge mechanisms and breakdown mechanisms. Elucidating these mechanisms to enable the successful prediction breakdown conditions a priori, particularly given the impact of surface roughness on breakdown voltage at microscale due to the impact of field enhancement, is thus crucial for system optimization and for engineering devices for subsequent commercial development (Hourdakis, Simonds, & Zimmerman, 2006; Dariwal, Torres, & Desmulliez, 2000; Torres & Dhariwal, 1999; Zhang et al., 2017). It becomes particularly important for long-term system operation where discharges may alter the electrode surfaces, thus exacerbating the challenges with predicting breakdown voltages unless the fundamental understanding of the breakdown mechanisms yields reasonable bands for threshold conditions. The present study provides the first step in linking this fundamental physics to practical engineering parameter design by demonstrating the contribution of field emission and Townsend avalanche to breakdown in air at microscale. This clear demonstration of the impact of field emission using experiments and theory shows the importance of quantifying the field enhancement and the potential applicability of and existing universal (true for any) gas breakdown theory for guiding system design.

3.5 Conclusion

In summary, we have shown experimentally and analytically the transition from Townsend avalanche to field emission driven breakdown for microscale gaps using pulsed voltages. The applicability of a DC gas breakdown theory to the pulsed breakdown experiment indicates the similarity in the mechanism involved. Future analysis and simulations assessing electron and ion

motion under these conditions will indicate the potential sensitivity of this mechanism to pulse duration and repetitive pulses, which are often used in combustion, biology, and medicine.

4. THE TRANSITION TO PASCHEN'S LAW FOR MICROSCALE GAS BREAKDOWN AT SUBATMOSPHERIC PRESSURE

Reprinted from Loveless, A. M., Meng, G., Ying, Q., Wu, F., Wang, K., Cheng, Y., and Garner, A. L. (2019) The transition to Paschen's law for microscale gas breakdown at subatmospheric pressure, *Scientific Reports*, 9, 5669.

4.1 Introduction

While Chapter 2 details the derivation of a dimensionless, universal breakdown model generalized for gas, gap distance, and pressure, validation of this model against experimental data is needed. This chapter takes the breakdown model detailed in Chapter 2 and uses it to analyze experimental data collected at various pressures. Specifically, this chapter considers the transition from field emission to Paschen's law at sub-atmospheric pressures (Loveless et al., 2019). Section 4.2.1 details the experimental setup and results and 4.2.2 demonstrates the numerical and analytic equations used to assess the data. Section 4.2.3 looks deeper into understanding the effects of field enhancement factor, secondary emission coefficient, and work function on the transition to Paschen's law. Concluding remarks are made in Section 4.3. This work was published in Loveless, et al. (2019).

4.2 Theoretical and Experimental Analysis

4.2.1 Experimental setup and results

The experimental work analyzed theoretically was obtained by our collaborators at Xi'an Jiaotong University. A detailed description and block diagram of the experimental setup can be found in Section 3.2 of this dissertation. Briefly, the experimental system consists of a nanosecond pulse generation unit, a synchronous and delay triggering unit, an in-situ optical imaging unit, and an electrical parameter measurement unit. We generated the nanosecond pulse by feeding DC voltage

into a high voltage solid-state switch (BEHLKE HTS-50-08-UF), which delivered adjustable nanosecond pulses with a maximum amplitude up to 5 kV. Synchronous triggering was performed by a function generator (RIGOL DG3101A). We integrated an in-situ optical imaging unit with an optical microscope to achieve micron-scale spatial resolution and a high-speed gated ICCD camera to attain nanosecond-scale temporal resolution. A metallographic microscope (OLYMPUS BX51M) with a long work distance objective lens (50 \times) magnified the micron-scale test specimen. We used a high-speed gated ICCD camera (ANDOR iStar 334T) to detect light emission during gas breakdown with a minimum gate width of 2 ns. A current coil (Pearson 6585) monitored pulse current, an attenuator probe (100:1) measured pulsed voltage, and a digital oscilloscope (LeCroy 104MXs-B) reported the signal. This letter focuses on breakdown measurements; further experimental assessments will be reported elsewhere.

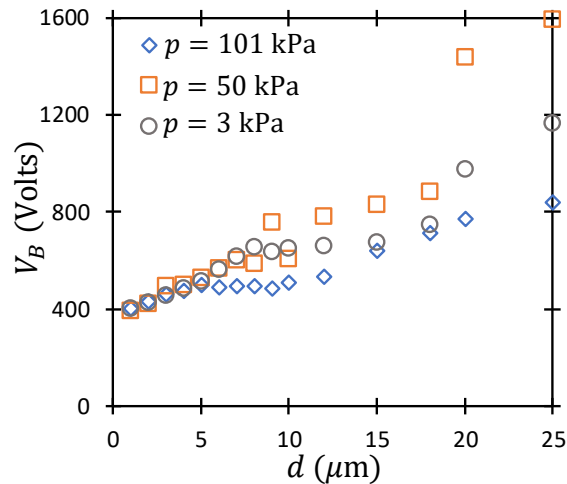


Figure 4.1. Measured breakdown voltage (V_B) as a function of gap distance (d) for pressures (p) of 3 kPa, 50 kPa, and 101 kPa.

Figure 4.1 shows the experimental results for breakdown voltage in air at pressures of 3, 50, and 101 kPa for gap distances from 1-25 μm . When plotted as a function of d , V_B is relatively

insensitive to p at smaller gap distances where one anticipates field emission driven breakdown. Measured V_B diverges with p for $d \gtrsim 5 \mu\text{m}$. While our previous theoretical studies have examined V_B as a function of either p or d (Loveless & Garner, 2016; Loveless & Garner, 2017b; Loveless & Garner, 2017b), the relatively large difference in p here suggests that collisionality, or pd , may elucidate the experimental behavior. Thus, we will assess $V_B(pd)$ when we apply the matched asymptotic theory to the experimental data.

4.2.2 Dimensionless model derivation and comparison to experiment

We start from the general, nondimensional, universal (true for any gas) breakdown equation, given by (Loveless & Garner, 2017b)

$$\frac{\exp[\bar{\phi}^{3/2}/(\beta\bar{E})]}{\beta\bar{\phi}^{1/2}\exp(\bar{\phi}^{-1/2})}\sqrt{\frac{\bar{T}\bar{E}}{\bar{p}\bar{d}^2}}\frac{\{1-\gamma_{SE}[\exp(\bar{\alpha}\bar{d})-1]\}}{\exp(\bar{\alpha}\bar{d})-1}=\exp(1)(1+2\bar{E}), \quad (4-1)$$

where $\bar{\phi} = \phi/\phi_*$ is the dimensionless work function of the electrode material with $\phi_* = [(3.79 \times 10^{-4})^2 B_{FN}]^2$ in eV, β is the field enhancement factor, $\bar{E} = E/E_*$ is the dimensionless breakdown electric field with $E_* = 0.95 B_{FN} \phi_*^{3/2}$ in V/m, $\bar{p} = p/p_*$ is the dimensionless pressure with $p_* = E_* B_p^{-1}$ in Torr, $\bar{d} = d/L$ is the dimensionless gap distance with $L = p_*^{-1} A_p^{-1}$ in m, $\bar{T} = T/T_*$ is the dimensionless temperature with $T_* = [(\pi m \sigma_{CE} B_p)/(8ek)]\{A_{FN}/[\epsilon_0 A_p t^2(\gamma)\phi_*]\}^2$ in K, γ_{SE} is the secondary emission coefficient, $\bar{\alpha} = \alpha L$ is the dimensionless ionization coefficient with $\alpha = A_p p \exp(-B_p p/E)$ in m^{-1} , and all terms without bars correspond to the dimensional (measured) quantities of those with bars. Additionally, A_{FN} and B_{FN} are Fowler-Nordheim constants, A_p and B_p are gas constants, m is the mass of the gas atom in kg, σ_{CE} is the charge

exchange cross section, e is the electron charge, k is Boltzmann's constant, ϵ_0 is the permittivity of free space, and $t^2(y) \approx 1.1$ (Spindt et al., 1976) is a Fowler-Nordheim correction factor used since the Schottky reduction factor, y , is sufficiently less than one for the data considered here.

Table 4.1 summarizes typical values.

Table 4.1. Summary of parameters considered in this work

| Parameter | Name | Value | Unit |
|---------------|--------------------------------|------------------------|------|
| V_B | Breakdown voltage | Variable | V |
| V_* | Breakdown voltage scale | 24.3 | V |
| d | Gap distance | Variable | m |
| L | Gap distance scale | 3.92×10^{-12} | m |
| E | Breakdown electric field | Variable | V/m |
| E_* | Breakdown electric field scale | 6.20×10^{12} | V/m |
| p | Pressure | Variable | kPa |
| p_* | Pressure scale | 1.70×10^8 | Torr |
| T | Temperature | 300 | K |
| T_* | Temperature scale | 7976 | K |
| ϕ | Work function | 4.7 | eV |
| ϕ_* | Work function scale | 96.81 | eV |
| β | Field enhancement factor | Variable | N/A |
| γ_{SE} | Secondary emission coefficient | 10^{-5} | N/A |

We numerically solve equation (4-1) and choose β to fit to the nondimensionalized experimental data from Figure 4.1 as a function of $\bar{p}\bar{d}$, with $\gamma_{SE} = 10^{-5}$ and $\bar{V} = \bar{E}\bar{d}$. Figure 4.2a shows the fitting of equation (4-1) and the universal PL (UPL) (Loveless & Garner, 2017b), given by

$$\bar{V}_B = \frac{\bar{p}\bar{d}}{\ln(\bar{p}\bar{d}) - \ln[\ln(1 + \gamma_{SE}^{-1})]}, \quad (4-2)$$

to the measured data with β shown in Figure 4.3. We note that the experimental data for 50 kPa and 101 kPa actually intersects with the UPL, indicating the transition from the combined FE/TA regime to the traditional PL. Moreover, the 50 kPa data intersects the UPL to the left of the Paschen minimum, while the 101 kPa data intersects the UPL near the minimum, as observed in previous applications of this theory to atmospheric pressure data (Loveless & Garner, 2017b, Meng et al., 2018). This stands to reason since previous results (Meng et al., 2019) indicate the transition should occur around 18 μm . Since the curves in Figure 4.2a are universal, they hold for any combination of parameters that yield these intersections, so the intersection with the UPL could occur on either side of the minimum at atmospheric pressure depending upon gas and electrode conditions.

We can analytically assess this intersection since $\bar{\alpha}\bar{d} \gg 1$ generally for the data considered here, allowing us to simplify \bar{V} to obtain (Loveless & Garner, 2017b)

$$\bar{V} = \frac{\bar{d}}{\Lambda_2} \left[-\Delta_2 - \sqrt{\Delta_2^2 - 2\Lambda_2(\bar{\phi}^{3/2}/\beta)} \right], \quad (4-3)$$

where

$$\Delta_2 = \frac{\ln[\bar{T}\bar{p}^{-1}\bar{d}^{-2}]}{2} - \ln[\beta\bar{\phi}^{1/2}] - \bar{\phi}^{-1/2} - \frac{\ln[\Lambda_2]}{2} - \ln\left[\exp\left(\frac{\bar{p}\bar{d}}{\exp(1)}\right) - 1\right] \quad (4-4)$$

$$+ \ln\left\{1 - \gamma_{SE}\left[\exp\left(\frac{\bar{p}\bar{d}}{\exp(1)}\right)\right]\right\} - \frac{3}{2},$$

and $\Lambda_2 = 1 \times 10^5$. Analogous to Ref. (Meng et al., 2018), we can further simplify (4-3) to obtain a limiting equation for \bar{V} , given by

$$\bar{V} = \frac{\bar{\phi}^{3/2}}{\beta|\Delta_2|} \bar{d}. \quad (4-5)$$

Figure 4.2b compares the limiting results from equation (4-5) to the numerical calculations from equation (4-1) using β from Figure 4.3. The limiting results agree well with equation (4-1) at low $\bar{p}\bar{d}$ and deviate as $\bar{p}\bar{d}$ increases. The numerical results of equation (4-1) and analytic results of equation (4-3) have an average percent difference of 3.97% while the results of equation (4-1) and the limiting results of equation (4-5) differ by an average of 3.71%. Thus, we use equation (4-5) in Figure 4.2b and the remainder of the analytic assessment without sacrificing accuracy. Also important concerning global universality, Figure 4.2 emphasizes that the breakdown voltage scales differently in the different regimes. Upon satisfying the PL condition (transitioned from the FE/TA combined regime to the conventional PL regime), the behavior the breakdown voltage scales with pd and one recovers the UPL. At smaller gaps, Figure 4.2a shows that breakdown voltage scales with \bar{d} . Thus, while breakdown exhibits universal behavior, this universal behavior varies depending upon the dominant breakdown mechanism.

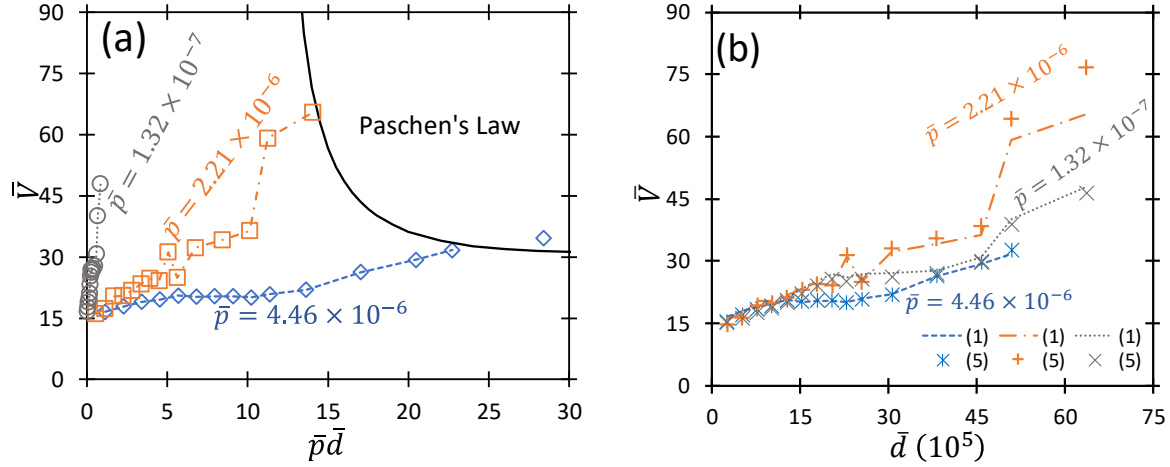


Figure 4.2. (a) Dimensionless breakdown voltage, \bar{V} , as a function of the product of dimensionless pressure and gap distance, $\bar{p}\bar{d}$, for various pressures compared to results from the universal Paschen's law (UPL) determined from (4-2) with $\gamma_{SE} = 10^{-5}$ using β from Figure 4.3. The symbols represent experimental data points and the dashed lines represent the numerical solution of (4-1), using field enhancement factor β as a fitting parameter. (b) Dimensionless breakdown voltage, \bar{V} , as a function of dimensionless gap distance, \bar{d} . Numerical results from (4-1) are shown as the dashed lines and the limiting results of equation (4-5) are shown as symbols with $\gamma_{SE} = 10^{-5}$ using β from Figure 4.3. There is an average percent difference between equations (4-1) and (4-5) of 3.71%.

Figure 4.3 shows β for fitting equation (4-1) to the data in Figure 4.2 as functions of the product of dimensionless pressure and gap distance, $\bar{p}\bar{d}$, and the dimensionless electric field, \bar{E} . For 50 kPa and 101 kPa, β increases linearly with increasing $\bar{p}\bar{d}$, as observed previously in the FE dominant regime at atmospheric pressure (Loveless & Garner, 2017b; Meng et al., 2018). Eventually, β approaches a constant, which corresponds to the transition from the FE to TA regimes, as also observed previously (Loveless & Garner, 2017b; Meng et al., 2018). Interestingly, this occurs at a lower $\bar{p}\bar{d}$ for 50 kPa. Previous results indicate that this transition is not solely driven by $\bar{p}\bar{d}$, but by \bar{p} and \bar{d} independently, which is supported by this work. For 3 kPa, β also increases linearly at low $\bar{p}\bar{d}$, but much more rapidly. While the current experiments cannot achieve sufficient voltage to measure V_B at larger d for 3 kPa, the theory suggests that the intersection with the UPL will occur at a much higher β than either of the other pressures studied. Figure 4.3b indicates that β is a

function of \bar{E} , which is also supported by previous work (Venkatraman, 2015; Buendia & Venkatraman, 2015). Interestingly, β at the two highest pressures studied here is identical when plotted as a function of \bar{E} , suggesting potential universality in this regime. Future work at lower pressures and larger gap distances can better characterize these transitions and further characterize the dependence of β on \bar{E} .

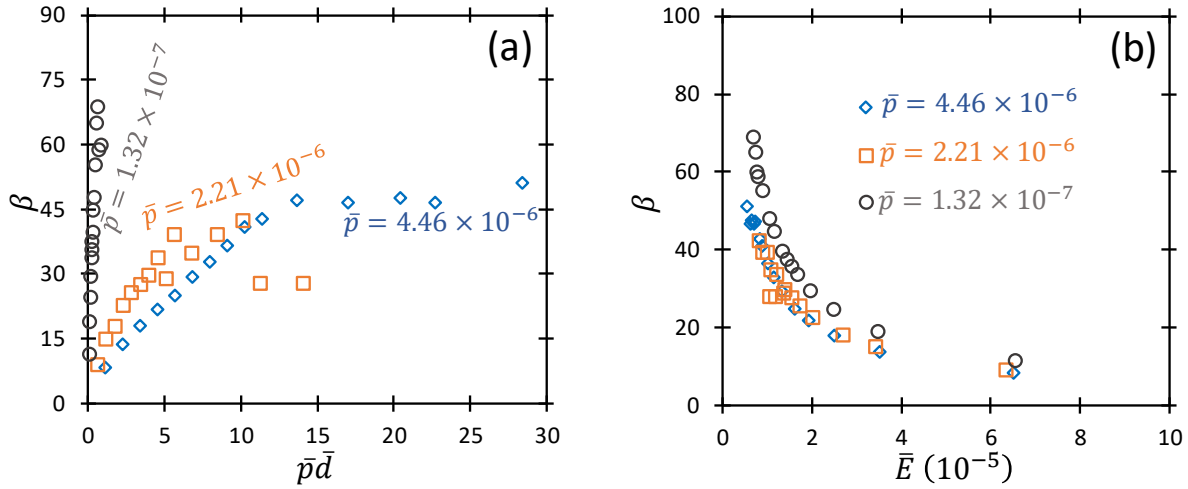


Figure 4.3. (a) Field enhancement factor, β , as a function of the product of the dimensionless pressure and gap distance, $\bar{p}\bar{d}$, obtained by fitting the experimental data from Figure 4.2. (b) Field enhancement factor, β , as a function of the dimensionless electric field, \bar{E} .

4.2.3 Parametric assessment of implications of material properties on transition to Paschen's law

Finally, we consider the impact of γ_{SE} , β , and $\bar{\phi}$, on the transition from the FE/TA regime to the UPL. Understanding how these parameters affect breakdown is vital for developing a predictive model, since γ_{SE} and β are difficult to determine *a priori* and the asymptotic prediction of V_B is very sensitive to variations in β and $\bar{\phi}$ in the FE/TA regime (Dynako, Loveless, & Garner, 2018). Thus, elucidating the influence of these terms on V_B will clarify the transition to UPL under

different p and d . The transition from the FE/TA regime to the UPL occurs when the limiting expression of equation (4-5) matches the UPL from equation (4-2), so we numerically solve

$$\frac{\bar{p}\beta|\Delta_2|}{\bar{\phi}^{3/2}\{\ln(\bar{p}\bar{d}) - \ln[\ln(1 + \gamma_{SE}^{-1})]\}} = 1 \quad (4-6)$$

for \bar{d} with a given γ_{SE} , β , and \bar{p} . Figure 4 shows the ratio of $\bar{p}\bar{d}$ for the transition, $(\bar{p}\bar{d})_{int}$, to the value corresponding to the standard ‘‘Paschen minimum’’ of equation (4-2) by setting $d\bar{V}/d(\bar{p}\bar{d}) = 0$ to give

$$(\bar{p}\bar{d})_{PL,min} = \exp\{1 + \ln[\ln(1 + \gamma_{SE}^{-1})]\}. \quad (4-7)$$

When $(\bar{p}\bar{d})_{int}/(\bar{p}\bar{d})_{PL,min} < (>)1$, equations (4-2) and (4-3) intersect to the left (right) of the traditional Paschen minimum. For example, at atmospheric pressure, $\beta = 60$, $\phi = 4.7$ eV, and $\gamma_{SE} = 10^{-4}$, the FE/TA model and the UPL intersect to the left of the Paschen minimum. However, reducing ϕ to 3 eV shifts the intersection to the right of the Paschen minimum. Figure 4a shows $(\bar{p}\bar{d})_{int}/(\bar{p}\bar{d})_{PL,min}$ as a function of \bar{p} for $\beta = 60$ and $\gamma_{SE} = 10^{-6}$ considering $\phi = 2, 3.5, 5,$ and 6 eV ($\bar{\phi} = 0.0207, 0.0362, 0.0516,$ and 0.0620) and Figure 4.4b shows $(\bar{p}\bar{d})_{int}/(\bar{p}\bar{d})_{PL,min}$ as a function of \bar{p} for various β at $\gamma_{SE} = 10^{-6}$. We note that ϕ does not have a significant effect on the transition point until $\bar{p} \approx 2 \times 10^{-6}$ (which corresponds to 380 Torr). We also observe the same behavior for any small value of γ_{SE} , such as $\gamma_{SE} = 10^{-6}$. This is analogous to previous observations that γ_{SE} does not play a vital role until TA dominates breakdown (often occurring somewhere around atmospheric pressure) (Loveless & Garner, 2017b;

Dynako, Loveless, & Garner, 2018). Figure 4.4b indicates that increasing β from 15 to 60 does not influence the transition point until $\bar{p} \approx 5 \times 10^{-6}$ (950 Torr). Reducing ϕ can shift the transition to the left of the PL minimum at subatmospheric pressures, but changing β does not shift the transition to the left of the minimum until the pressure exceeds atmospheric pressure. Varying γ_{SE} yielded similar behavior on the intersection with PL as changing β .

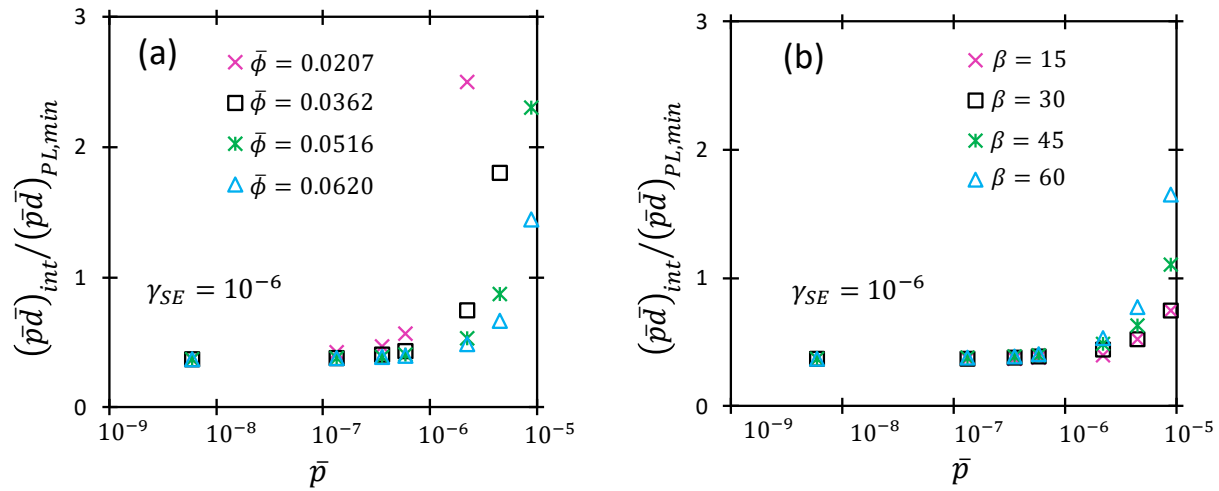


Figure 4.4. The ratio of the product of dimensionless pressure and gap distance, $\bar{p}\bar{d}$, causing the transition to Paschen's law, $(\bar{p}\bar{d})_{int}$, to $\bar{p}\bar{d}$ corresponding to the Paschen minimum, $(\bar{p}\bar{d})_{PL,min}$, as a function of \bar{p} for various values of (a) $\bar{\phi}$ with $\beta = 60$ and $\gamma_{SE} = 10^{-6}$, and (b) β with $\gamma_{SE} = 10^{-6}$ and $\bar{\phi} = 0.0465$. Figure (a) highlights that It is important to note that note that $\bar{\phi}$ does not have a significant effect on the transition point until $\bar{p} \approx 2 \times 10^{-6}$ (which corresponds to 380 Torr), and β does not influence the transition point until $\bar{p} \approx 5 \times 10^{-6}$ (950 Torr).

4.3 Conclusion

In summary, we applied a gas breakdown theory (Loveless & Garner, 2017b; Meng et al., 2018) to assess experimental results for breakdown voltage at various pressures. Using β as a fitting parameter, we achieved excellent agreement between the exact numerical solution of the theory and the experimental results, and demonstrated that the analytic model differed from experiment

by an average of 3.71%. We showed that experimental conditions, particularly electrode work function, can drive the intersection between the coupled FE/TA model and the UPL to the left or the right of the traditional Paschen minimum, providing a potential contributing factor determining whether V_B decreases with decreasing pd or an extended plateau occurs. Furthermore, the results showed that β and γ_{SE} have little influence on the location of the transition below atmospheric pressure, but ϕ has a greater influence. Future studies quantifying the change in work function (Li & Li, 2005) with multiple breakdown events will further elucidate how breakdown behavior changes with constant gap distance. For example, one can envision an initial work function leading to a transition to the UPL to the right of the minimum, with subsequent breakdown events occurring to the left after electrode surface damage potentially decreases work function if it enhances surface roughness (Li & Li, 2005). Future work quantifying how changes in work function due to surface roughness or chemical roughness (Kim, Hurtado, & Han, 1999) effect the system and incorporating thermionic emission (Jensen, 2018) into the model will enhance the utility and completeness of the model across multiple operating regimes. A more thorough understanding of this behavior is vital to accurately predict breakdown behavior and electron emission overall.

5. THE IMPACT OF CATHODE SURFACE ROUGHNESS AND MULTIPLE BREAKDOWN EVENTS ON MICROSCALE GAS BREAKDOWN AT ATMOSPHERIC PRESSURE

Reprinted from Brayfield, II, R. S., Fairbanks, A. J., Loveless, A. M., Gao, S., Dhanabal, A., Li, W., Darr, C., Wu, W. and Garner, A. L. (2019) The Impact of Cathode Surface Roughness and Multiple Breakdown Events on Microscale Gas Breakdown at Atmospheric Pressure, *Journal of Applied Physics*, 125, 203302, with the permission of AIP Publishing.

5.1 Introduction

Chapter 2 developed the universal model for dimensionless breakdown voltage, and Chapters 2 and 3 applied this model to various experimental data sets to provide analysis on the behavior of the emission mechanisms. This chapter similarly presents more detailed experimental results and applies the theory developed in Chapters 2-4. However, the data presented here aims to assess the impact of varying degrees of polishing on electrode surfaces. Thus, the main objective is to understand how different surface roughness values effect the work function, and—more importantly—the overall breakdown voltage of a system at a constant gap distance. Section 5.2 discusses the materials and methods employed, Section 5.3 presents the results of the experiments, Section 5.4 presents the theoretical assessment, and concluding remarks are made in Section 5.5. Russell Brayfield from the School of Aeronautics and Astronautics at Purdue University performed the experiments reported in this chapter. Agni Dhanabal from the Department of Agricultural and Biological Engineering performed the statistical analysis of the experimental data. Shengjie Gao from the School of Industrial Engineering performed the atomic force microscopy of the surface roughness. This work was published (Brayfield et al. 2019). The experimental portion of this work was performed at Purdue University, led by Russell Brayfield II.

5.2 Materials and Methods

5.2.1 Materials

The setup consists of tungsten dissection needles (Roboz Surgical Instrument Co., RS-6065) mounted into polyethylene to ensure electrical isolation. The copper plates were mounted to polyethylene blocks mounted to a micromanipulator and moved in increments of 1 μm . Figure 5.1 shows the micromanipulator setup with a fixed pin electrode.

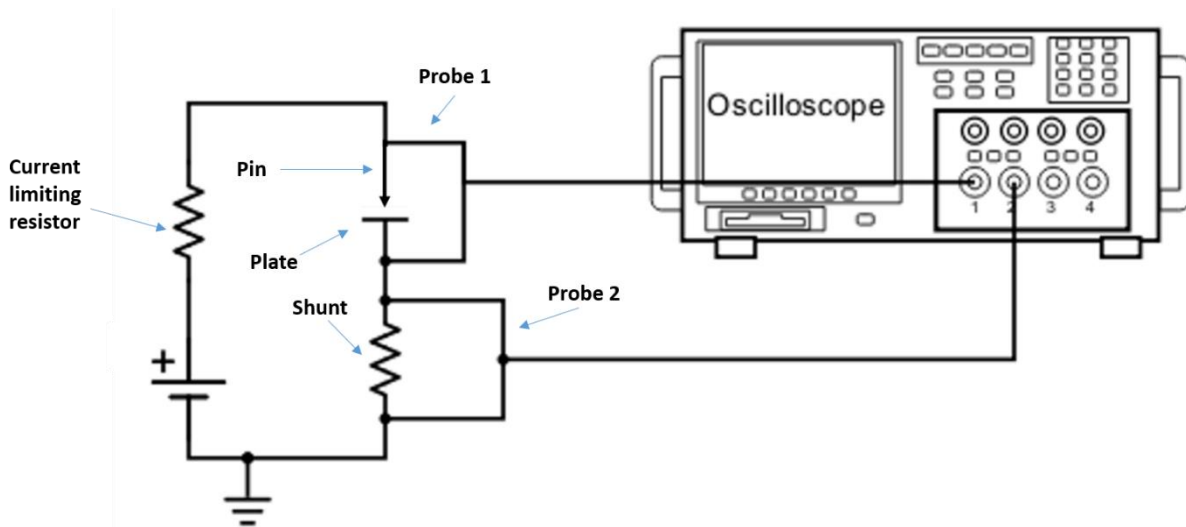


Figure 5.1. Schematic of the experimental setup showing the micromanipulator and pin mounting blocks.

The copper (Fire Mountain Gems, H20-9336FX) was cut into 12.7 mm² plates that were then polished to various degrees of surface roughness by using a wet polishing station with 400, 800, and 1200 grit polishing pads (Pace Technologies). After polishing, we soaked the plates in acetone to remove any surface contamination and rinsed them with water to remove any residue. AFM was then conducted to verify the absence of residue or polishing particulate on the surfaces. Table 5.1

reports the surface conditions under these initial AFM tests. A wire was soldered onto the back of the copper plate to provide electrical connections. Voltage and current measurements were made using an oscilloscope and two 100:1 voltage probes. One probe was connected across the pin to plate gap to measure the gap voltage and the second across a 1 M Ω resistor to determine the current. With the copper plate as the ground (cathode) and the tungsten needle as the “hot” electrode (anode), we used a high voltage supply (Stanford Research System, PS365, 10 kV) to apply DC voltage until discharge formation.

5.2.2 Methods

We divided each copper plate into sections for single breakdown event testing, ten breakdown event testing, and sample handling. We tested cathodes polished with each grit in triplicate for statistical purposes. We set the gap distance by applying 35 V to create a bias and using the micromanipulator to move the plate until it softly contacted the needle to create a “short” in the circuit before withdrawing the plate to the desired gap distance. This method was previously used to calibrate needle electrode distance with no effect on the surface (Bilici et al., 2016). To determine whether the contact phase of the setup damaged the surface, we used the micromanipulator to force a needle electrode into the surface. AFM was used to verify no significant change to the electrode surface was measurable. We considered gap distances of $1 \pm 0.5 \mu\text{m}$, $5 \pm 0.5 \mu\text{m}$, and $10 \pm 0.5 \mu\text{m}$ between the needle and the copper plate. Voltage was ramped at approximately 3 V/s from 100 V to breakdown, where an oscilloscope recorded the breakdown voltage and current waveforms. We removed the voltage immediately following the oscilloscope trigger to prevent further breakdown events. Since no current was present before breakdown, there was no voltage across the 1 M Ω resistor prior to breakdown, so this voltage served as an indication

of breakdown. We collected voltage and current waveforms for each breakdown event to compare breakdown voltage across events.

Breakdown for these tests was defined as the movement of electrons across the gap, creating a sustained dielectric breakdown of the gas. The current was limited using a ballast resistor to prevent damage to the anode and prevent large currents across the gap that would damage the tip. We observed no damage to the tungsten tips. The discharge event was measured by a shunt resistor that allowed us to monitor the current. When the current across the gap was detected by the oscilloscope, we immediately turned off the power supply to ensure that we only created a single breakdown event at a time. For the ten breakdown experiments, we waited one minute after each breakdown event before repeating. The relative humidity varied from 38-50% during the course of experiments.

We used atomic force microscopy (AFM) to quantify the change in surface roughness by measuring the average height of surface features before and after the breakdown events. Some breakdown induced surface features were too deep for AFM analysis and were estimated by altering the depth of field of an optical microscope to observe when the bottom of the feature was in focus compared to the surface.

5.3 Results

5.3.1 Cathode surface changes

Figure 5.2 shows the representative AFM data for the 800 grit polished cathode prior to breakdown experiments using a 5 μm gap. The optical images of the surface, such as Figure 5.2a, show the

general roughness of the surface. Figure 5.2b shows the contour map of the 800 grit sample with a maximum surface height of 200 nm and crater depth of 200 nm. Figure 5.2c shows the AFM tip deflection that measures the surface feature height. This was repeated for each sample to characterize the average surface features before the breakdown experiments. Table 5.1 presents the initial average surface feature height for the samples before breakdown events along the red dashed line in Figure 5.2b. The data in Table 5.1 was taken by averaging all of the peak to peak and RMS values for each grit.

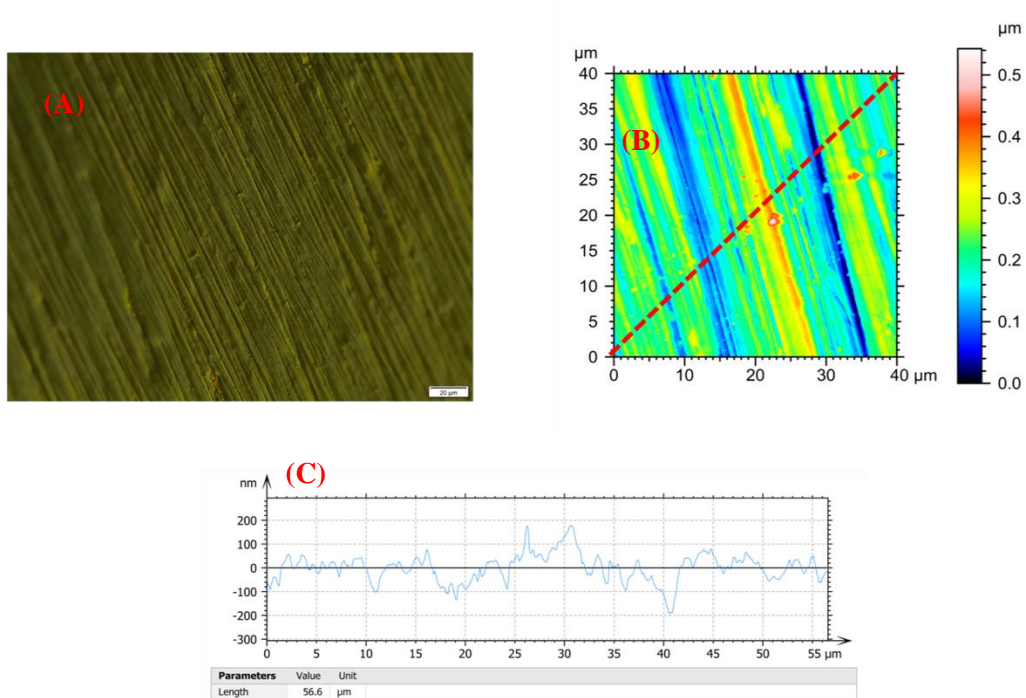


Figure 5.2. Atomic force microscopy (AFM) measurements of the 800 grit cathode prior to experiments showing the average surface features (a) Optical image of the surface visually showing the surface roughness. (b) Contour mapping of surface height along the surface. (c) AFM arm deflection showing height and depth of the surface features.

Table 5.1. Average surface features before breakdown tests.

| Grit | Number of samples | Peak to Peak Average (μm) | Standard Deviation (μm) | RMS (nm) |
|------|-------------------|--|--------------------------------------|----------|
| 400 | 9 | 1.47 | 1.08 | 535.22 |
| 800 | 9 | 0.26 | 0.18 | 65.99 |
| 1200 | 9 | 0.24 | 0.23 | 39.48 |

The breakdown events created small circular ablations on the samples at the test site. The ablation depth ranged from 3 to 50 μm and is reported in Table 5.2 for all samples containing them. The depth was so great that the samples could not be measured using AFM to quantify the surfaces without damaging the AFM tips. These results indicate that breakdown can cause significant surface modification, ablating material from a localized spot. Furthermore, the ablation depth is greatest for the cathodes with the largest average surface height (400 grit polished cathodes), which would be anticipated to have the highest field enhancement and, thus, be more susceptible to field emission driven breakdown. This suggests that the concentration of the discharges at the locations of higher surface height for the cathodes polished with 400 grit causes greater cathode damage compared to the 800 and 1200 grit samples, whose surface features are less sharp and will cause less field enhancement.

Table 5.2. Depth of the observed craters at the breakdown voltage for the cathodes polished at each grit where measurable ablation occurred.

| Grit (gap distance) | Depth (μm) | Grit (gap distance) | Depth (μm) | Grit (gap distance) | Depth (μm) |
|-------------------------|-------------------------|------------------------|-------------------------|--------------------------|-------------------------|
| 400 (10 μm) | 9.7 | 800 (5 μm) | 6.2 | 1200 (1 μm) | 12.1 |
| 400 (10 μm) | 6 | 800 (5 μm) | 7.4 | 1200 (1 μm) | 3.5 |
| 400 (10 μm) | 13.5 | 800 (5 μm) | 12.4 | 1200 (10 μm) | 4.8 |
| 400 (5 μm) | 41.2 | 800 (5 μm) | 5.3 | 1200 (10 μm) | 5.4 |
| 400 (5 μm) | 19.6 | 800 (5 μm) | 5.2 | | |
| 400 (1 μm) | 42.5 | | | | |

To determine whether the contact phase of the setup damaged the surface, we used the micromanipulator to force a needle electrode into the surface. AFM was used to verify no significant change to the electrode surface was measurable. The resulting absence of a circular mark indicated that the breakdown events, and not needle placement, damaged the surface. The absence of these marks on some samples following breakdown indicated that slight variations in surface polishing, which could influence the initial presence of surface structures, could sufficiently alter discharge path and subsequent surface ablation.

5.3.2 Changes in breakdown voltage

Figure 5.3 shows a representative waveform for a single breakdown event and the tenth breakdown event for a $5 \pm 0.5 \mu\text{m}$ gap distance with the cathode polished using 800 grit. The voltage remains relatively constant until breakdown occurs, as expected for an applied DC voltage. The breakdown voltage following the tenth event exceeded that for a single event, as shown in Figure 5.6. In this case, the first breakdown event occurred at 434.85 V while the tenth breakdown occurred at 523.25 V.

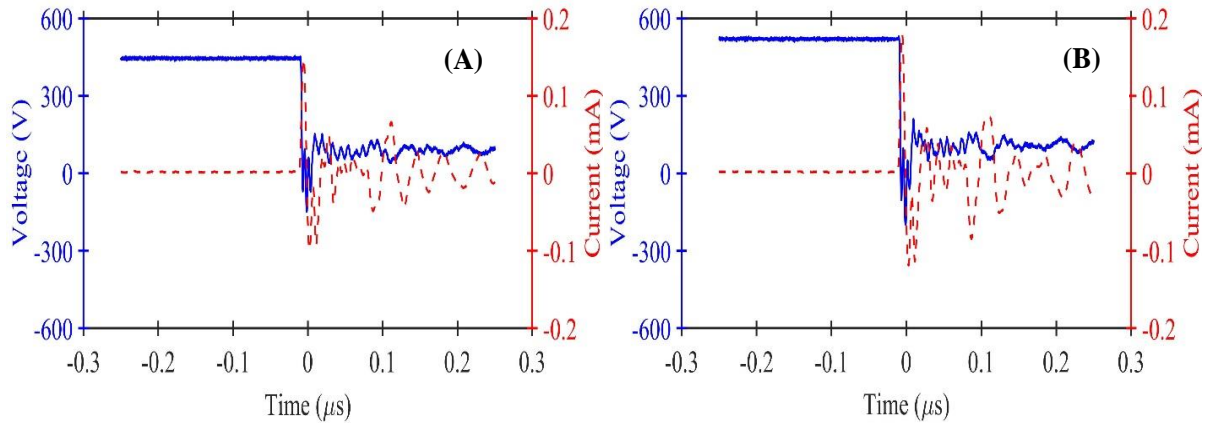


Figure 5.3. Representative voltage (solid) and current (dashed) waveforms for a $5 \pm 0.5 \mu\text{m}$ gap with the cathode polished using 800 grit for (a) a single breakdown event and (b) the tenth breakdown event. All breakdown events exhibited similar characteristics.

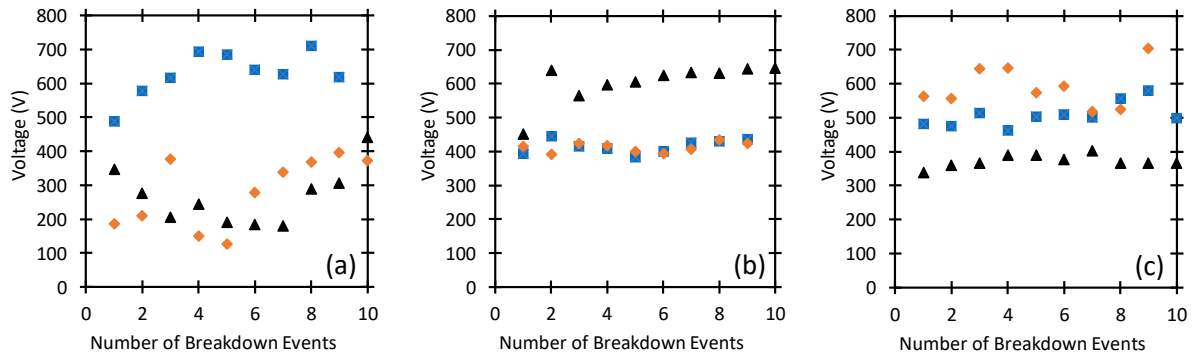


Figure 5.4. Breakdown voltage as a function of number of breakdown events for three individual trials for (a) 400 grit (b) 800 grit and (c) 1200 grit samples at $1 \mu\text{m}$ gap distance.

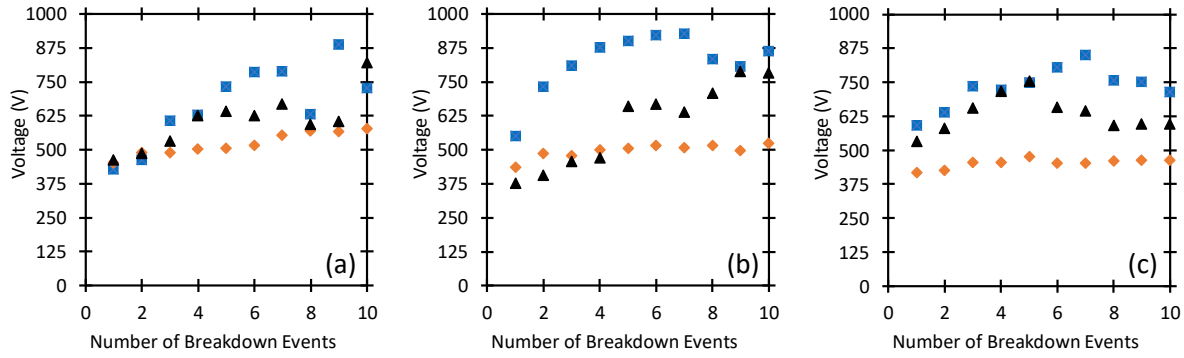


Figure 5.5. Breakdown voltage as a function of number of breakdown events for three individual trials for (a) 400 grit (b) 800 grit and (c) 1200 grit samples at 5 μm gap distance.

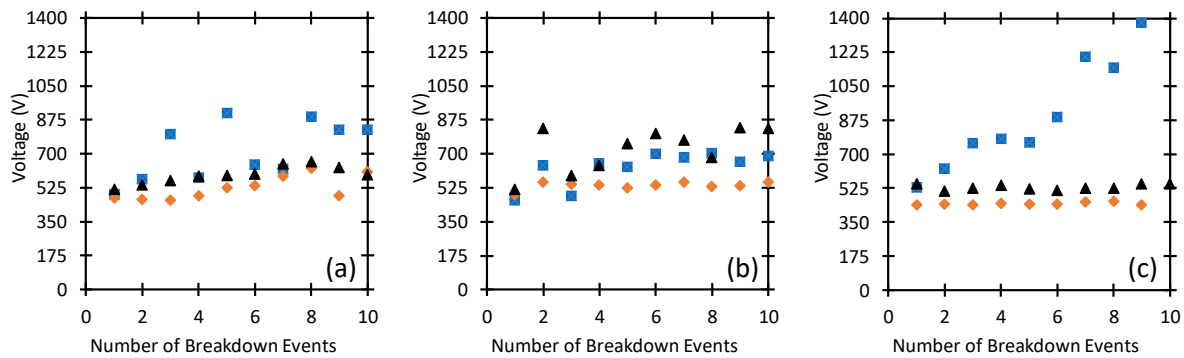


Figure 5.6. Breakdown voltage as a function of number of breakdown events for three individual trials for (a) 400 grit (b) 800 grit and (c) 1200 grit polished cathodes at 10 μm gap distance.

Figures 5.4 to 5.6 report the individual replicates for breakdown voltage as a function of the number of breakdown events for a 1, 5, and 10 μm gap with cathodes polished using 400, 800, and 1200 grit disks. Note that we did not achieve three repetitions for a few of the ten breakdown event cases due to either reaching high voltages for larger gap distances or slight sensitivity to micromanipulator position for smaller gap distances. Figure 5.7 reports the average values for a given grit. Generally, breakdown voltage increases with subsequent breakdown events, although this difference is not monotonic and noticeable variation occurs between samples.

Because the craters make noting distinct differences challenging, we ran a general linear model analysis of variance (ANOVA) with stepwise backward elimination to identify the statistically significant difference in means based on voltage as the response for each breakdown event (Minitab 18 software). Anderson-Darling normality tests showed no significance (p -values > 0.05), indicating normal distribution of residuals, except for the ninth pulse, which likely arises due to some outliers in our experimental dataset when reaching the limit of the micromanipulator travel tolerances. The ANOVA was followed by a Tukey pairwise comparison test at the 95% confidence level and adjusted p -values are reported due to the need for multiple comparisons. Grit did not exhibit any significance for any of the tests. Gap showed significant differences in means for voltage after at least five breakdown events ($p < 0.05$). Table 5.3 summarizes the adjusted p -values from the Tukey tests for significance. Breakdown voltages for 1 μm gap after at least five breakdown events differ statistically significantly from either the 5 μm and 10 μm gaps while the breakdown voltages following the fifth breakdown event for the 5 μm and 10 μm gaps do not exhibit any statistically significant difference.

Table 5.3. Adjusted p -values from Tukey tests comparing breakdown voltage for 5 μm and 1 μm gaps, 10 μm and 1 μm gaps, and 10 μm and 5 μm gaps for the fifth through tenth breakdown events. Conditions undergoing a statistically significant change are denoted with *. Generally, breakdown events after the fifth event yield a statistically significant breakdown voltage between the 1 μm gap and the other gap distance while no statistical significant difference arises between the 5 μm and 10 μm gaps.

| Breakdown Event | Difference between 5 μm and 1 μm | Difference between 10 μm and 1 μm | Difference between 10 μm and 5 μm |
|-----------------|---|--|--|
| 5 | 0.015* | 0.038* | 0.914 |
| 6 | 0.017* | 0.044* | 0.900 |
| 7 | 0.036* | 0.035* | 1.000 |
| 8 | 0.141 | 0.026* | 0.693 |
| 10 | 0.002* | 0.005* | 0.988 |

This behavior arises because the breakdown events alter the electrode surface, which also contributes to the increased variation after multiple events. First, each breakdown ablates the sharp-tipped features that contribute to field enhancement meaning that the applied voltage (and, thus, the electric field) for subsequent breakdown events must exceed the breakdown voltage for the initial event. The breakdown events additionally create craters on the surface that increase the effective gap distance, as shown by comparing Tables 5.1 and 5.2, further increasing the applied voltage to achieve the electric field necessary for breakdown. Thus, we anticipate that the combination of these phenomena will cause a general increase in breakdown voltage for subsequent breakdown events. This trend may not necessarily be monotonic since changes to the electrode surface structure (both electrode depth and field enhancement factor) may vary from event to event and across samples.

This suggests that the change in effective gap distance induced by crater formation plays a dominant role in breakdown voltage for multiple events. Table 5.4 shows that the crater depth is highest for the smallest gap distances, where field emission tends to drive breakdown (Go & Venkattraman, 2014; Meng et al., 2018; Fowler & Nordheim, 1928); Dynako, Loveless, & Garner, 2018), and for the cathode (400 grit) with the sharpest surface features, which would initially provide greater field enhancement to further drive field emission. Thus, we anticipate that the discharges under these conditions would focus on the sharp emitters during repeated breakdowns, resulting in greater cathode damage characterized by larger craters. These larger craters would create an increased effective gap distance, which also corresponds to a higher field enhancement factor in the combined field emission/Townsend avalanche regime since field enhancement increases with increasing gap distance in this regime (Bilici et al., 2016). Eventually, these larger

effective gap distances could also lead to a transition in breakdown mechanism from field emission to Townsend avalanche. Section 5.4 applies an asymptotic theory for microscale gas breakdown to confirm this hypothesis and quantify the contributions of the phenomena involved.

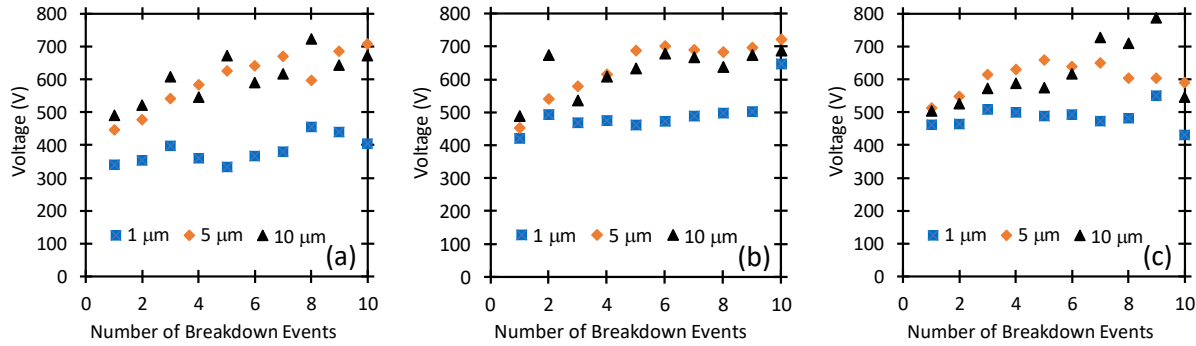


Figure 5.7. Average breakdown voltage as a function of number of breakdown events for (a) 400 grit (b) 800 grit and (c) 1200 grit for three trials each.

Figure 5.7 shows larger gap sizes did not always result in higher breakdown voltage, as one would intuitively expect. The variation in breakdown voltage is likely due to the crater formation, which leads to a larger effective gap. Table 5.4 presents the average crater depths for the conditions where craters occurred. Since this experiment only considered conditions after either a single breakdown event or after ten breakdown events, we did not record information on crater formation for intermediate conditions (i.e., the exact number of events when crater formation occurred).

Table 5.4. Average crater depth and breakdown voltage after the tenth breakdown event

| Grit | Starting Gap Distance (μm) | Average Crater Depth (μm) | Average Breakdown Voltage for 1 st Event (V) | Average Breakdown Voltage for 10 th Event (V) |
|------|---|--|---|--|
| 400 | 1 | 42.5 | 339 | 405 |
| 400 | 5 | 30.4 | 446 | 707 |
| 400 | 10 | 9.73 | 491 | 672 |
| 800 | 5 | 7.3 | 454 | 723 |
| 1200 | 1 | 7.8 | 462 | 432 |
| 1200 | 10 | 5.1 | 504 | 545 |

5.4 Theoretical Assessment

Table 5.4 summarizes the average crater depth for various grits and initial gap distances, along with the average breakdown voltage following the first and tenth breakdown events. Strictly speaking, we would need the crater depth after the ninth breakdown event to calculate the average breakdown voltage after the tenth event; however, the data indicates relatively slight variation between the breakdown voltage for the ninth and tenth events, so we use this crater depth for these calculations. Applying an “effective gap distance” that combines the initial gap distance with the crater depth allows us to assess the transition in breakdown mechanisms with crater formation, analogous to our previous theoretical studies (Loveless & Garner, 2016; Loveless & Garner, 2017b; Meng et al., 2018; Dynako, Loveless, & Garner, 2018). It is critical to point out that applying the theory to the *raw* data from Figs. 5.4 through 5.7 would lead to large variations in the fitting parameters; however, accounting for the crater depth using Table 5.2 dramatically reduces the relative error of the gap distances (particularly compared to the raw data), enabling the application of the theory (Dynako, Loveless, & Garner, 2018). While variation clearly remains (which motivated the study from Ref. Dynako, Loveless, & Garner, 2018), we apply the theory here to emphasize the behavior of breakdown voltage as a function of gap distance and the transitions in breakdown regime that we have observed elsewhere (Meng et al., 2018).

Table 5.5. Summary of parameters used in the theoretical analysis

| Parameter | Name | Value | Unit |
|---------------|--------------------------------|------------------------|------|
| ϕ | Work function | 4.7 | eV |
| ϕ_* | Work function scale | 96.81 | eV |
| d | Gap distance | Variable | m |
| L | Gap distance scale | 3.92×10^{-12} | m |
| p | Pressure | 760 | Torr |
| p_* | Pressure scale | 1.70×10^8 | Torr |
| E | Breakdown electric field | Variable | V/m |
| E_* | Breakdown electric field scale | 6.20×10^{12} | V/m |
| V | Breakdown voltage | Variable | V |
| V_* | Breakdown voltage scale | 24.3 | V |
| T | Temperature | 300 | K |
| T_* | Temperature scale | 7976 | K |
| β | Field enhancement factor | Variable | N/A |
| γ_{SE} | Secondary emission coefficient | 10^{-5} | N/A |

We start from our previously-derived universal gas breakdown model (Loveless & Garner, 2017b),

given by

$$\frac{\exp[\bar{\phi}^{3/2}/(\beta\bar{E})]}{\beta\bar{\phi}^{1/2}\exp(\bar{\phi}^{-1/2})}\sqrt{\frac{\bar{T}\bar{E}}{\bar{p}\bar{d}_{eff}^2}}\frac{\{1-\gamma_{SE}[\exp(\bar{\alpha}\bar{d}_{eff})-1]\}}{\exp(\bar{\alpha}\bar{d}_{eff})-1}=\exp(1)(1+2\bar{E}), \quad (5-1)$$

where $\bar{E} = E/E_*$ is the dimensionless breakdown field, $\bar{d}_{eff} = \bar{d} + \bar{\delta} = (d + \delta)/L$ is the effective dimensionless gap distance with \bar{d} the dimensionless electrode gap distance and $\bar{\delta}$ the dimensionless crater depth, $\bar{\phi} = \phi/\phi_*$ is the dimensionless work function, $\bar{p} = p/p_*$ is the

dimensionless pressure, $\bar{T} = T/T_*$ is the dimensionless gas temperature, and Table 4.5 defines all other parameters and provides typical values.

We numerically solve (5-1) for \bar{E} and apply $V = \bar{E}\bar{d}_{eff}E_*L$ to obtain the breakdown voltage in volts using β as a fitting parameter. Furthermore, since the product of the ionization coefficient α and d exceeds unity (specifically, $1.1 < \bar{\alpha}\bar{d}_{eff} = \bar{p}\bar{d}_{eff} \exp(\bar{p}\bar{d}_{eff} \exp(-1)) < 50$, where $\bar{\alpha}=\alpha L$), we apply the analytic equation for breakdown voltage for $\bar{\alpha}\bar{d} \gg 1$ from (Venkatraman & Alexeenko, 2012), given by

$$V = (E_*L \bar{d}_{eff}/\Lambda_2) \left[-\Delta_2 - (\Delta_2^2 - 2\Lambda_2\bar{\phi}^{3/2}/\beta)^{1/2} \right], \quad (4-2)$$

where $\Delta_2 = -[\bar{\mu} + \bar{\nu}]$ and $\bar{\mu} = \ln(\Lambda_2)/2 + \ln(\beta\bar{\phi}^{1/2}) + \bar{\phi}^{-1/2} + 3/2$ and $\bar{\nu} = \ln\{\exp[\bar{p}\bar{d}_{eff} \exp(-1)] - 1\} - \ln\{1 - \gamma_{SE}[\exp(\bar{p}\bar{d}_{eff} \exp(-1))]\} - \ln[\bar{T}\bar{p}^{-1}\bar{d}_{eff}^{-2}]/2$

represent the field emission and Townsend contributions, respectively, and $\Lambda_2 = 10^{-5}$ is a fitting parameter. Figure 5.8 shows the experimental results, the calculations from (5-1) and (5-2), and the values of $\bar{\alpha}\bar{d}_{eff}$ (note that $\bar{\alpha}\bar{d}_{eff} = \alpha d_{eff}$ since both quantities are scaled by L). From Meek's criterion (Loeb & Meek, 1941), $\bar{\alpha}\bar{d}_{eff} \approx 18$ corresponds to the transition to streamer formation, making (5-1) and (5-2) no longer valid (in fact, (5-2) is unsolvable for these points). Although we have addressed this limitation to this theory in previous studies (Loveless & Garner, 2016; Loveless & Garner, 2017b; Meng et al., 2018), this experimental condition is unique in that we start in the field emission regime and then transition to the Townsend and streamer regimes without changing the physical gap distance. Current theory does not address the transition to streamer

discharge at microscale, so we note the potential transition in the current study. The results of (5-1) and (5-2) differ by ~10% except for the two largest gap distances where $\bar{\alpha}d_{eff} > 18$ and (5-2) cannot be solved.

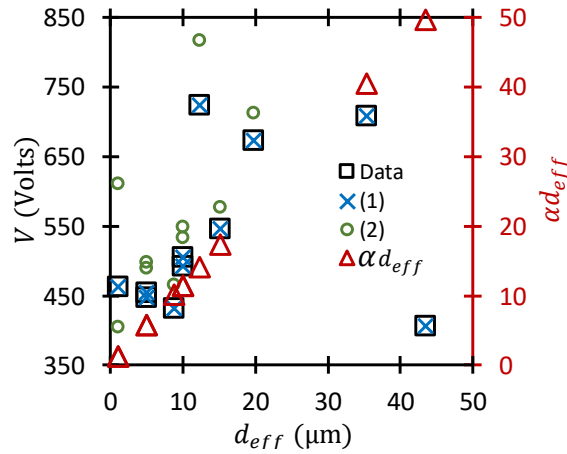


Figure 5.8. Average breakdown voltage, V , as a function of effective gap distance, $d_{eff} = d + \delta$, where d is the anode-cathode gap and δ is the breakdown induced crater depth, compared to numerical results from (5-1) and analytic results from (5-2). The product of the ionization coefficient and effective gap distance, αd_{eff} , is displayed on the secondary vertical axis as a function of d_{eff} . The largest two gap distance points have $\alpha d_{eff} \gg 18$, which exceeds Meek's criterion for streamer formation.

Figure 5.9(a) shows β for fitting the model to experimental data. Interestingly, β varies linearly with d_{eff} until the largest gap distances, excluding the outlier at $d_{eff} \approx 12 \mu\text{m}$. At the largest gaps, β becomes approximately constant. This behavior is similar to our previous application of this theory to experimental results for single breakdown events at microscale, where β increased linearly until Townsend avalanche began to dominate (Meng et al., 2018). Furthermore, the transition from linear to constant β occurs approximately when $\bar{\mu} = \bar{v}$, or when breakdown begins to transition from field emission to the traditional Paschen law (Paschen, 1889; Fowler & Nordheim, 1928;

Dynako, Loveless, & Garner, 2018; Loveless & Garner, 2017a). Figure 5.9(b) shows that $\alpha d_{eff} \approx 10$ at this transition.

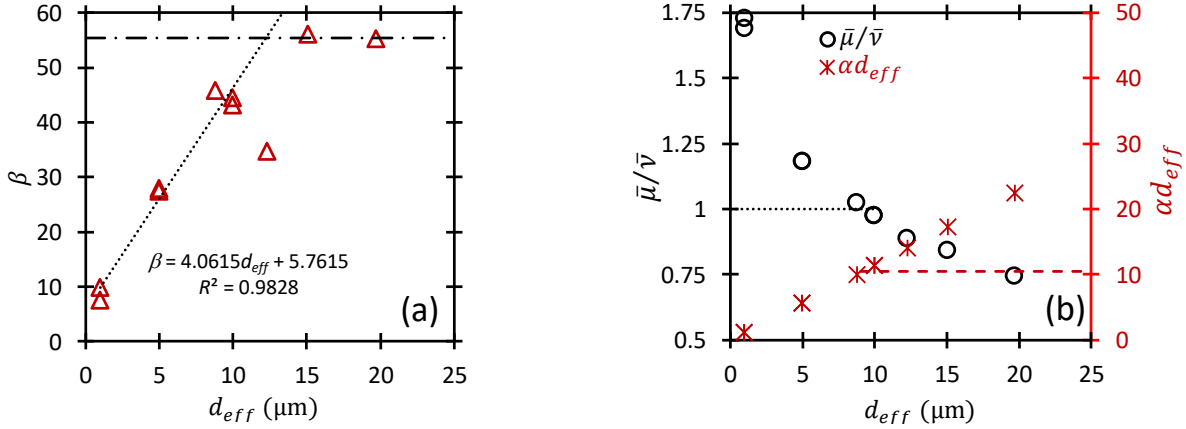


Figure 5.9. (a) Field enhancement factor, β , as a function of effective gap distance, $d_{eff} = d + \delta$, where d is the gap distance and δ is the crater depth, showing that β is approximately linear until the larger gap distances corresponding to the transition to Townsend avalanche, where it becomes constant. (b) The ratio of the field emission component to the Townsend component, $\bar{\mu}/\bar{\nu}$, as a function of d_{eff} , demonstrating that field emission effects govern breakdown until $d_{eff} \approx 10 \mu\text{m}$, which corresponds to $\alpha d_{eff} \approx 10$. This point coincides with the transition of β from linear to constant in (a), indicating the transition to the traditional Paschen's law.

Upon transition to Paschen's law, the experimental data and numerical results from (5-1) agree well with the universal Paschen's law (UPL) (Loveless & Garner, 2017b), given by

$$V = \frac{(\bar{p}\bar{d}_{eff})}{\ln(\bar{p}\bar{d}_{eff}) - \ln[\ln(1 + \gamma_{SE}^{-1})]} (E_*L). \quad (5-3)$$

Figure 5-10(a) shows the experimental results, the numerical results from (5-1), and the results of (5-3) using $\gamma_{SE} = 1.5 \times 10^{-3}$, which we selected based as reasonable based on previous studies (Loveless & Garner, 2017b; Meng et al., 2018; Dynako, Loveless, & Garner, 2018) and agreement with the experimental data. The calculations from (5-1) for the asymptotic solution match (5-3) for the UPL when $\alpha d_{eff} \approx 10$, corresponding to the transition from the combined field emission and Townsend

regime to the traditional Paschen's law, and deviate once αd_{eff} becomes sufficiently large for streamer formation. Alternatively, noting that the transition to Paschen's law occurs when $\alpha d_{eff} \approx 10$, we can calculate γ_{SE} to match the experimental results by solving (5-3) to obtain $\gamma_{SE} = \{\exp[\bar{p}\bar{d}_{eff} \exp(-\bar{p}\bar{d}_{eff}/\bar{V})] - 1\}^{-1}$. Future work will aim to better characterize γ_{SE} and further assess streamer formation and behavior.

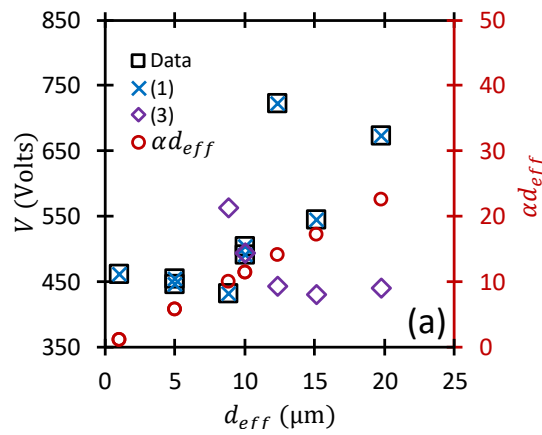


Figure 5.10. (a) Breakdown voltage, V , as a function of effective gap distance, $d_{eff} = d + \delta$, where d is the gap distance and δ is the crater depth, from the experimental data, the numerical results of (5-1), and the analytic results of (5-3) assuming $\gamma_{SE} = 1.5 \times 10^{-3}$. The product of the ionization coefficient and effective gap distance, αd_{eff} , is shown on the secondary vertical axis.

The transition to Paschen's law occurs for $\alpha d_{eff} \approx 10$ and breakdown becomes driven by streamer formation when $\alpha d_{eff} > 18$.

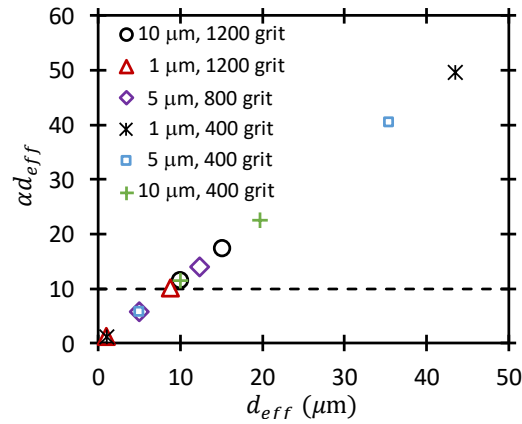


Figure 5.11. The product of the ionization coefficient and effective gap distance, αd_{eff} , as a function of the effective gap distance, $d_{eff} = d + \delta$, where d is the gap distance and δ is the crater depth. Each pair of symbols shows the αd_{eff} value after the first and tenth breakdown events, showing that crater formation can push breakdown behavior past the $\alpha d_{eff} \approx 10$ criterion for transition to Paschen's law.

Finally, we theoretically assess the impact of crater formation on breakdown voltage. Figure 5.11 summarizes the six sets of data, showing αd_{eff} after the one and ten breakdown events. Notably, the data from the samples with initial gap distances of 1 and 5 μm had $\alpha d_{eff} < 10$ after the first breakdown event, but transitioned to $\alpha d_{eff} > 10$ after the tenth breakdown event, indicating that crater formation alone can push the breakdown mechanism into the Townsend regime even if the anode-cathode gap remains unchanged. This could have significant implications on device design, where many breakdown events are expected to occur and breakdown voltage is expected to remain constant. Moreover, this suggests that eventually, subsequent breakdown events will not increase crater depth much since one transitions to the Townsend regime, where field enhancement diminishes, reducing the localization of breakdown that occurs at smaller gaps in the field emission

regime. This suggests that most sensitivity to the influence of surface effects in breakdown occurs when operating in the field emission regime with rough cathodes, where the higher electric fields lead to greater crater formation and noticeable changes in breakdown voltage and electrode conditions.

5.5 Conclusion

These results show the dependence of breakdown voltage on repeated breakdown events for a pin-to-plate configuration at microscale gaps and atmospheric pressure. With a polished copper plate as the cathode and a tungsten dissection needle as the anode, we measured the breakdown voltage for 1, 5, and 10 ± 0.5 μm gaps. We polished the cathodes using 400, 800, and 1200 grit papers with a wet polishing machine to vary the surface roughness. Figs. 5.4 through 5.6 show that the change in breakdown voltage due to surface roughness for a fixed gap distance or due to gap distance for a fixed surface roughness were not statistically significant. The major change in behavior involved the variation in breakdown voltage due to cathode crater formation. AFM and optical imaging before and after the breakdown events showed that the cathodes changed from having average surface feature heights ranging from 0.24 to 1.47 μm before the events to containing small ablated regions with crater depths ranging from 3 to 50 μm (cf. Table 5.2). The combination of initial surface feature height and the ablation/melting of surface material changed the effective gap distance of the system. Cathode crater formation drove the changes by increasing the effective gap distance, which increased breakdown voltage for multiple breakdown events. We observed similar breakdown voltages for similar effective gap distances independent of the interelectrode spacing. Applying a matched asymptotic analysis to the experimental results demonstrated that the breakdown voltage was a function of the effective gap distance and that the

transition from field emission to Townsend avalanche occurred at effective gap distances equivalent to the gap distances observed for single breakdown studies (Loveless & Garner, 2017b; Meng et al., 2018). Moreover, β varied linearly with gap distance in the field emission regime before becoming constant at the transition to the Townsend avalanche, as observed for single breakdown studies (Meng et al., 2018). Interestingly, we observed a change in breakdown mechanism from field emission to Townsend avalanche to streamer discharge at a single interelectrode gap distance due to crater formation. Thus, for microscale devices, changes in electrode surface can play a major role in breakdown voltage for multiple uses, particularly for rough surfaces where field emission dominates, leading to concentration of discharge formation at the emission sites that creates large craters.

While the current study focused on the breakdown voltage and surface structure, predominantly cathode feature height or depth, sensitivity analysis of breakdown theory indicates that microscale gas breakdown voltage also depends strongly on work function (Dynako, Loveless, & Garner, 2018). Future studies will extend the analysis to assess changes in work function with repeated breakdown events to ascertain the relative contribution on gas breakdown, particularly when uncertainty in work function and field enhancement dominate the sensitivity of breakdown voltage predictions for gap distances below 10 μm (Dynako, Loveless, & Garner, 2018). Although mean surface roughness did not impact the breakdown voltage, it did lead to concentration of the discharge at emission sites that impacted subsequent breakdown events; however, this study did not consider the impact of a single, controllable sharp-tipped emitter on breakdown voltage. Future studies will thus further investigate the impact of controllable aspect ratio (Lin et al., 2017) as a function of gap distance and pressure on gas breakdown and current density to additionally

characterize transitions between electron emission mechanisms (Bogue, 2007; Zhang et al., 2017) and breakdown phenomena.

6. UNIFICATION OF ELECTRON EMISSION AND BREAKDOWN MECHANISM THEORIES FROM QUANTUM SCALES TO PASCHEN'S LAW

Loveless, A. M., Darr, A. M., and Garner, A. L. (2020) Unification of electron emission and breakdown mechanism theories from quantum scales to Paschen's law, *Physical Review Research*, Submitted.

6.1 Introduction

The previous chapters assessed gas breakdown dynamics at microscale, particularly the transition from field emission to Townsend avalanche and, ultimately, Paschen's law. As we further reduce gap size, electron emission will transition from field emission at low voltage to space-charge limited emission at high voltage. This work aims to incorporate further emission mechanisms into the breakdown model to accurately predict electron emission behavior at all scales. This includes Child-Langmuir and Mott-Gurney at space-charge-limited regimes and Schrödinger's one-dimensional wave equation at nanoscales when single particle effects become important. Figure 6.1 summarizes the flow of emission mechanisms with increasing gap distance and pressure from left to right. Section 6.2 details the current model development for this assessment. Section 6.3 presents current results, and Section 6.4 includes concluding remarks. This work modifies that from Darr, Loveless, and Garner (2019) by modifying the scaling parameters to additionally account for Schrödinger's one-dimensional wave equation.

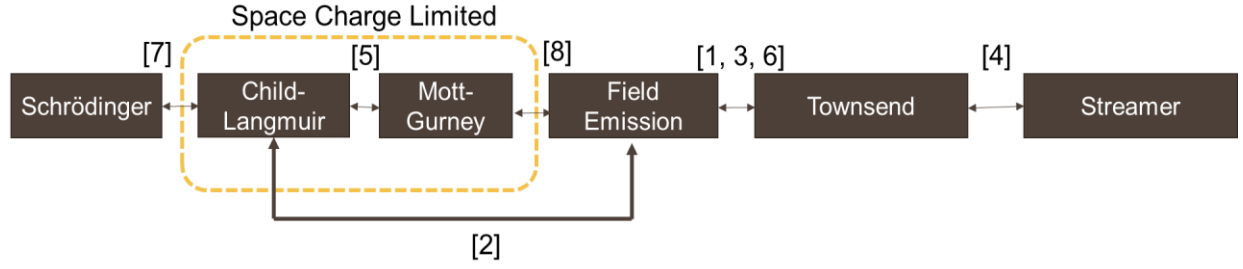


Figure 6.1. Summary of emission mechanisms from nanoscale to microscale with [1] Venkatraman & Alexeenko, 2012); [2] Lau, Liu, & Parker, 1994); [3] Go & Pohlman, 2010; [4] Warne, Jorgenson, & Nicolaysen, 2003; [5] Benilov, 2009; [6] Loveless & Garner, 2017b; [7] Lau et al., 1991; and [8] Darr, Loveless, & Garner, 2019.

6.2 Model Development

We start by defining the governing equations. For the Townsend avalanche regime, the standard PL is given by (Paschen, 1889; Loveless & Garner, 2017b)

$$V = \frac{Bpd}{\ln(Apd) - \ln[\ln(1 + \gamma_{SE}^{-1})]} \quad (6-1)$$

where V is the breakdown voltage, p is the gas pressure, d is the gap distance, γ_{SE} is the secondary electron emission coefficient, and A and B are gas dependent parameters.

For the coupled PL/FN regime (what we consider the “microscale” regime, in general), we considered the coupled breakdown criterion given by (Go & Pohlman, 2010)

$$\frac{2E^2 v_d \epsilon_0 \{1 - \gamma_{SE} [\exp(\alpha d) - 1]\}}{D_{FN} d J_{FN} [\exp(\alpha d) - 1]} = \frac{\exp(x_0) (1 + 2\tilde{E} x_0)}{x_0}, \quad (6-2)$$

where E is the breakdown electric field, α is the ionization coefficient, v_d is the drift velocity, J_{FN} is the Fowler-Nordheim current, D_{FN} is a field emission parameter, $\tilde{E} = E/D_{FN}$, and x_0 is a function of E . While this formulation assumes a uniform E , recent efforts have been made to generalize this assumption (Fu, Krek, Zhang, & Verboncoeur, 2018)

Next, we consider the transitions between FN and space-charge limited emission with CSCL at vacuum and MG with collisions by starting from Poisson's equation, given by (Lau, Liu, & Parker, 1994; Darr, Loveless, & Garner, 2019)

$$\frac{d^2V}{dx^2} = \frac{J}{\epsilon_0 v'} \quad (6-3)$$

where x is the position, J is the current density, and v is the electron velocity, and a force balance that incorporates electron mobility μ as

$$m \frac{dv}{dt} = e \frac{dV}{dx} - \frac{ev}{\mu}, \quad (6-4)$$

where m is the electron mass and e is the electron charge.

For the CSCL to QSCL transition we consider (3), Schrödinger's 1D wave equation, given by (Lau, Chernin, Colombant, & Ho, 1991)

$$\frac{\hbar^2}{2m} \frac{d^2\psi}{dx^2} - eV\psi = U\psi, \quad (6-5)$$

where ψ is the wave function and U is the electron injection energy, and the quantum mechanical current density for a single eigenfunction as

$$J = e \left(\frac{i\hbar}{2m} \right) [\psi\psi^{*'} - \psi^*\psi'], \quad (6-6)$$

where ' represents a derivative with respect to position and * represents the complex conjugate.

Equations (6-1)-(6-6) describe the emission behavior from the 1D wave equation to the traditional PL. Nondimensionalizing the governing equations by deriving a single set of consistent scaling parameters across mechanisms reduces the number of constants and material-dependent terms. This allows us to focus on the underlying physical mechanisms driving the emission behavior. The dimensionless variables and scaling parameters for this analysis are given by

$$\begin{aligned} \bar{p} &= pp_*^{-1}, \bar{d} = dL^{-1}, \bar{T} = TT_*^{-1}, \bar{\alpha} = \alpha L, \bar{\mu} = \mu\mu_*^{-1}, \bar{J} = Jj_0^{-1}, \\ \bar{\psi} &= \psi\psi_*^{-1}, \bar{E} = EE_*^{-1}, \bar{t} = tt_*^{-1}, \end{aligned} \quad (6-7)$$

With

$$p_* = E_*/B_p \text{ [Torr]}, E_* = D'_{FN} = 0.95B_{FN}\phi_*^{3/2} \text{ [V/m]}, j_0 = C'_{FN}E_*^2 \text{ [A/m}^2\text{]},$$

$$T_* = \frac{\pi m_g \sigma_{CE}}{2ekB_p} \left(\frac{C'_{FN} D'_{FN} L^2 A_p p_*}{2\varepsilon_0} \right)^2 \text{ [K]}, L = \left(\frac{\hbar}{2m_e e E_*} \right)^{1/3} \text{ [m]}, t_*^2 = \frac{m_e L}{e E_*} \text{ [s}^2\text{]}, \quad (6-8)$$

$$\mu_* = \frac{et_*}{m_e} \text{ [m}^2\text{/Vs]}, \phi_*^{1/2} = \left(\frac{2A_{FN}^3 m_e \hbar (0.95B_{FN})}{(\varepsilon_0 \tau^2(\gamma))^3 e^2} \right)^{1/3} \text{ [eV}^{1/2}\text{]}, \psi_*^2$$

$$= \varepsilon_0 E_*/(eL) \text{ [m}^{-3}\text{]},$$

respectively, with the dimensions given in brackets, $C'_{FN} = A_{FN}(\phi_*\tau^2(\gamma))^{-1}$, and $D'_{FN} = 0.95B_{FN}\phi_*^{3/2}$. Two additional parameters included are a dimensionless constant given by $\Gamma = (3.79 \times 10^{-4})^2 B_{FN}/\phi_*^{1/2}$, and a single material-dependent term given by $\Omega = A_p E_* L/B_p$. Thus, the model is not completely universal due to the material-dependent term remaining in PL. Appendix C gives a detailed derivation of the full dimensionless model.

Applying (6-7) and (6-8) to (6-1)-(6-6), solving the equation of motion, and taking various limits (cf. Appendix C) gives a set of dimensionless equations characterizing electron emission and gas breakdown from QSCL to PL as

$$\frac{1}{\bar{U}} \frac{d^2 q(\bar{x})}{d\bar{x}^2} + \left[\left(\frac{\bar{V}}{\bar{U}} + 1 \right) - \frac{(\lambda_q/4)^2}{[q(\bar{x})]^4} \right] q(\bar{x}) = 0; \quad (6-9)$$

$$\frac{d^2 \bar{V}}{d\bar{x}^2} = [q(\bar{x})]^2; \bar{J} = 2\theta'(\bar{x})q^2(\bar{x}); \lambda_q = \frac{2\bar{J}}{\bar{U}^{1/2}},$$

for QSCL (cf. Appendix C 1),

$$\bar{J}_{CSCL} = \frac{8\bar{V}^{3/2}}{9\bar{d}^2}, \quad (6-10)$$

$$\bar{J}_{MG} = \frac{9\sqrt{2}\bar{\mu}\bar{V}^2}{8\bar{d}^3}, \quad (6-11)$$

$$\bar{J}_{FN} = \frac{\bar{V}^2\beta^2}{\bar{d}^2\bar{\phi}} \exp\left(-\frac{\bar{\phi}^{3/2}\bar{d}}{\beta\bar{V}}\right) \exp\left(\frac{\Gamma}{\bar{\phi}^{1/2}}\right), \quad (6-12)$$

for CSCL, MG, and FN (cf. Appendix C 2),

$$\begin{aligned} & \frac{2\varepsilon_0 \exp\left(\frac{\bar{\phi}^{3/2}}{\beta\bar{E}}\right) \tau^2(y)}{0.95B_{FN}\phi_*^{1/2}\bar{\phi}^{1/2}LA_{FN}\beta \exp(\Gamma/\bar{\phi}^{1/2})} \sqrt{\frac{2ekT_*B_p}{\pi m_g\sigma_{ce}}} \sqrt{\frac{\bar{T}\bar{E}}{\bar{p}\bar{d}^2}} \times \\ & \times \frac{\{1 - \gamma_{SE}[\exp(\bar{\alpha}\bar{d}) - 1]\}}{[\exp(\bar{\alpha}\bar{d}) - 1]} = \frac{\exp(x_0)(1 + 2\bar{E}x_0)}{x_0}, \end{aligned} \quad (6-13)$$

where $x_0 = (\sqrt{1 + 8\bar{E}} - 1)/(4\bar{E})$ for microscale (cf. Appendix C 3), and

$$\bar{V} = \frac{\bar{p}\bar{d}}{\ln(\Omega\bar{p}\bar{d}) - \ln[\ln(1 + \gamma_{SE}^{-1})]} \quad (6-14)$$

for Paschen's law (PL) (cf. Appendix C 4). The Appendix details this derivation and provides further information on the exact, analytic, and limiting solutions for both the microscale region and the CSCL/MG/FN regimes. Table 6.1 summarizes the parameters used in the theory.

Table 6.1. Summary of scaling parameters used in calculations for air.

| Symbol | Quantity | Value |
|---------------|---|---|
| A_p | gas parameter | $15 \text{ cm}^{-1}\text{Torr}^{-1}$ |
| B_p | gas parameters | $365 \text{ V cm}^{-1}\text{Torr}^{-1}$ |
| m | mass of gas atom | $4.81 \times 10^{-26} \text{ kg}$ |
| A_{FN} | Fowler-Nordheim parameter | $6.2 \times 10^6 \text{ A eV V}^{-2}$ |
| B_{FN} | Fowler-Nordheim parameter | $6.85 \times 10^9 \text{ V m}^{-1} \text{ eV}^{-3/2}$ |
| ϕ | work function | 5.15 eV |
| β | field enhancement factor | 50 |
| $v(y)$ | elliptic function | $0.95 - y^2$ |
| y | elliptic function | $3.79 \times 10^{-4} \sqrt{\beta E} / \phi$ |
| $\tau^2(y)$ | elliptic function | 1.1 |
| Γ | dimensionless factor | $(3.79 \times 10^{-4})^2 B_{FN} / \phi_*^{1/2}$ |
| e | electron charge | $1.6 \times 10^{-19} \text{ C}$ |
| k | Boltzmann's constant | $1.38 \times 10^{-23} \text{ J K}^{-1}$ |
| ϵ_0 | permittivity of free space | $8.854 \times 10^{-12} \text{ F m}^{-1}$ |
| σ_{CE} | charge exchange cross section | 10^{-18} m^2 |
| γ_{SE} | secondary electron emission coefficient | 10^{-3} |
| T | Temperature | 300 K |

6.3 Results

We determined the transitions between the various emission mechanisms by equating their various asymptotic solutions. For a given gap distance and injection energy, we may numerically solve for the voltage that yields a QSCL current density equal to that from (6-10), representing the transition point between QSCL and CSCL. Similarly, equating (6-10) and (6-11) and solving for \bar{V} as a function of either \bar{d} or $\bar{\mu}$ gives the transition between CSCL and MG as

$$\bar{V} = \left(\frac{64\sqrt{2}\bar{d}}{162\bar{\mu}} \right)^2. \quad (6-15)$$

An analogous procedure equating (6-10) to (6-12) and (6-11) to (6-12) yields

$$\bar{V}^{-1/2} \exp\left(\frac{\bar{\phi}^{3/2}\bar{d}}{\beta\bar{V}}\right) = \frac{9\beta^2}{8\bar{\phi}} \exp\left(\frac{\Gamma}{\bar{\phi}^{1/2}}\right), \quad (6-16)$$

for the transition from CSCL to FN and

$$\bar{V} = \frac{\bar{\phi}^{3/2}\bar{d}}{\beta} \left[\frac{\Gamma}{\bar{\phi}^{1/2}} - \ln\left(\frac{9\sqrt{2}}{8} \frac{\bar{\mu}\bar{\phi}}{\beta^2\bar{d}}\right) \right]^{-1}, \quad (6-17)$$

for the transition from MG to FN. The intersection of the transitions from (6-15) to (6-17) defines a nexus where the asymptotic solutions for CSCL, MG, and FN match. Although the experimental

implications of this triple point, or third order nexus, require further investigation, one immediate consequence is that the dominant electron emission mechanism in this regime will be very sensitive to experimental conditions, such as gap distance, pressure, and electrode design, making it very easy to transition between the mechanisms.

Figure 6.2 demonstrates the importance of the dimensionless, material-dependent term Ω in the dimensionless PL given by (6-14). While \bar{V} depends strongly on gas at small $\bar{p}\bar{d}$, this dependence decreases for increasing $\bar{p}\bar{d}$ to the right of the minimum.

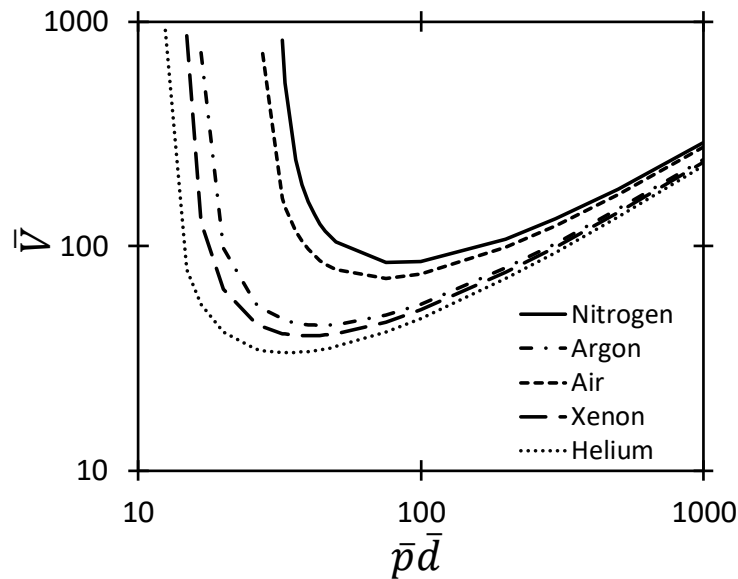


Figure 6.2. Dimensionless breakdown voltage, \bar{V} , as a function of the product of dimensionless pressure and gap distance, $\bar{p}\bar{d}$, for various gases with $\gamma_{SE} = 10^{-3}$, calculated with the dimensionless PL using (6-14). One material parameter remains in (6-14), preventing it from being universal (true for any gas).

Figure 6.3 demonstrates the dependence of \bar{V} on \bar{d} for different dimensionless pressures \bar{p} for nitrogen. Increasing \bar{p} shifts the minimum \bar{V} to the left, as expected based on the typical $\bar{p}\bar{d}$

scaling of the traditional PL. Thus, as \bar{p} increases, \bar{d} decreases proportionally so that $\bar{p}\bar{d}$ remains constant.

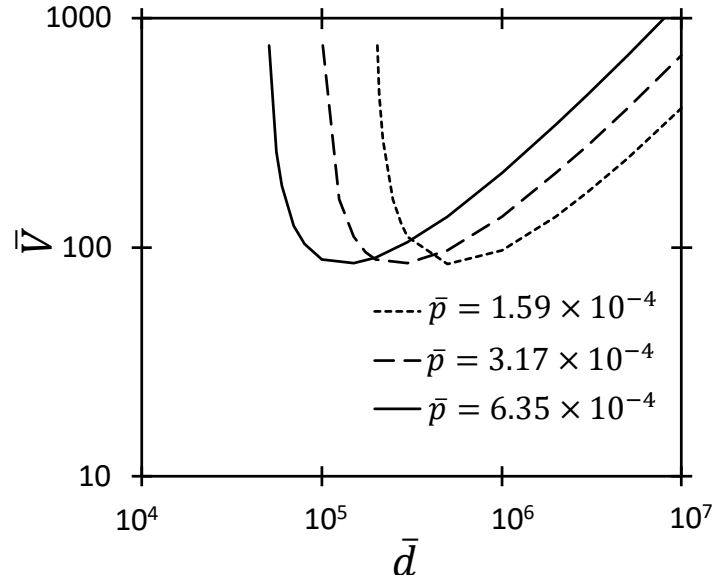


Figure 6.3. Dimensionless breakdown voltage, \bar{V} , as a function of dimensionless gap distance, \bar{d} , for various dimensionless pressures, \bar{p} , calculated with (6-14) for nitrogen considering $\gamma_{SE} = 10^{-3}$. Increasing \bar{p} shifts the minimum to the left.

Figure 6.4 demonstrates the transition from PL to FN-driven breakdown for microscale gaps. The exact microscale solution from (6-13) picks up this transition, while the analytic and limiting solutions detailed in (C54) and (C55), respectively, do not since they represent the asymptotic behavior of the FN-driven breakdown and would be strictly valid only when \bar{d} is much less than the transition value. Furthermore, (C55) directly indicates that $\bar{V} \propto \bar{d}$ in the field emission-driven breakdown regime, as noted in previous applications of this theory to experimental behavior (Meng et. al, 2018; Meng et. al, 2019; Loveless et. al, 2019). Additionally, Figure 6.4 shows that the transition from field emission-driven breakdown to PL may occur on either the left or right of the Paschen minimum depending on \bar{p} (Loveless et al., 2019). Electrode properties, particularly $\bar{\phi}$

and β , may also influence the intersection of these regimes with respect to the Paschen minimum (Meng et. al, 2018; Meng et. al, 2019; Loveless et. al, 2019).

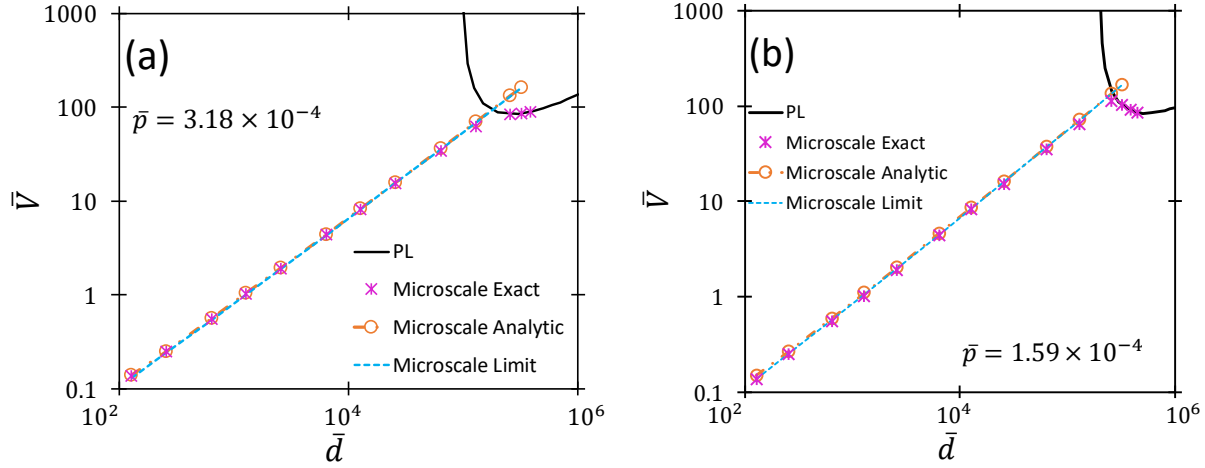


Figure 6.4. Dimensionless breakdown voltage, \bar{V} , as a function of dimensionless gap distance, \bar{d} , for dimensionless pressures of (a) $\bar{p} = 3.18 \times 10^{-4}$ and (b) $\bar{p} = 1.59 \times 10^{-4}$, using the exact (6-13), analytic (C54), and limiting equation (C55) for microscale and PL (6-14) with nitrogen considering $\gamma_{SE} = 10^{-3}$. The transition from microscale breakdown to the traditional PL can occur to either the left or the right of the Paschen minimum depending on one's pressure.

Further decreasing gap distance beyond the FN-driven breakdown regime leads to a purely electron emission regime characterized by FN, MG, and CSCL. Figure 5 shows the transition between these regimes at $\bar{d} = 129$ ($d = 10$ nm) for low and high $\bar{\mu}$, demonstrating the transition of the exact solution from FN at low \bar{V} to the MG regime at mid- \bar{V} , and, finally, to CSCL at high \bar{V} for a given $\bar{\mu}$ (Song et al., 2018). A lower $\bar{\mu}$ yields a lower \bar{J} since the electrons undergo more collisions. Since $\mu \propto 1/p$, (or, alternatively, mobility is inversely proportional to collisionality), this intuitively means that J will be lower for a given V at high p , yielding an MG-driven regime. Figure 6.5 shows that the exact solution for $\bar{\mu} = 1000$ never follows the MG equation for $\bar{\mu} = 1000$. Rather, there is a direct transition from FN to CSCL under these conditions. Thus, electron emission may transition to MG depending on the system pressure, or collisionality. Further investigation is

needed to accurately relate mobility and pressure, although current semi-empirical relationships represent promising first steps.

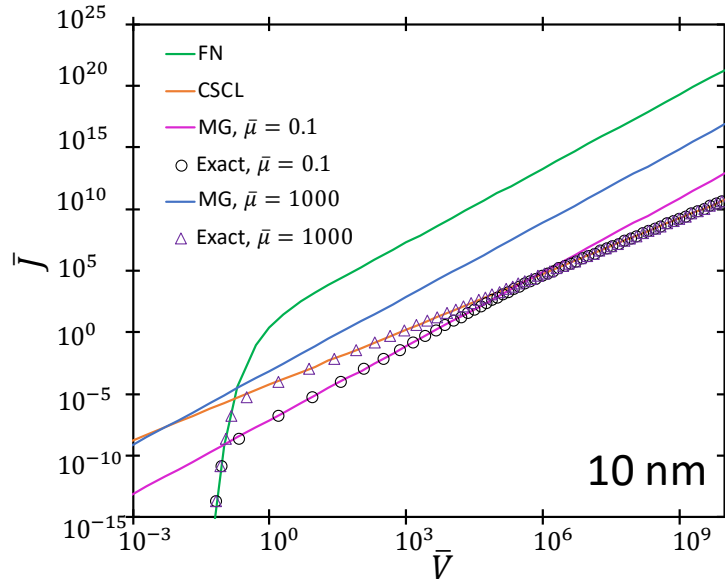


Figure 6.5. Dimensionless current density \bar{J} as a function of dimensionless breakdown voltage \bar{V} demonstrating the transitions of the exact solution between CSCL, FN, and MG, and showing the implications of increasing mobility on those transitions for a 10 nm gap.

Further reducing gap distances below ~ 100 nm requires additionally considering the implications of QSCL on emission. The dimensionless quantum equations in (6-9) give two solutions that yield a minimum and maximum solution for QSCL, as shown in Figure 6.6. Figure 6.6a shows the intersection of these solutions of (6-9) with CSCL. In particular, the solution of (6-9) ultimately follows the CSCL once \bar{V} is sufficiently large to overcome quantum effects (Lau, Chernin, Colombant, & Ho, 1991). Figure 6.6b shows the nexus between QSCL, CSCL, MG, and FN at a fixed $\bar{\mu} = 250$. This point represents a state of high sensitivity where small perturbations in experimental conditions may shift the system into any of these emission regimes.

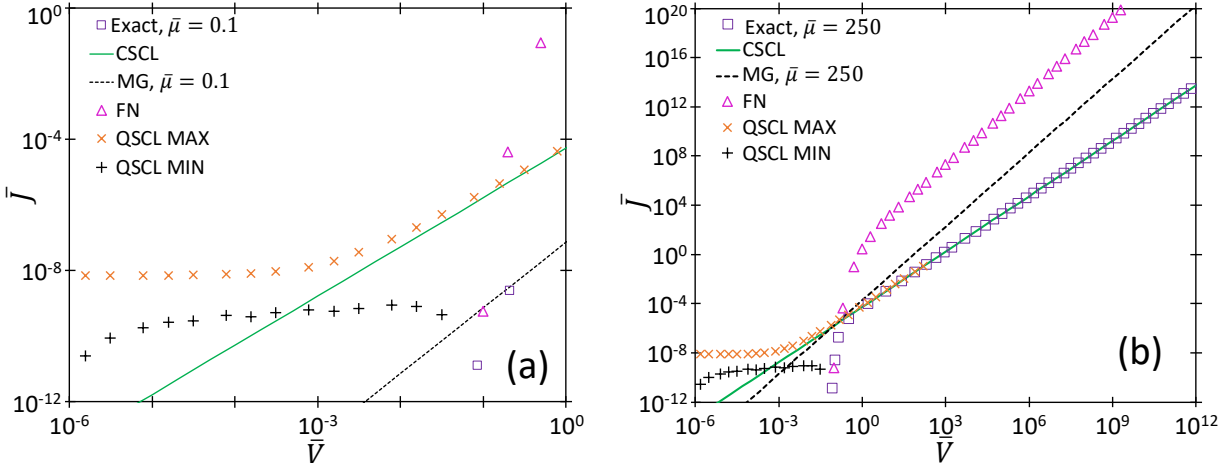


Figure 6.6. Dimensionless current density \bar{J} as a function of dimensionless breakdown voltage \bar{V} for a 10 nm gap demonstrating the transitions of the exact solution between QSCL, CSCL, FN, and MG focusing on (a) the transition from QSCL to CSCL and (b) the full spectrum of transitions.

Figure 6.7 shows state diagrams demonstrating the transitions between the asymptotic solutions of the various emission mechanisms at $\bar{\mu} = 1000, 500,$ and 50 to examine the relative importance of each mechanism. First, the curves representing the transitions QSCL to FN and CSCL to FN do not shift with changing $\bar{\mu}$ because they are independent of $\bar{\mu}$. At the highest $\bar{\mu}$, corresponding to the lowest pressure (closest to vacuum), the transition from QSCL to FN occurs to the left of the nexus between CSCL, MG, and FN (cf. Figure 6.7a). Reducing the mobility (or increasing p) to $\bar{\mu} = 500$ causes the transition from CSCL and MG to shift sufficiently to the left such that all four asymptotic solutions match at $\bar{d} \approx 10^3$ (cf. Figure 6.7b), giving a fourth order nexus between QSCL, CSCL, MG, and FN. At higher p , it may be possible to transition from FN to QSCL directly without transitioning through either of the standard space-charge limited emission regimes. It is also possible at sufficiently high \bar{V} to transition from FN to MG to CSCL without transitioning through the QSCL regime at even small \bar{d} . For a physical sense of the meaning of these nexuses, consider Figure 6.7b. The nexus between MG, FN, QSCL, and CSCL occurs at $\bar{d} \approx 1000$, and

$\bar{V} \approx 1.34$. In dimensional units, these parameters correspond to $d = 7.75 \times 10^{-9}$ m, $V = 8.5$ V, and $\mu = 6.45 \times 10^{-3}$ m²/(Vs). For nitrogen, considering $v_d = \mu E$ with $v_d = 3.3 \times 10^6 \sqrt{E/p}$ with E and v_d in cgs units and p in Torr (Zubarev & Ivanov, 2018) yields a pressure of 2910 Torr. While this is a large pressure, the same analysis for Figure 6.7a yields a triple point at gap distances of 271 nm and pressure of 755 Torr. While experiments have examined the transition in electron emission mechanisms at quantum scale (tens of nanometers) at vacuum (Bhattacharjee, Vartak, & Mukherjee, 2008; Bhattacharjee & Chowdhury, 2009), most atmospheric pressure experiments have focused on microscale dimensions and atmospheric pressure (Go & Venkatraman, 2014; Brayfield II et al., 2019; Meng et al. 2018; Meng et al., 2019; Loveless et al., 2019). We have recently assessed electron emission for submicroscale gaps at atmospheric pressure to begin experimentally characterizing this regime, which has practical implications for MEMS and NEMS devices at increasingly smaller sizes (Bogue, 2007; Craighead, 2000).

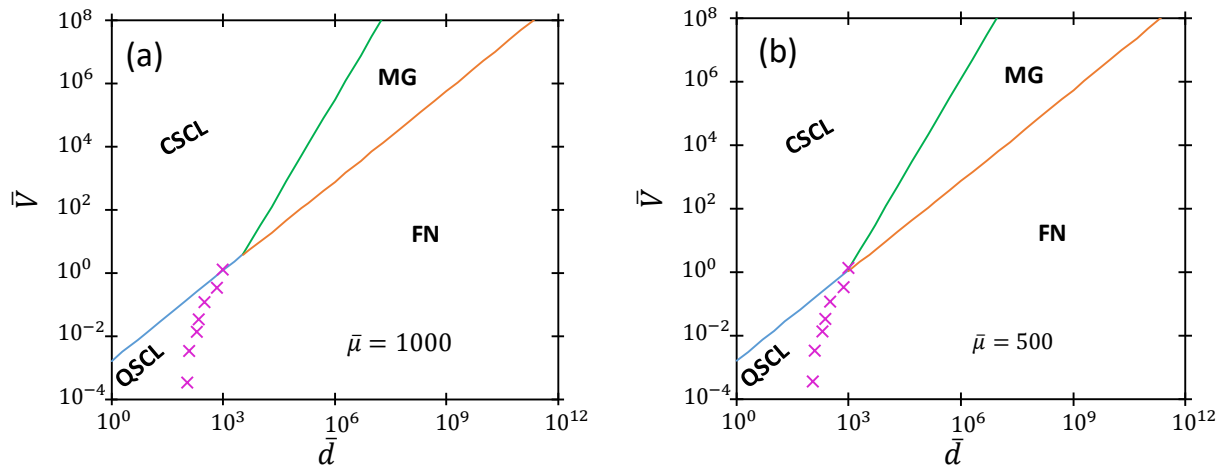


Figure 6.7. Dimensionless breakdown voltage, \bar{V} , as a function of dimensionless gap distance, \bar{d} , demonstrating the respective regions where each emission mechanism should dominate for dimensionless mobilities of (a) $\bar{\mu} = 1000$ and (b) $\bar{\mu} = 500$.

6.4 Conclusion

This work presents a unified, dimensionless model describing electron emission and gas breakdown from quantum scales to the traditional PL. While one material parameter remains in the dimensionless PL, the model is universal (true for any gas) from quantum scales up through FN-driven breakdown. Although several studies have examined the intersections between these mechanisms piecemeal in the past, they all used the most natural nondimensionalization schemes for the given conditions. The present study used a *single* scaling approach to derive a theory across the mechanisms with a single dimensionless reference frame to demonstrate various transitions between the mechanisms in a consistent manner. This permitted us to demonstrate that the triple point between MG, FN, and CSCL shifts to larger \bar{d} with increasing $\bar{\mu}$.

Furthermore, the common dimensionless framework allowed us to show the nexus between MG, FN, CSCL, and QSCL, suggesting experimental conditions where slight perturbations may lead to a transition between all four mechanisms at very small gaps. Prior experiments for nanoscale gaps at vacuum have demonstrated the transitions between QSCL and CSCL (Bhattacharjee, Vartak, & Mukherjee, 2008) and between FN and CSCL (Bhattacharjee & Chowdhury, 2009); however, the fourth order nexus suggests some very interesting design considerations, particularly for NEMS or the case of leakage for electron emitters at vacuum. Specifically, it points to the ease with which slight variations in gap distance can shift one into one of the space-charge limited emission regimes. Interestingly, Figure 6.7 shows that changing the mobility (or pressure) does not change the sensitivity to transitioning from FN to space-charge limited emission, but it does change the

relative sensitivity to transitioning from FN or MG to CSCL, with lower mobilities (higher pressures) shifting the transition to CSCL at smaller gaps.

This unified theory will provide a starting point for further theoretical development. One challenge with the microscale gas breakdown equation presently is the assumption of $E = V/d$ for application in Poisson's equation. First, most experiments are *not* in planar geometries and use either pin-to-plate or pin-to-pin geometries. Future work will derive closed form solutions for this to include the field enhancement due to the electrode geometry as done elsewhere numerically (Fu, Krek, Zhang, & Verboncoeur, 2018). Physically, this relationship between E and V fails as space charge builds up in the gap. We address this in our unification of FN and space-charge limited emission by coupling Poisson's equation and the electron force law in (3) and (4), respectively, in the present paper and in Refs. (Darr, Loveless, & Garner, 2019) and (Dynako, Darr, & Garner, 2019). Future work could quantify the impact of space charge on microscale gas breakdown more directly. Based on Refs. (Darr, Loveless, & Garner, 2019) and (Dynako, Darr, & Garner, 2019), which show that the nexus between FN, MG, and CSCL occurs at ~ 250 nm for nitrogen at atmospheric pressure, we anticipate that FN will dominate over space-charge limited emission at atmospheric pressure at microscale; however, this does not mean that no contribution exists, particularly as we approach submicroscale gaps where space charge begins to contribute more strongly to electron emission. The present work provides a potential framework for approaching this issue by coupling the electron force equation and continuity equation to modify the input to Poisson's equation as done in Refs. (Darr, Loveless, & Garner, 2019) and (Dynako, Darr, & Garner, 2019). The common nondimensionalization scheme presented here will permit a more detailed examination of this relationship and updating E across the gap (Venkatraman & Alexeenko, 2012; Loveless & Garner,

2017b; Loveless & Garner, 2016) to more directly couple microscale gas breakdown with space-charge limited emission. Molecular dynamics simulations of particles in the gap under various voltages, gap distances, and pressures (or collisionality) (Torfason, Valfells, & Manolescu, 2016) will provide further insight into the implications of space charge in this regime.

The common framework will help with better characterizing electrode characteristics, particularly field enhancement β and work function ϕ , which influence FN and FN-driven microscale gas breakdown, and secondary electron emission γ_{SE} , which influences microscale gas breakdown and PL. The common framework across mechanisms and a better characterization of the influence of diode geometry will permit minimizing the amount of fitting currently required to apply the theory to experimental data and help make the theory more useful *a priori*.

Finally, while the current theory provides a fairly comprehensive assessment of electron emission mechanisms, it is incomplete since it does not include thermionic or thermo-field emission (Zhang, Valfells, Ang, Luginsland, & Lau, 2017; Jensen, 2018; Jensen et al., 2019). Future theoretical work will incorporate temperature to examine the nexuses that arise between FN, CSCL, MG, Ohm's law, and thermionic emission. Such results will be useful since temperature increases may become important and introduce another component. This will guide future experiments assessing the impact of not only pressure, gap distance, and electrode design, but temperature and heating on electron emission and gas breakdown. Experimental work under these conditions will help develop more robust relations between pressure and mobility, which will further generalize the theory reported here.

7. SCALING LAWS FOR AC GAS BREAKDOWN AND IMPLICATIONS FOR UNIVERSALITY

Reprinted from Loveless, A. M. and Garner, A. L. (2017) Scaling laws for AC gas breakdown and implications for universality. *Physics of Plasmas*, 24, 104501, with the permission of AIP Publishing.

7.1 Introduction

Radiofrequency (RF) plasmas have advantages over direct current (DC) plasmas. For instance, since electron diffusion dictates RF breakdown rather than ion flow to the cathode (Smith, Charles, & Boswell, 2003), the importance of secondary electron emission and surface conditions decreases (Levko & Raja, 2015). This is important for accurately predicting breakdown due to the difficulty of determining secondary electron emission parameters a priori (Levko & Raja, 2015). Moreover, one may extend cathode lifetime by covering the electrodes with a dielectric material, since ion collisions with the cathode are not necessary to sustain an RF plasma (Levko & Raja, 2015). This has motivated studies of RF plasmas for numerous applications requiring extended electrode lifetimes, including microthrusters (Sitaraman & Raja, 2012).

Kihara mathematically modeled microwave, RF, and DC gas breakdown voltage (Kihara, 1952). Rather than using observed or quantum-mechanically calculated collision cross sections, he developed and incorporated a molecular model for the collision processes into the Boltzmann equation. Using this molecular model to define the diffusion coefficient and coupling it with the coefficient of collision ionization yielded the breakdown condition. Combining this breakdown condition with a relationship between electron temperature and electric field amplitude gave an equation for microwave breakdown as a function of frequency and wavelength. Incorporating the

periodic mass-motion of electrons caused by the electric field (shown through the drift velocity) yielded the RF breakdown condition. Finally, noting the dependence of DC breakdown on collisional processes, he incorporated a secondary electron mechanism to derive a breakdown equation analogous to Paschen's law (Kihara, 1952).

Other studies have computationally assessed alternating current (AC) breakdown voltage (Smith, Charles, & Boswell, 2003; Levko & Raja, 2015; Radmilović-Radjenović & Lee, 2005; Levko & Raja, 2016; Biswas & Mitra, 1979; Campbell et al., 2014). For example, Radmilović-Radjenović and Lee modeled RF breakdown using a particle-in-cell (PIC) code that focused on improving secondary emission model (Radmilović-Radjenović & Lee, 2005). Smith, et al. compared experimental and simulated breakdown voltage for argon discharges to a volume-averaged model at 13.56 MHz from 1-500 mTorr and gap distances from 2-20 cm. They demonstrated that secondary electron emission has a small effect on the right-hand-side of the Paschen curve, but significantly impacts the slope of the left-hand-side (Smith, Charles, & Boswell, 2003). PIC simulations assessing microwave discharges at atmospheric pressure considering both field electron emission and secondary electron emission (Levko & Raja, 2015) showed that microwave and DC breakdown voltages converged at gap distances below $\sim 5 \mu\text{m}$ (Levko & Raja, 2015). Additionally, Biswas and Mitra correlated Paschen's law with high-frequency breakdown by incorporating frequency into the electron mean free path (Biswas & Mitra, 1979). Scaling the gap distance to the electron mean free path and coupling with Paschen's law yielded breakdown voltage as a function of frequency. This model scaled with the product of frequency and gap distance, analogous to Paschen's law (Biswas & Mitra, 1979). Finally, Campbell et al. modeled microwave breakdown in nitrogen gas by treating it with a two-fluid model at the boundary of

different pressure regimes in a large gap (Campbell et al., 2014). They further showed that microwave breakdown in microgaps only occurs above a specific pressure (Campbell et al., 2014).

Section 7.2 details the nondimensionalization of Kihara's breakdown model (Kihara, 1952) and matched asymptotic analysis showing the transitions between the various regimes. Analytic results are compared to those determined both numerically and experimentally. Concluding remarks are made in Section 7.3. This work was published in Loveless and Garner (2017c).

7.2 Matched Asymptotic Analysis

While many studies have assessed RF and microwave breakdown, the current work provides simple, analytic equations to clearly show transition between high (microwave) frequency, RF, and DC. The present study provides a first step in developing a universal breakdown theory across frequency, which may suggest regimes requiring more detailed physical analysis. We begin with Kihara's (1952) equations for breakdown voltage for MW and RF fields given by

$$\frac{B_0 P}{E} \left[1 + \left(\frac{\delta C_1 L / \Lambda}{A_1 P L} \right)^2 \right]^{1/2} = 2 \ln(A_1 P L), \quad (7-1)$$

and

$$\exp\left(\frac{B_0 P}{2E}\right) = A_1 P L \left(1 - \frac{E / B_0 P}{\xi C_2 L / \Lambda} \right), \quad (7-2)$$

respectively, where P is gas pressure in torr, E is the breakdown field in V/cm, L is the gap distance in cm, $\Lambda = 2\pi c/\omega$ is the wavelength in cm, B_o is a gas constant, $A_1 = (N/P\pi)(3\sigma\lambda/c_i)^{1/2}$, $C_1 = (\omega\lambda/\pi)(3\sigma/\lambda c_i)^{1/2}$, $C_2 = (2\pi c/c_i^2)(\lambda/6\rho)^{1/2}$, ξ and δ are fitting constants, and σ , λ , c_i , and ρ are gas-dependent molecular constants tabulated in (Kihara, 1952) and summarized in Table 7-1. Fitting (7-1) and (7-2) to experimental results for hydrogen requires setting $\delta = 0.8$ and $\xi = 3.2$ (Kihara, 1952). Equation (7-1) was derived under the assumption that the wavelength is much greater than the gap distance to allow one-dimensional treatment and only considers gains from ionizing collisions and losses from diffusion (Kihara, 1952). The derivation of (7-2) additionally accounts from the periodic mass-motion of electrons induced by the field by considering the drift velocity of electrons in the balance equation (Kihara, 1952). We will nondimensionalize (7-1) and (7-2) to examine the behavior at critical limits (such as high or low pressure and frequency) and the transition from RF to microwave.

Table 7.1 Molecular constants summarized from (Kihara, 1952) for the gases considered in this work.

| Gas | c_i [10^8 cm/s] | σ [10^{-17} cm ²] | λ [10^{-8} cm ³ /s] | ρ [10^{-25} cm s] |
|----------|----------------------|---|---|---------------------------|
| Hydrogen | 1.89 | 5.90 | 5.50 | 8.10 |
| Argon | 1.89 | 17.4 | 7.80 | 13.5 |
| Nitrogen | 1.87 | 12.3 | 16.5 | 18.0 |
| Helium | 2.35 | 2.00 | 2.00 | 1.40 |

We first substitute A_1 and C_1 into (7-1) and nondimensionalize the resulting equation by defining $E = \bar{E}E_*$, $P = \bar{P}P_*$, $L = \bar{L}L_*$, and $\omega = \bar{\omega}\omega_*$, with $E_* = B_o P_*$, $P_* = 760$ torr, $L_* = (\pi/\chi P_*)(c_i/3\sigma\lambda)^{1/2}$, and $\omega_* = (c_i^2/\xi L_*)(6\rho/\lambda)^{1/2}$, where bars and stars denote dimensionless and scaling parameters, respectively. For simplicity, we assume a parallel plate geometry ($E = V/L$, where V is the applied voltage and $V = \bar{V}E_*L_*$). Table 7-2 summarizes the scaling parameters for

the gases considered here. Coupling these parameters with (7-1) yields a fully nondimensionalized analytic equation for MW-induced breakdown voltage as

$$\bar{V} = \frac{\bar{P}\bar{L}}{2 \ln(\bar{P}\bar{L})} \left[1 + \left(\frac{\theta \bar{\omega}}{\bar{P}} \right)^2 \right]^{1/2}, \quad (7-3)$$

where $\theta = (\delta c_i^2 / \xi \pi \lambda)(18 \sigma \rho / c_i)^{1/2}$ is a dimensionless, gas-dependent constant that varies from ~0.11 to ~0.69 for the gases considered here. Figure 7-1 shows \bar{V} as a function of \bar{P} for three different values of $\bar{\omega}$ for hydrogen, nitrogen, argon, and helium using (7-3).

As \bar{P} increases, \bar{V} depends less on $\bar{\omega}$ since $(\theta \bar{\omega} / \bar{P})^2 \approx 0$ for $\bar{P} \gg \bar{\omega}$ in (7-3), leading to

$$\bar{V} = \frac{\bar{P}\bar{L}}{2 \ln(\bar{P}\bar{L})}, \quad (7-4)$$

which is independent of both $\bar{\omega}$ and θ , making it universal (valid for all gases). Figure 7-1 demonstrates this behavior since the solutions for \bar{V} at different $\bar{\omega}$ converge as \bar{P} gets large. When $\bar{P} \ll \bar{\omega}$, $1 + (\theta \bar{\omega} / \bar{P})^2 \approx (\theta \bar{\omega} / \bar{P})^2$ and (7-3) becomes

$$\bar{V} = \frac{\theta \bar{\omega} \bar{L}}{2 \ln(\bar{P}\bar{L})}. \quad (7-5)$$

The dependence on θ at low \bar{P} indicates that \bar{V} depends on gas at low pressure, as also shown in Figure 7-1.

Table 7.2 Summary of scaling parameters for the gases considered here.

| Gas | E_* [10^4 V/cm] | L_* [10^{-4} cm] | ω_* [10^{11} s $^{-1}$] |
|----------|----------------------|-----------------------|------------------------------------|
| Hydrogen | 9.88 | 5.13 | 6.54 |
| Argon | 15.2 | 2.51 | 14.5 |
| Nitrogen | 25.8 | 2.04 | 13.9 |
| Helium | 3.80 | 16.3 | 2.20 |

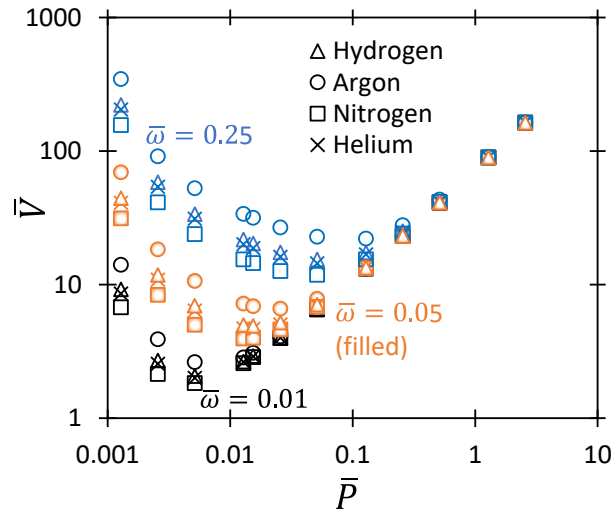


Figure 7.1 Comparison of dimensionless breakdown voltage, \bar{V} , from (7-3) as a function of dimensionless pressure, \bar{P} , at a dimensionless gap distance of $\bar{L} = 1000$ for different values of dimensionless angular frequency, $\bar{\omega}$, for hydrogen, nitrogen, argon, and helium. At large \bar{P} , \bar{V} becomes independent of gas, or universal.

Figure 7-2 shows the exact solution for MW breakdown given by (7-3), the matched asymptotic solution given by (7-4) and (7-5), and experimental results for hydrogen (Lisovskiĭ, 1999). As \bar{P} increases for a given $\bar{\omega}$, (7-4) agrees well with (7-3) and (7-5) deviates. Conversely, at small \bar{P} , (7-5) agrees well with (7-3) and (7-4) deviates. While (Lisovskiĭ, 1999) considers cylindrical geometries, the large radius of the cylindrical electrodes effectively yields a parallel plate geometry.

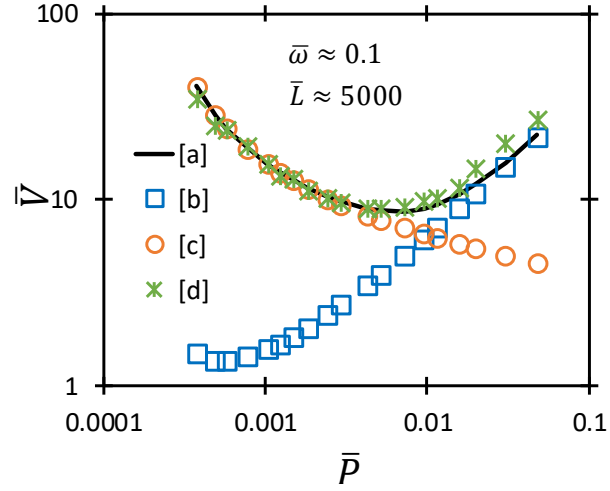


Figure 7.2 Comparison of dimensionless breakdown voltage, \bar{V} , as a function of dimensionless pressure, \bar{P} , for various values of $\bar{\omega} \approx 0.1$ and $\bar{L} \approx 5000$ for hydrogen, from [a] the exact, dimensionless equation for MW breakdown given by (7-3), [b] the $\bar{P} \gg \bar{\omega}$ limit given by (7-4), [c] the $\bar{P} \ll \bar{\omega}$ limit given by (7-5), and [d] experimental data (Lisovskiĭ, 1999).

For RF breakdown, we substitute the definitions for A_1 , C_2 , and the dimensionless and scaling parameters defined above into (7-2) to obtain a universal RF breakdown equation given by

$$\exp\left(\frac{\bar{P}}{2\bar{E}}\right) = \bar{P}\bar{L} \left[1 - \frac{\bar{E}}{\bar{P}\bar{\omega}\bar{L}}\right]. \quad (7-6)$$

Taking the natural log of both sides, and noting from numerical results that $\bar{E}/(\bar{P}\bar{\omega}\bar{L}) \ll 1$ yields

$$\bar{V} = \frac{\bar{P}\bar{\omega}\bar{L}^2 \ln(\bar{P}\bar{L})}{2} \left\{ 1 \pm \sqrt{1 - \frac{2\bar{\omega}^{-1}\bar{L}^{-1}}{(\ln[(\bar{P}\bar{L})]^2)}} \right\}. \quad (7-7)$$

Since $\bar{\omega}\bar{L}$ and $\ln[(\bar{P}\bar{L})]^2$ are both greater than one, it stands to reason that $2/\{\bar{\omega}\bar{L} \ln[(\bar{P}\bar{L})]^2\} \ll 1$, allowing us to use binomial theorem to expand the radical in (7-7) to obtain the RF limits for dimensionless breakdown voltage to the left and right of the minimum as

$$\bar{V} = \bar{\omega}\bar{L}^2\bar{P} \ln(\bar{P}\bar{L}) - \frac{\bar{P}\bar{L}}{2 \ln(\bar{P}\bar{L})}, \quad (7-8)$$

and

$$\bar{V} = \frac{\bar{P}\bar{L}}{2 \ln(\bar{P}\bar{L})}, \quad (7-9)$$

respectively. However, (7-8) and (7-9) poorly approximate the minimum since $\bar{P}\bar{L} \approx 1$ at that point, invalidating $2\bar{\omega}^{-1}\bar{L}^{-1}/\ln[(\bar{P}\bar{L})]^2 \ll 1$. Interestingly, (7-9) is the same as the $\bar{P} \gg \bar{\omega}$ limit for MW breakdown from (7-4), demonstrating that both models predict the same limiting behavior for high pressure independent of frequency and gas. Figure 7-3 shows the results from the numerical solution of (7-6), the analytic equations in (7-7), the limiting equations shown in (7-8) and (7-9), and experimental data (Lisovskiy et al., 2006). For both gap distances considered, (7-8) accurately predicts most of the left-hand side of the minimum while (7-7) and (7-9) accurately predict the behavior to the right of the minimum. For both cases, the experimental data kinks where \bar{P} begins to decrease with increasing \bar{V} that modeling does not predict. Other theoretical analyses also fail to capture this kink (Lisovskiy & Yegorenkov, 1998) although PIC simulations using an improved second emission do (Radmilović-Radjenović & Lee, 2005). Future experiments and simulations with hydrogen and other gases may demonstrate both the reproducibility of this behavior and the potential physical mechanisms involved.

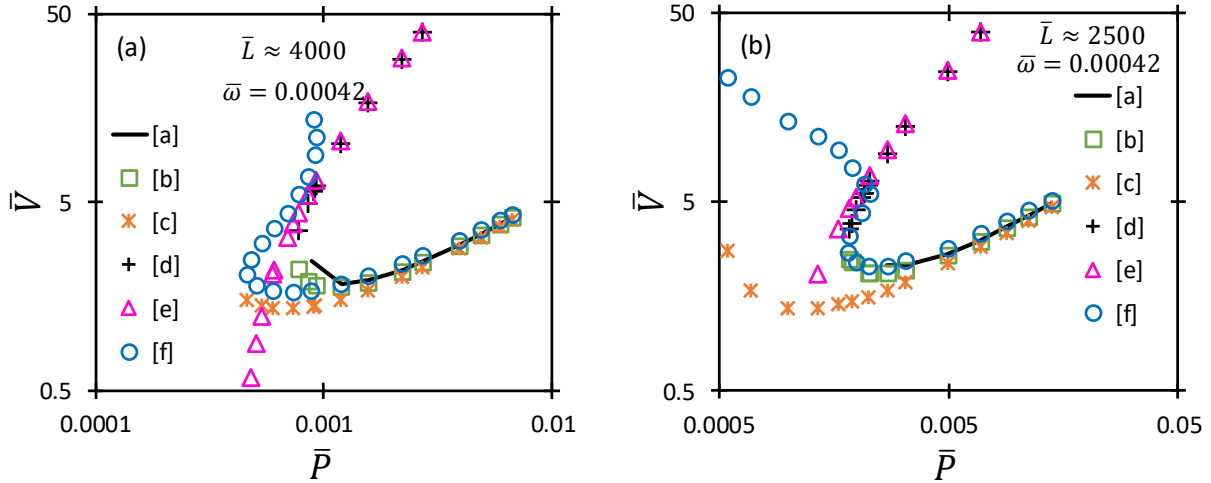


Figure 7.3 Comparison of RF-induced dimensionless breakdown voltage, \bar{V} , as a function of dimensionless pressure, \bar{P} , for $\bar{\omega} = 4.2 \times 10^{-4}$ and $\bar{L} \approx$ (a) 4000 and (b) 2500 for hydrogen, from [a] the numerical solution of (7-6), [b] the analytic solution valid to the right of the minimum given by the negative root of (7-7), [c] the limit valid to the right of the minimum given by (7-9), [d] the analytic solution valid to the left of the minimum given by the positive root of (7-7), [e] the limit valid to the left of the minimum given by (7-8), and [f] experimental data from (Lisovskiy et al., 2006)

Figure 7-4 shows the transition of dimensionless breakdown voltage from RF to MW as $\bar{\omega}$ increases for a fixed \bar{P} and \bar{L} for hydrogen. At low $\bar{\omega}$, the RF numerical equation given by (7-6) should be the most accurate, with the RF analytic equation in (7-7) giving similarly accurate results. As $\bar{\omega}$ increases, the MW $\bar{\omega} \ll \bar{P}$ limit shown in (7-4)—and the RF limit shown in (7-8)—agree well with the numerical RF equation. Finally, when $\bar{\omega} > \bar{P}$, there is a transition from RF to MW, and the MW equation given by (7-3) and the corresponding MW limit for $\bar{\omega} \gg \bar{P}$ shown in (7-5) offer the most accurate results. Since the transition occurs at $\bar{\omega} > \bar{P}$, the frequency corresponding to this transition increases at higher pressures.

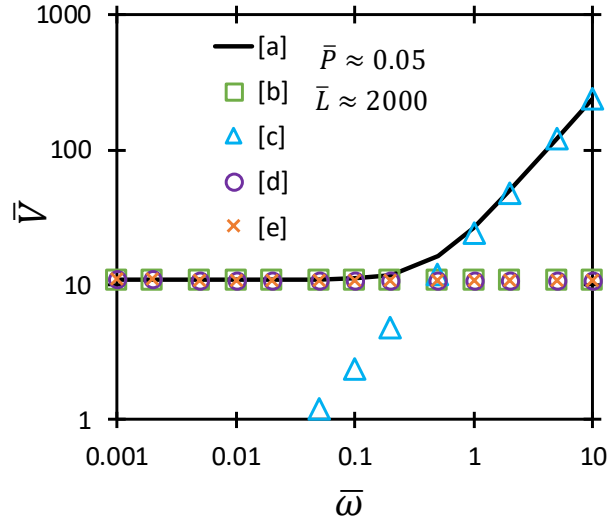


Figure 7.4 Transition from RF to MW dimensionless breakdown voltage, \bar{V} , in hydrogen as a function of dimensionless angular frequency, $\bar{\omega}$, at a gap distance of 1 cm determined using [a] the full MW equation from (7-3), [b] the $\bar{P} \gg \bar{\omega}$ limit given by (7-4), [c] the $\bar{P} \ll \bar{\omega}$ limit given by (7-5), [d] the numerical solution of the RF equation from (7-6), and [e] the analytic RF solution of (7-7).

Finally, we address DC gas breakdown, governed by Paschen's law, which is given by (Kihara, 1952; Paschen, 1889)

$$V = \frac{B_o PL}{\ln(A_o PL) - \ln[\ln(1 + \gamma^{-1})]}, \quad (7-10)$$

where $A_o = (\chi\sigma/c_i)(3\lambda/\rho)^{1/2}$, $B_o = (\chi mc_i^2/2e)(3\lambda\rho)^{1/2}$, γ is the secondary electron emission coefficients, and σ, c_i, λ , and ρ are the gas-dependent molecular constants (Kihara, 1952). Substituting the dimensionless variables and scaling parameters defined previously into (7-10) yields a dimensionless form of Paschen's law, given by

$$\bar{V} = \frac{\bar{P}\bar{L}}{\ln[\Omega\bar{P}\bar{L}]}, \quad (7-11)$$

where $\Omega = (\pi^2\sigma/\rho c_i)^{1/2}/\ln(1 + \gamma^{-1})$, with typical values of Ω ranging from $\sim 2/\ln(1 + \gamma^{-1})$ to $\sim 3/\ln(1 + \gamma^{-1})$. Increasing pressure reduces the dependence on γ since $\ln[\Omega\bar{P}\bar{L}] = \ln[\Omega] + \ln[\bar{P}\bar{L}] \approx \ln[\bar{P}\bar{L}]$ for large \bar{P} . Thus, (7-11) reduces to

$$\bar{V} \approx \frac{\bar{P}\bar{L}}{\ln[\bar{P}\bar{L}]}, \quad (7-12)$$

which, interestingly, is the same form as the RF and MW limits given by (7-9) and (7-4), respectively, although this limit is larger by a factor of two. Figure 5 shows the results of (7-3), (7-6), (7-11) and demonstrates the similar limiting behavior as \bar{P} increases, shown by the ratio of the RF (and MW, since they have the same limiting equation) and the Paschen results approaching two since $\bar{P}\bar{L}$ dominates in (7-11) for larger \bar{P} , resulting in (7-12).

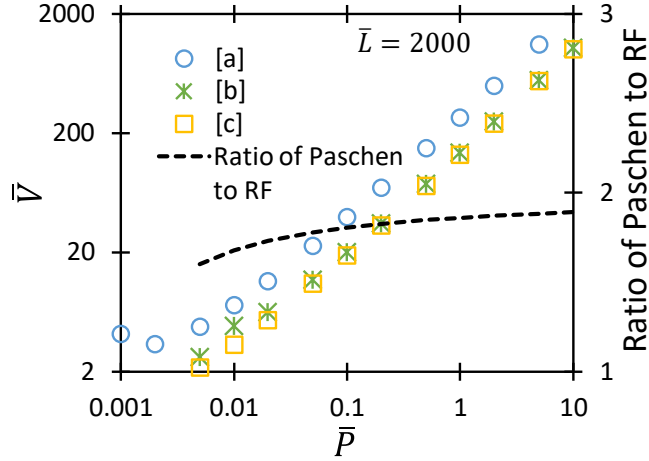


Figure 7.5 Dimensionless breakdown voltage, \bar{V} , as a function of dimensionless pressure, \bar{P} , for hydrogen for $\bar{L} = 2000$ from [a] Paschen's law given by (7-11) assuming $\gamma = 0.1$, [b] the numerical solution of (7-6) assuming $\bar{\omega} = 0.0002$, and [c] the solution of (7-3) considering $\bar{\omega} = 0.002$. Additionally, the ratio of the results from Paschen's law from [a] and the numerical results from [b] are plotted on the secondary vertical axis.

7.3 Conclusion

In summary, this work derived simple, dimensionless, analytic equations for RF, MW, and DC breakdown. We showed that each regime predicted $\bar{V} \propto \bar{P}\bar{L}/\ln(\bar{P}\bar{L})$ as $\bar{P} \rightarrow \infty$ independent of gas and frequency. We further demonstrated the transition from RF to MW regimes at $\bar{\omega} \gg \bar{P}$ and MW to RF for $\bar{\omega} \ll \bar{P}$. Future work will aim to incorporate more accurate molecular constants to prevent the need for a fitting factor and more accurately account for electron emission. Decreasing gap size to microscale necessitates incorporating field emission into AC breakdown models (Lee et al., 2016; Lee et al., 2017b; Lee et al., 2017b). Analytic simplifications, as done for DC (Loveless & Garner, 2016; Loveless & Garner, 2017b), could ultimately elucidate multifrequency multiscale behavior. Conversely, large gaps require using Monte Carlo simulations to determine transport parameters and ultimately applying a drift-diffusion model to simulate breakdown to minimize computational expense (Nguyen, 2017). Furthermore, many potential applications

(defense and security, for example) require higher millimeter-wave and terahertz (Booske et al., 2008; Booske et al., 2011; Cook, Shapiro, & Temkin, 2010; Hidaka et al., 2009; Cook et al., 2011), which would require further assessment of higher frequencies in the AC models derived here. Broadly speaking, acquiring experimental data across the full range of parameters using a single setup is vital for deriving theoretical models, developing and benchmarking simulations, and elucidating the physics across various length scales, frequencies, and pressures. The current work provides a first step in understanding the fundamental physics and transitions between DC, RF, and MW breakdown and may be extended to address a wider parameter range.

8. CONCLUSION

This dissertation provided a continuation to a previous thesis (Loveless, 2017) detailing gas breakdown from microscale to the classical Paschen law by extending the model to incorporate additional electron emission phenomena and applying the model to experimental results. The initial dimensionless model provided a universal theory for gas breakdown using a matched asymptotic analysis to result in analytic breakdown equations (Venkattraman & Alexeenko, 2012; Loveless & Garner, 2017b) coupling field emission with the Townsend avalanche criterion by incorporating an increase in the electric field due to the presence of positive space charge, as detailed in Chapters 1 and 2.

Chapter 3 used in situ optical imaging to demonstrate the transition from field emission driven breakdown to Townsend avalanche driven breakdown. These transitions were noted in microscale gaps both experimentally using pulsed voltages and analytically through a simplified breakdown model (Meng et al., 2018). Of particular note was the roughly linear dependence of the dimensionless breakdown voltage on the dimensionless gap distance in the field emission driven regime. The ability to apply DC breakdown theory to pulsed voltage experiments demonstrates mechanism similarity in both breakdown regions.

Chapter 4 discussed the transition to Paschen's law for microscale gas breakdown at subatmospheric pressure (Loveless et al., 2019). This transition was demonstrated by applying a gas breakdown theory (Loveless & Garner, 2017b; Meng et al., 2018) to experimental data obtained at various pressures. With the field enhancement factor as a fitting parameter, the difference between the simple analytic solution and the experimental data was 3.71% on average.

Additionally, this analysis demonstrated that the intersection between the coupled field emission/Townsend avalanche model with the traditional Paschen law could occur either to the left or the right of the traditional Paschen law minimum by varying the work function.

Furthering the work function consideration, Chapter 5 presented a study on the impact of cathode surface roughness and multiple breakdown events on microscale gas breakdown at atmospheric pressure (Brayfield et al., 2019). Experimental data demonstrated the dependence breakdown voltage on multiple breakdown events for a pin-to-plate geometry with various degrees of cathode surface roughness. The theoretical analysis considered an effective gap distance for the multiple breakdown events, adding the set gap distance to the crater depth. With this consideration, the transition from the coupled field emission/Townsend regime to the traditional Paschen law occurred at similar gap distances to the single breakdown cases (Loveless & Garner, 2017b; Meng et al., 2018). Furthermore, the analysis demonstrated a linearly increasing field enhancement factor while field emission drove breakdown, and a roughly constant field enhancement factor in the Townsend avalanche driven regime.

Chapter 6 further extended the model presented in Chapter 2 by incorporating additional emission mechanisms into the model, including quantum-enhanced space charge limited behavior, classical space-charge limited behavior, and the Mott-Gurney law. We defined a common set of scaling parameters across the range of dominant mechanisms to derive a single unified theory that yields asymptotic solutions for quantum space-charge-limited emission (QSCL), the Child-Langmuir law (CL), space-charge-limited emission with collisions (MG), field emission (FE), field emission driven gas breakdown (FEGB), and classical gas breakdown defined by Paschen's law (PL).

The numerical and analytic models presented through Chapter 6 assumed a parallel plate geometry. However, many experimental designs do not use parallel plate electrodes, but rather pin-to-plate (Brayfield et al., 2019) or pin-to-pin (Meng et al., 2018; Loveless et al., 2019) electrodes.

A final extension of the theoretical work performed in this dissertation is for AC gas breakdown. Chapter 7 discusses a simple analytic model for RF, MW, and DC gas breakdown derived based on previous work (Kihara, 1952; Loveless & Garner, 2017). This simple model demonstrated analytic equations for limits of large and small frequency as related to pressure, showing similar scaling in breakdown voltage for each regime.

In summary, this dissertation provides numerical and analytic models describing gas breakdown from microscale to nanoscale at various pressures, and for macroscale at varying frequency. Future work will account for more specific physics. For instance, Darr et al. (2020) recently unified thermionic emission with space-charge-limited emission and field emission. Such an approach could be combined with the studies in this dissertation to provide a more complete multiphysics examination of breakdown and emission. For instance, analogous to this study, we could replace the Fowler-Nordheim equation for field emission with the thermo-field emission model (Jensen 2018; Jensen et al. 2019) to derive analytic equations that include temperature effects, which could become especially relevant for thermionic emitters. Ongoing work in this research group is applying particle-in-cell simulations to better characterize ionization coefficient at nano- and microscale and performing nanoscale breakdown and emission experiments at atmospheric pressure and vacuum (Brayfield, 2020). The theories presented here may be adapted by replacing

the semi-empirical relationship for ionization coefficient with one obtained using simulations over the range of relevant parameters. The models may also be adapted to account for the geometry of the nanoscale experiments (Lin et al. 2017) to characterize breakdown. Future work will extend these experiments to include temperature, which can then be further assessed by extending the theory, as outlined above. Better understanding of this behavior may be important for applications in directed energy and propulsion.

APPENDIX A. DETAILED MATCHED ASYMPTOTIC ANALYSIS OF BREAKDOWN VOLTAGE

In this Appendix, we derive analytic solutions for dimensionless breakdown voltage, \bar{V} , for $\bar{\alpha}\bar{d} \ll 1$ and $\bar{\alpha}\bar{d} \gg 1$, given by (2-7)-(2-10).

To obtain an analytic solution for \bar{V} , we start with the numerical equation, given by

$$\frac{\exp(\bar{\phi}^{3/2}/\beta\bar{E})}{\beta\bar{\phi}^{1/2}\exp(\bar{\phi}^{-1/2})}\sqrt{\frac{\bar{\tau}\bar{E}}{\bar{p}\bar{d}^2}}\frac{\{1-\gamma_{SE}[\exp(\bar{\alpha}\bar{d})-1]\}}{[\exp(\bar{\alpha}\bar{d})-1]}=\frac{\exp(x_0)(1+2\bar{E}x_0)}{x_0}. \quad (\text{A1})$$

Taking the natural log of both sides yields

$$\begin{aligned} \frac{\bar{\phi}^{3/2}}{\beta\bar{E}} - \ln[\beta\bar{\phi}^{1/2}\exp(\bar{\phi}^{-1/2})] + \frac{1}{2}\ln\left[\frac{\bar{\tau}}{\bar{p}\bar{d}^2}\right] + \frac{1}{2}\ln(\bar{E}) + \ln\{1-\gamma_{SE}[\exp(\bar{\alpha}\bar{d})-1]\} \\ - \ln[\exp(\bar{\alpha}\bar{d})-1] = x_0 + \ln(1+2\bar{E}x_0) - \ln(x_0). \end{aligned} \quad (\text{A2})$$

Since $\bar{E} \ll 1$, $x_0 \approx 1$, and $x_0 + \ln(1+2\bar{E}x_0) - \ln(x_0) = 1 + \ln(1+2\bar{E}) \approx 1 + 2\bar{E}$, we can further simplify the right-hand side of (A2) to obtain

$$\begin{aligned} \frac{\bar{\phi}^{3/2}}{\beta\bar{E}} - \ln[\beta\bar{\phi}^{1/2}\exp(\bar{\phi}^{-1/2})] + \frac{1}{2}\ln\left[\frac{\bar{\tau}}{\bar{p}\bar{d}^2}\right] + \frac{1}{2}\ln(\bar{E}) + \ln\{1-\gamma_{SE}[\exp(\bar{\alpha}\bar{d})-1]\} \\ - \ln[\exp(\bar{\alpha}\bar{d})-1] = 1 + 2\bar{E}. \end{aligned} \quad (\text{A3})$$

Deriving an analytic solution requires simplifying $\ln[\bar{E}^{1/2}]$, $\ln\{1 - \gamma_{SE}[\exp(\bar{\alpha}\bar{d}) - 1]\}$, and $\ln\{\exp[\bar{\alpha}\bar{d}] - 1\}$ so that (A3) does not result in a transcendental function in terms of \bar{E} . For $\ln[\bar{E}^{1/2}]$, we can simplify the natural log with

$$\ln[\bar{E}^{1/2}] = \frac{1}{2} [\ln(\Lambda\bar{E}) - \ln(\Lambda)] \approx \frac{1}{2} [\Lambda\bar{E} - 1 - \ln(\Lambda)] \quad (\text{A4})$$

provided we select Λ such that $\Lambda\bar{E} \approx 1$. We set $\Lambda = \Lambda_1 = 4 \times 10^4$ for $\bar{\alpha}\bar{d} \ll 1$, and $\Lambda = \Lambda_2 = 1 \times 10^5$ for $\bar{\alpha}\bar{d} \gg 1$.

We next consider $\ln\{1 - \gamma_{SE}[\exp(\bar{\alpha}\bar{d}) - 1]\}$, which depends on whether $\bar{\alpha}\bar{d} \ll 1$ or $\bar{\alpha}\bar{d} \gg 1$. Considering $\bar{\alpha}\bar{d} \ll 1$ (which also means that $\bar{p}/\bar{E} \ll 1$) yields

$$\begin{aligned} \ln\{1 - \gamma_{SE}[\exp(\bar{\alpha}\bar{d}) - 1]\} &= \ln\{1 - \gamma_{SE}[1 + \bar{\alpha}\bar{d} - 1]\} = \ln[1 - \gamma_{SE}\bar{\alpha}\bar{d}] \approx -\gamma_{SE}\bar{\alpha}\bar{d} \\ &= -\gamma_{SE} \left[\frac{\bar{p}\bar{d}}{\exp(\bar{p}/\bar{E})} \right] = -\gamma_{SE} \left[\frac{\bar{p}\bar{d}}{1 + \bar{p}/\bar{E}} \right] = -\gamma_{SE}\bar{p}\bar{d}[1 - \bar{p}/\bar{E}] \\ &= \frac{\gamma_{SE}\bar{p}^2\bar{d}}{\bar{E}} - \gamma_{SE}\bar{p}\bar{d}. \end{aligned} \quad (\text{A5})$$

Considering $\bar{\alpha}\bar{d} \gg 1$ (which makes $\bar{p}/\bar{E} \approx 1$) gives

$$\ln\{1 - \gamma_{SE}[\exp(\bar{\alpha}\bar{d}) - 1]\} = \ln\{1 - \gamma_{SE} \exp(\bar{\alpha}\bar{d})\} = \ln \left\{ 1 - \gamma_{SE} \exp \left(\frac{\bar{p}\bar{d}}{\exp[1]} \right) \right\}. \quad (\text{A6})$$

The final term we must simplify is $\ln[\exp(\bar{\alpha}\bar{d}) - 1]$. For $\bar{\alpha}\bar{d} \ll 1$, we obtain

$$\ln\{\exp[\bar{\alpha}\bar{d}] - 1\} = \ln\{1 + \bar{\alpha}\bar{d} - 1\} = \ln(\bar{\alpha}\bar{d}) = \ln\left[\frac{\bar{p}\bar{d}}{\exp(\bar{p}/\bar{E})}\right] = \ln(\bar{p}\bar{d}) - \frac{\bar{p}}{\bar{E}}, \quad (\text{A7})$$

and for $\bar{\alpha}\bar{d} \gg 1$ we obtain

$$\ln\{\exp[\bar{\alpha}\bar{d}] - 1\} = \ln\left\{\exp\left[\frac{\bar{p}\bar{d}}{\exp(1)}\right] - 1\right\} \quad (\text{A8})$$

Thus, if $\bar{\alpha}\bar{d} \ll 1$, we can use (A4), (A5), and (A7) to rewrite (A3) as

$$\begin{aligned} \frac{\bar{\phi}^{3/2}}{\beta\bar{E}} + \frac{1}{2}\ln\left(\frac{\bar{\tau}}{\bar{p}\bar{d}^2}\right) + \left[\frac{\Lambda_1\bar{E}}{2} - \frac{1}{2} - \frac{\ln(\Lambda_1)}{2}\right] - \ln(\beta\bar{\phi}^{1/2}) - \bar{\phi}^{-1/2} - \gamma_{SE}\bar{p}\bar{d} + \frac{\gamma_{SE}\bar{p}^2\bar{d}}{\bar{E}} \\ - \left[\ln(\bar{p}\bar{d}) - \frac{\bar{p}}{\bar{E}}\right] = 1 + 2\bar{E}. \end{aligned} \quad (\text{A9})$$

Multiplying both sides by \bar{E} , and moving everything to the left-hand side gives

$$\begin{aligned}
& \frac{\bar{\phi}^{3/2}}{\beta} + \gamma_{SE} \bar{p}^2 \bar{d} + \bar{p} \\
& + \left\{ \frac{1}{2} \ln \left(\frac{\bar{\tau}}{\bar{p} \bar{d}^2} \right) - \frac{1}{2} - \frac{\ln(\Lambda_1)}{2} - \ln(\beta \bar{\phi}^{1/2}) - \bar{\phi}^{-1/2} - \gamma_{SE} \bar{p} \bar{d} - \ln(\bar{p} \bar{d}) \right. \\
& \left. - 1 \right\} \bar{E} + \left[\frac{\Lambda_1}{2} - 2 \right] \bar{E}^2 = 0. \tag{A10}
\end{aligned}$$

Finally, by defining

$$\Delta_1 = \left\{ \ln(\bar{\tau}/\bar{p} \bar{d}^2)/2 - 3/2 - \ln(\Lambda_1)/2 - \ln(\beta \bar{\phi}^{1/2}) - \bar{\phi}^{-1/2} - \gamma_{SE} \bar{p} \bar{d} - \ln(\bar{p} \bar{d}) \right\}, \tag{A11}$$

we can solve (A10) for \bar{E} and apply $\bar{V} = \bar{E} \bar{d}$ to obtain

$$\bar{V} = \bar{d} \left[\frac{-\Delta_1 - \sqrt{\Delta_1^2 - 2\Lambda_1(\bar{\phi}^{3/2}/\beta + \gamma_{SE} \bar{p}^2 \bar{d} + \bar{p})}}{\Lambda_1} \right]. \tag{A12}$$

Similarly, if $\bar{a} \bar{d} \gg 1$, we can use (A6) and (A8) to rewrite (A3) as

$$\begin{aligned}
& \frac{\bar{\phi}^{3/2}}{\beta \bar{E}} + \frac{1}{2} \ln \left(\frac{\bar{\tau}}{\bar{p} \bar{d}^2} \right) + \left[\frac{\Lambda_2 \bar{E}}{2} - \frac{1}{2} - \frac{\ln(\Lambda_2)}{2} \right] - \ln(\beta \bar{\phi}^{1/2}) - \bar{\phi}^{-1/2} \\
& + \ln \left\{ 1 - \gamma_{SE} \exp \left[\frac{\bar{p} \bar{d}}{\exp(1)} \right] \right\} - \ln \left[\exp \left(\frac{\bar{p} \bar{d}}{\exp(1)} \right) - 1 \right] = 1 + 2\bar{E}. \tag{A13}
\end{aligned}$$

Multiplying by \bar{E} and moving everything to the left-hand side gives

$$\begin{aligned}
& \frac{\bar{\phi}^{3/2}}{\beta} + \left\{ \frac{1}{2} \ln \left(\frac{\bar{\tau}}{\bar{p}\bar{d}^2} \right) - \frac{3}{2} - \frac{\ln(\Lambda_2)}{2} - \ln(\beta\bar{\phi}^{1/2}) - \bar{\phi}^{-1/2} \right. \\
& \quad \left. + \ln \left\{ 1 - \gamma_{SE} \exp \left[\frac{\bar{p}\bar{d}}{\exp(1)} \right] \right\} - \ln \left[\exp \left(\frac{\bar{p}\bar{d}}{\exp(1)} \right) - 1 \right] \right\} \bar{E} \\
& \quad + \left(\frac{\Lambda_2}{2} - 2 \right) \bar{E}^2 = 0.
\end{aligned} \tag{A14}$$

Defining

$$\begin{aligned}
\Delta_2 = & \left\{ \ln(\bar{\tau}/\bar{p}\bar{d}^2)/2 - 3/2 - \ln(\Lambda_2)/2 - \ln(\beta\bar{\phi}^{1/2}) - \bar{\phi}^{-1/2} \right. \\
& \left. + \ln\{1 - \gamma_{SE} \exp[\bar{p}\bar{d}/\exp(1)]\} - \ln[\exp[\bar{p}\bar{d}/\exp(1)] - 1] \right\}
\end{aligned} \tag{A15}$$

allows us to solve (A14) to obtain

$$\bar{V} = \bar{d} \left[\frac{-\Delta_2 - \sqrt{\Delta_2^2 - 2\Lambda_2 \bar{\phi}^{3/2}/\beta}}{\Lambda_2} \right]. \tag{A16}$$

APPENDIX B. DERIVATION OF THE MODIFIED PASCHEN MINIMUM

This Appendix details the derivation of our analytic solution for the modified Paschen minimum. Deriving an analytic solution for \bar{p}_c requires taking the derivative of (2-7) with respect to \bar{p} , and setting it equal to zero. Since the resulting equation equals zero, we can just consider the numerator and write

$$\bar{d}\gamma_{SE} + \frac{3}{2\bar{p}} + \frac{\Lambda_1(1 + \gamma_{SE}\bar{d}^2) + \Delta_1[\gamma_{SE}\bar{d} + 3/2\bar{p}]}{\sqrt{\Delta_1^2 - 2\Lambda_1(\bar{\phi}^{3/2}/\beta + \gamma_{SE}\bar{p}\bar{d}^2 + \bar{p})}} = 0, \quad (\text{B1})$$

where $\Delta_1 = \{\ln(\bar{\tau}/\bar{p}\bar{d}^2)/2 - 3/2 - \ln(\Lambda_1)/2 - \ln(\beta\bar{\phi}^{1/2}) - \bar{\phi}^{-1/2} - \gamma_{SE}\bar{p}\bar{d} - \ln(\bar{p}\bar{d})\}$ and $\Lambda_1 = 4 \times 10^4$. Noting that $\Delta_1 < 0$, we rewrite (B1) as

$$\bar{d}\gamma_{SE} + \frac{3}{2\bar{p}} - \frac{\Lambda_1(1 + \gamma_{SE}\bar{d}^2) + \Delta_1[\gamma_{SE}\bar{d} + 3/2\bar{p}]}{\Delta_1\sqrt{1 - 2\Lambda_1(\bar{\phi}^{3/2}/\beta + \gamma_{SE}\bar{p}\bar{d}^2 + \bar{p})/\Delta_1^2}} = 0, \quad (\text{B2})$$

Then, since $|\Delta_1| \gg 1$, we use the binomial theorem to expand the radical, resulting in

$$\bar{d}\gamma_{SE} + \frac{3}{2\bar{p}} - \frac{\Lambda_1(1 + \gamma_{SE}\bar{d}^2) + \Delta_1[\gamma_{SE}\bar{d} + 3/2\bar{p}]}{\Delta_1[1 - \Lambda_1(\bar{\phi}^{3/2}/\beta + \gamma_{SE}\bar{p}\bar{d}^2 + \bar{p})/\Delta_1^2]} = 0. \quad (\text{B3})$$

Next, since $\Lambda_1(\bar{\phi}^{3/2}/\beta + \gamma_{SE}\bar{p}\bar{d}^2 + \bar{p})/\Delta_1^2 \ll 1$, we can rewrite (B3) as

$$\bar{d}\gamma_{SE} + \frac{3}{2\bar{p}} - \frac{\{\Lambda_1(1 + \gamma_{SE}\bar{d}^2) + \Delta_1[\gamma_{SE}\bar{d} + 3/2\bar{p}]\}\{1 + \Lambda_1(\bar{\phi}^{3/2}/\beta + \gamma_{SE}\bar{p}\bar{d}^2 + \bar{p})/\Delta_1^2\}}{\Delta_1} = 0. \quad (\text{B4})$$

Distributing terms and looking at the relative orders-of-magnitudes of the terms in (B4) allows us to only consider the dominant terms, given by

$$1 + \frac{\Lambda_1\bar{\phi}^{3/2}}{\Delta_1^2\beta} + \frac{\Lambda_1}{\Delta_1^2}\bar{p} + \frac{3\bar{\phi}^{3/2}}{2\bar{p}\Delta_1\beta} + \frac{3}{2\Delta_1} = 0. \quad (\text{B5})$$

Multiplying through by Δ_1^2 yields

$$\Delta_1^2 + \frac{\Lambda_1\bar{\phi}^{3/2}}{\beta} + \Lambda_1\bar{p} + \frac{3\bar{\phi}^{3/2}}{2\bar{p}\beta}\Delta_1 + \frac{3}{2}\Delta_1 = 0. \quad (\text{B6})$$

Solving (B6) for \bar{p}_c requires further assessment of Δ_1 , which depends on pressure. Rearranging Δ_1 gives

$$\Delta_1 = \ln(\bar{\tau}/\bar{d}^2)/2 - 3/2 - \ln(\Lambda_1)/2 - \ln(\beta\bar{\phi}^{1/2}) - \bar{\phi}^{-1/2} - \gamma_{SE}\bar{p}\bar{d} - \ln(\bar{d}) - \ln(\bar{p}^{3/2}). \quad (\text{B7})$$

To simplify the $\ln(\bar{p}^{3/2})$ term, we define $\ln(\bar{p}^{3/2}) = \ln[\chi\bar{p}^{3/2}] - \ln[\chi]$, where we choose χ to make $\bar{p}^{3/2}\chi \approx 1$ so that we can take the series expansion of $\ln(\bar{p}^{3/2}\chi)$ and only consider the first order term. For $\bar{\alpha}\bar{d} \ll 1$, $\chi \approx 2 \times 10^7$. This allows us to rewrite Δ_1 as

$$\Delta_1 = \ln(\bar{\tau}/\bar{d}^2)/2 - 1/2 - \ln(\Lambda_1)/2 - \ln(\beta\bar{\phi}^{1/2}) - \bar{\phi}^{-1/2} - \ln(\bar{d}) + \ln(\chi) - \gamma_{SE}\bar{p}\bar{d} - \chi\bar{p}^{3/2}. \quad (\text{B8})$$

From here, we can define $X = \ln(\bar{\tau}/\bar{d}^2)/2 - 1/2 - \ln(\Lambda_1)/2 - \ln(\beta\bar{\phi}^{1/2}) - \bar{\phi}^{-1/2} - \ln(\bar{d}) + \ln(\chi)$, and rewrite (B8) as $\Delta_1 = X - \gamma_{SE}\bar{p}\bar{d} - \chi\bar{p}^{3/2}$, which we can insert into (B6) and consider dominant terms to obtain

$$\left(X^2 + \frac{\Lambda_1\bar{\phi}^{3/2}}{\beta} + \frac{3}{2}X\right)\bar{p} + \frac{3\bar{\phi}^{3/2}}{2\beta}X = 0. \quad (\text{B10})$$

Thus, solving (B10) for \bar{p} gives an analytic expression for the modified Paschen minimum as

$$\bar{p}_c = \frac{-3\bar{\phi}^{3/2}X}{2\beta X^2 + 2\Lambda_1\bar{\phi}^{3/2} + 3X\beta}. \quad (\text{B11})$$

APPENDIX C. UNIFICATION OF ELECTRON EMISSION MODEL DERIVATION

This Appendix details the derivation of the dimensionless breakdown and emission model characterized by the base equations in (6-1)-(6-6). Applying the dimensionless variable definitions from (6-7) to the various base equations yields the scaling parameters from (6-8) during the nondimensionalization process, which results in (6-9)-(6-14). Finally, certain simplifications can be considered for the microscale model to obtain closed form solutions for this regime. The QSCL derivation is detailed in 1, the CSCL, FN, and MG derivation is given in 2, the microscale exact, analytic, and limiting equations are derived in 3, and the dimensionless PL derivation is presented in 4.

1. Quantum Space-Charge Limited Emission

We first consider the quantum to Child-Langmuir, or QSCL to CSCL, transition. Starting with Schrödinger's equation, Poisson's equation, and the current density equation described in (6-5), (6-3), and (6-6), respectively, we first apply the dimensionless variable definitions from (6-7) to (6-5) to obtain

$$\frac{\hbar^2}{2mUL^2} \frac{d^2\bar{\psi}}{d\bar{x}^2} + \frac{eV_*\bar{V}}{U} \bar{\psi} + \bar{\psi} = 0. \quad (C1)$$

Defining $\bar{V} = eV_*\bar{V}/U$, or $U_* = eV_*$, and $L = [\hbar^2/(2m_e eE_*)]^{1/3}$, (C1) becomes

$$\frac{1}{\bar{U}} \frac{d^2 \bar{\psi}}{d\bar{x}^2} + \left(\frac{\bar{V}}{\bar{U}} + 1 \right) \bar{\psi} = 0 \quad (\text{C2})$$

We next apply the dimensionless variables to (6-3) to obtain

$$\frac{d^2 \bar{V}}{d\bar{x}^2} = \frac{eL^2 \psi_*^2}{V_* \epsilon_0} \bar{\psi} \bar{\psi}^*. \quad (\text{C3})$$

Setting $\psi_*^2 = \epsilon_0 V_*/(eL^2)$ and applying this to (C3) gives

$$\frac{d^2 \bar{V}}{d\bar{x}^2} = \bar{\psi} \bar{\psi}^*. \quad (\text{C4})$$

Now we can nondimensionalize (6-6) with the appropriate nondimensional definitions to obtain

$$\bar{J} = \frac{ie\hbar}{2m_e j_0} \frac{\psi_*^2}{L} \left[\bar{\psi} \frac{d\bar{\psi}^*}{d\bar{x}} - \bar{\psi}^* \frac{d\bar{\psi}}{d\bar{x}} \right]. \quad (\text{C5})$$

Applying the previously-derived definitions of $j_0, L,$ and ψ_* and setting $\bar{\phi}_* = [A_{FN}/\epsilon_0 t^2(y)]^2 [2m_e \hbar (0.95 B_{FN})/e^2]^{2/3}$ simplifies (C5) to

$$\bar{J} = i \left[\bar{\psi} \frac{d\bar{\psi}^*}{d\bar{x}} - \bar{\psi}^* \frac{d\bar{\psi}}{d\bar{x}} \right]. \quad (\text{C6})$$

Considering a wave of the form $\psi(\bar{x}) = (n_s \bar{U})^{1/2} p(\bar{x}) \exp(i\theta(\bar{x}))$ and its corresponding conjugate yields $\bar{\psi}(\bar{x}) = (n_s \bar{U} / \psi_*^2)^{1/2} p(\bar{x}) \exp(i\theta(\bar{x}))$. Thus, with $\bar{n} = \psi_*^2 / n_s$ and $\bar{q}(\bar{x}) = (\bar{U} / \bar{n})^{1/2} p(\bar{x})$, $\bar{\psi}(\bar{x}) = q(\bar{x}) \exp(i\theta(\bar{x}))$. Applying this to (C4) gives

$$\frac{d^2 \bar{V}}{d\bar{x}^2} = [q(\bar{x})]^2. \quad (\text{C7})$$

Taking the derivative of this dimensionless wave function and its conjugate yields

$$\frac{d\bar{\psi}}{d\bar{x}} = \exp(i\theta(\bar{x})) [i\theta'(\bar{x})q(\bar{x}) + q'(\bar{x})] \quad (\text{C8})$$

and

$$\frac{d\bar{\psi}^*}{d\bar{x}} = \exp(-i\theta(\bar{x})) [-i\theta'(\bar{x})q(\bar{x}) + q'(\bar{x})]. \quad (\text{C9})$$

Additionally, we can take a second derivative of (C8) with respect to the spatial direction to obtain

$$\frac{d^2 \bar{\psi}}{d\bar{x}^2} = \exp(i\theta(\bar{x})) [i\theta''(\bar{x})q(\bar{x}) + 2i\theta'(\bar{x})q'(\bar{x}) + q''(\bar{x}) - (\theta'(\bar{x}))^2 q(\bar{x})]. \quad (\text{C10})$$

Applying (C7) and (C8) to (C6), along with the definition of the dimensionless wave function and its conjugate yields

$$\bar{J} = 2\theta'(\bar{x})q^2(\bar{x}). \quad (\text{C11})$$

Next, we simplify (C2) by noting $d\bar{J}/d\bar{x} = 2i\theta'(\bar{x})q'(\bar{x}) + i\theta''(\bar{x})q(\bar{x}) = 0$ and defining $\lambda_q = 2\bar{J}/\bar{U}^{3/2}$ to give

$$\frac{1}{\bar{U}} \frac{d^2 \bar{q}}{d\bar{x}^2} + \left(\frac{\bar{V}}{\bar{U}} - \frac{(\lambda_q/4)^2}{[q(\bar{x})]^4} \right) q(\bar{x}) = 0 \quad (\text{C12})$$

Numerically solving (C7), (C11), and (C12) simultaneously yields the transition point between QSCL and CSCL, and is represented by the QSCL points in Figs. 6.7.

2. FN, CSCL, and MG Emission

We next consider the FN, CSCL, and MG derivation. Starting from Poisson's equation and the force balance with mobility introduced in (6-3) and (6-4), respectively, we first insert the dimensionless parameter definitions into the force balance equation to obtain

$$\frac{d\bar{v}}{d\bar{t}} = \frac{et_*^2 E_*}{m_e L} \frac{d\bar{V}}{d\bar{x}} - \frac{et_*}{m_e \mu_*} \frac{\bar{v}}{\bar{\mu}}. \quad (\text{C13})$$

Setting $t_*^2 = m_e L / e E_*$ and $\mu_* = et_* / m_e$ and coupling with (C13) yields

$$\frac{d\bar{v}}{d\bar{t}} = \frac{d\bar{V}}{d\bar{x}} - \frac{\bar{v}}{\bar{\mu}}. \quad (\text{C14})$$

Next, we insert the dimensionless variable definitions into Poisson's equation and simplify as

$$\frac{d^2\bar{V}}{d\bar{x}^2} = \frac{j_0\tau_*\bar{J}}{E_*\epsilon_0\bar{v}}. \quad (\text{C15})$$

After substituting in the definitions for j_0 , t_* , and E_* , we obtain

$$\frac{d^2\bar{V}}{d\bar{x}^2} = \omega \frac{\bar{J}}{\bar{v}}, \quad (\text{C16})$$

where $\omega = 1/\sqrt{2}$. We next perform a change of variables on (C14) considering $\bar{v} = d\bar{x}/d\bar{t}$. Thus, taking another derivative with respect to the spatial component in (C14) yields

$$\frac{d}{d\bar{x}} \left[\bar{v} \frac{d\bar{v}}{d\bar{x}} \right] = \frac{d\bar{v}}{d\bar{x}} \frac{d\bar{v}}{d\bar{x}} + \bar{v} \frac{d^2\bar{v}}{d\bar{x}^2} = \frac{d^2\bar{V}}{d\bar{x}^2} - \frac{1}{\bar{\mu}} \frac{d\bar{v}}{d\bar{x}}. \quad (\text{C17})$$

Applying (C16) and reverting back to \bar{t} yields

$$\omega\bar{J} = \frac{d\bar{x}}{d\bar{t}} \frac{d}{d\bar{x}} \frac{d\bar{x}}{d\bar{t}} \frac{d\bar{v}}{d\bar{x}} + \frac{1}{\bar{\mu}} \frac{d\bar{x}}{d\bar{t}} \frac{d\bar{v}}{d\bar{x}}, \quad (\text{C18})$$

which simplifies to

$$\bar{J} = \frac{1}{\omega} \frac{d^2\bar{v}}{d\bar{t}^2} + \frac{1}{\omega\bar{\mu}} \frac{d\bar{v}}{d\bar{t}}. \quad (\text{C19})$$

From here, we solve for $\bar{v}(\bar{t})$ from (C19) as

$$\bar{v}(\bar{t}) = \omega\bar{J}\bar{\mu}\bar{t} - \bar{\mu} \exp(-\bar{t}/\bar{\mu}) C_1 + C_2. \quad (\text{C20})$$

Using the boundary conditions of $\bar{v}(0) = 0$ and $d\bar{v}/d\bar{t} = \bar{E}$ and $\bar{t} = 0$ yields $C_1 = \bar{E} - \omega\bar{J}\bar{\mu}$ and $C_2 = \bar{\mu}[\bar{E} - \omega\bar{J}\bar{\mu}]$. Thus, we arrive at the equation of velocity and position given by

$$\bar{v}(\bar{t}) = \bar{\mu}\{(\omega\bar{J}\bar{\mu} - \bar{E})[\exp(-\bar{t}/\bar{\mu}) - 1] + \omega\bar{J}\bar{t}\}, \quad (\text{C21})$$

and

$$\bar{x}(\bar{t}) = \bar{\mu} \left\{ (\omega\bar{J}\bar{\mu} - \bar{E})[-\bar{\mu} \exp(-\bar{t}/\bar{\mu}) - \bar{t} + \bar{\mu}] + \frac{\omega\bar{J}\bar{t}^2}{2} \right\}, \quad (\text{C22})$$

respectively. Integrating the dimensionless force balance in (C14) yields

$$\bar{V}(\bar{t}) = \frac{\bar{v}(\bar{t})^2}{2} \Big|_0^{\bar{t}} + \int_0^{\bar{t}} d\bar{t} \frac{\bar{v}(\bar{t})^2}{\bar{\mu}}. \quad (\text{C23})$$

Numerically solving (C21)-(C23) yields the exact solution in Figs. 6.5 and 6.6. We next consider the high mobility limit, where we apply the expansion $\exp(-\bar{t}/\bar{\mu}) \approx 1 - \bar{t}/\bar{\mu} + \bar{t}^2/2\bar{\mu}^2$. Inserting this into (C21) and (C22) yields

$$\bar{v}(\bar{t}) = \bar{E}\bar{t} + \frac{\omega}{2}\bar{J}\bar{t}^2 \quad (\text{C24})$$

and

$$\bar{x}(\bar{t}) = \frac{\bar{E}\bar{t}^2}{2} + \frac{\omega}{6}\bar{J}\bar{t}^3. \quad (\text{C25})$$

We can now solve for the dimensionless transit time, $\bar{\tau}$, considering $\bar{v}(\bar{\tau}) = \sqrt{2\bar{V}}$ since the first term on the RHS of (C23) dominates in this limit. Coupling this with (C24) yields

$$\bar{\tau} = \frac{\left(-\bar{E} + \sqrt{\bar{E}^2 - 2(2\bar{V})^{1/2}\omega\bar{J}}\right)}{\omega\bar{J}}. \quad (\text{C26})$$

Next, inserting (C6) into (C26) results in

$$\bar{\tau} = \frac{\xi_1 \bar{\phi} \exp(\bar{\phi}^{3/2}/\beta\bar{E})}{\bar{E}\omega\beta^2 \exp(\Gamma/\bar{\phi}^{1/2})}, \quad (\text{C27})$$

where

$$\xi_1 = -1 + \sqrt{1 - \frac{2(2\bar{V})^{1/2}\omega\beta^2}{\bar{\phi}} \exp\left(-\frac{\bar{\phi}^{3/2}}{\beta\bar{E}}\right) \exp\left(\frac{\Gamma}{\bar{\phi}^{1/2}}\right)}. \quad (\text{C28})$$

Inserting (C27) and (C28) into (C25) and noting $\bar{x}(\bar{\tau}) = \bar{D}$ gives the high mobility limit of

$$6\bar{D}\bar{E}\bar{\phi}^{-2} \exp\left(-\frac{2\bar{\phi}^{3/2}}{\beta\bar{E}}\right) \exp\left(\frac{2\Gamma}{\bar{\phi}^{1/2}}\right) \omega^2 \beta^4 = \xi_1^2(\xi_1 + 3). \quad (\text{C29})$$

Further inspecting (C28) and (C29) gives two further limits: large and small \bar{V} . At large \bar{V} ,

$$\xi_2 = \sqrt{\frac{2(2\bar{V})^{1/2}\omega\beta^2}{\bar{\phi}} \exp\left(-\frac{\bar{\phi}^{3/2}}{\beta\bar{E}}\right) \exp\left(\frac{\Gamma}{\bar{\phi}^{1/2}}\right)}. \quad (\text{C30})$$

Inserting (C30) into (C29), noting that $\xi_2^2(\xi_2 + 3) \approx \xi_2^3$ at this limit, and simplifying yields

$$(\bar{J}\bar{D}^2)_{CSCL} = \frac{4\sqrt{2}\bar{V}^{3/2}}{9\omega}, \quad (\text{C31})$$

which is the traditional scaling for CSCL and is used for the CSCL calculations in Figs. 6.5 and

6.6. Alternatively, at small \bar{V} ,

$$\xi_3 = -\frac{(2\bar{V})^{1/2}\omega\beta^2}{\bar{\phi}} \exp\left(-\frac{\bar{\phi}^{3/2}}{\beta\bar{E}}\right) \exp\left(\frac{\Gamma}{\bar{\phi}^{1/2}}\right). \quad (\text{C32})$$

Noting $\xi_3^2(\xi_3 + 3) \approx 3\xi_3^2$ in this limit and applying (C32) to (C29), we obtain

$$(\bar{J}\bar{D}^2)_{FN} = \frac{\bar{V}^2\beta^2}{\bar{\phi}} \exp\left(-\frac{\bar{\phi}^{3/2}\bar{D}}{\beta\bar{V}}\right) \exp\left(\frac{\Gamma}{\bar{\phi}^{1/2}}\right), \quad (\text{C33})$$

demonstrating $\bar{V} = \bar{E}\bar{D}$ and the standard FN behavior, shown as the FN limits in Figs. 6.5 and 6.6. Alternatively, for the low mobility limit of $\bar{\mu} \ll 1$, $\exp(-\bar{t}/\bar{\mu}) \approx 0$. Applying this to (C21) and (C22) yields

$$\bar{v}(\bar{t}) = \bar{\mu}(\bar{E} + \omega\bar{J}\bar{t}), \quad (\text{C34})$$

and

$$\bar{x}(\bar{t}) = \bar{\mu} \left(\bar{E}\bar{t} + \frac{\omega\bar{J}\bar{t}^2}{2} \right). \quad (\text{C35})$$

To find the dimensionless transit time in this limit, we again set (C33) equal to 0 at $\bar{t} = \bar{\tau}$, resulting in

$$\bar{\tau} = \frac{\xi_4 \bar{E}}{\omega\bar{J}}, \quad (\text{C36})$$

where

$$\xi_4 = -1 + \sqrt{1 + \frac{2\omega\bar{J}\bar{D}}{\bar{\mu}\bar{E}^2}}. \quad (\text{C37})$$

To explicitly solve (C23), we first simplify the first term on the right-hand side (RHS) of (C23) to obtain

$$\left. \frac{\bar{v}(\bar{t})^2}{2} \right|_0^{\bar{t}} = \frac{\bar{\mu}^2 \bar{E}^2}{2} (1 + 2\xi_4 + \xi_4^2). \quad (\text{C38})$$

Then, we simplify the second term on the RHS of (C23) as

$$\int_0^{\bar{t}} d\bar{t} \frac{\bar{v}(\bar{t})^2}{\bar{\mu}} = \frac{\bar{\mu} \bar{E}^3}{\omega \bar{J}} \left(\xi_4 + \xi_4^2 + \frac{\xi_4^3}{3} \right). \quad (\text{C39})$$

Combining (C38) and (C39) yields

$$\bar{V} = \frac{\bar{\mu}^2 \bar{E}^2}{2} (1 + 2\xi_4 + \xi_4^2) + \frac{\bar{\mu} \bar{E}^3}{\omega \bar{J}} \left(\xi_4 + \xi_4^2 + \frac{\xi_4^3}{3} \right). \quad (\text{C40})$$

Since $\bar{\mu} \ll 1$, the second term on the RHS of (C40) dominates, resulting in

$$\bar{V} \approx \frac{\bar{\mu} \bar{E}^3}{\omega \bar{J}} \left(\xi_4 + \xi_4^2 + \frac{\xi_4^3}{3} \right). \quad (\text{C41})$$

For $\bar{\mu} \ll 1$, $\xi_4 \approx \sqrt{2\omega \bar{J} \bar{D} / \bar{\mu} \bar{E}^2}$. This limit also gives $\xi_4 \gg 1$, meaning $\xi_4^3/3$ dominates in (C39).

Applying these simplifications to (C41) yields

$$(\bar{D}^2)_{MG} = \frac{9}{8} \frac{\bar{\mu} \bar{V}^2}{\omega \bar{D}}, \quad (\text{C42})$$

which is consistent with expected MG scaling and calculates the MG limits in Figs. 6.5 and 6.6.

3. Microscale Breakdown

We next consider the microscale breakdown criterion given by

$$F_{br} = \frac{2E^2 v_a \varepsilon_0 \{1 - \gamma_{SE} [\exp(\alpha d) - 1]\}}{D_{FN} d J_{FN}} = \frac{\exp(x_0) (1 + 2\bar{E} x_0)}{x_0}, \quad (C43)$$

where variable definitions are defined in the main text. The first goal is to nondimensionalize (C43), and then apply simplifying assumptions to obtain an analytic solution. Taking the product of the ionization coefficient and gap distance as

$$\alpha d = A_p p d \exp\left(-\frac{B_p p}{E}\right) \quad (C44)$$

and applying the dimensionless variables from (6-7) yields

$$\bar{\alpha} \bar{d} = (A_p p_* L) \bar{p} \bar{d} \exp(-\bar{p} p_* B_p / \bar{E} E_*). \quad (C45)$$

Defining $p_* = E_*/B_p$ yields

$$\bar{\alpha} \bar{d} = (A_p p_* L) \bar{p} \bar{d} \exp(-\bar{p} / \bar{E}). \quad (C46)$$

Next, we consider the Fowler-Nordheim current density equation given by

$$J_{FN} = C_{FN} E^2 \exp\left(-\frac{D_{FN}}{E}\right) \quad (\text{C47})$$

and apply the appropriate definitions to obtain

$$\bar{J}\bar{J}_0 = \frac{A_{FN}\beta^2}{\bar{\phi}\phi_*\tau^2(y)} \exp\left[\frac{(3.79 \times 10^{-4})^2 B_{FN}}{\bar{\phi}^{\frac{1}{2}}\phi_*^{\frac{1}{2}}}\right] \bar{E}^2 E_*^2 \exp\left(-\frac{0.95 B_{FN} \bar{\phi}^{\frac{3}{2}} \phi_*^{\frac{3}{2}}}{\beta \bar{E} E_*}\right). \quad (\text{C48})$$

Defining $E_* = 0.95 B_{FN} \phi_*^{3/2}$, $J_0 = A_{FN}/(\phi_* t^2(y))$, and $\Gamma = (3.79 \times 10^{-4})^2 B_{FN}/\phi_*^{1/2}$ yields

$$\bar{J} = \frac{\beta^2 \bar{E}^2}{\bar{\phi}} \exp\left(-\frac{\bar{\phi}^{\frac{3}{2}}}{\beta \bar{E}}\right) \exp\left(\frac{\Gamma}{\bar{\phi}^{\frac{1}{2}}}\right). \quad (\text{C49})$$

Plugging (C46) and (C49) into (C43) yields a dimensionless, numerical form of the microscale breakdown equation given by

$$\frac{2\varepsilon_0 \exp\left(\frac{\bar{\phi}^{3/2}}{\beta \bar{E}}\right) \tau^2(y)}{0.95 B_{FN} \phi_*^{1/2} \bar{\phi}^{1/2} L A_{FN} \beta \exp(\Gamma/\bar{\phi}^{1/2})} \sqrt{\frac{2ekT_* B_p}{\pi m_g \sigma_{ce}}} \sqrt{\frac{\bar{T} \bar{E}}{\bar{p} \bar{d}^2} \frac{\{1 - \gamma_{SE} [\exp(\bar{\alpha} \bar{d}) - 1]\}}{[\exp(\bar{\alpha} \bar{d}) - 1]}} \quad (\text{C50})$$

$$= \exp(x_0) (1 + 2\bar{E}x_0)/x_0.$$

This is what is referred to as the “exact” solution in Figure 6.3. Upon inspection, there are two simplifications we can make to (C50) for small gaps, which is the regime of interest for the

transition to MG and/or CSCL. First, $\bar{E} \ll 1$, so $x_0 = (\sqrt{1 + 8\bar{E}} - 1)/4\bar{E} \approx (1 + 4\bar{E} - 1)/4\bar{E} = 1$. Second, since this transition will be occurring at small gap distance, we can assume $\bar{\alpha}\bar{d} \ll 1$ and γ_{SE} is negligible (Tholeti, Shivkumar, & Alexeenko, 2016). Thus, $\exp(\bar{\alpha}\bar{d}) - 1 \approx \bar{\alpha}\bar{d}$. Applying these simplifications to (C50) and defining

$$T_* = \frac{\pi m_g \sigma_{ce}}{2ekB_p} \left[\frac{0.95 B_{FN} \bar{\phi}^{\frac{3}{2}} A_{FN} \beta^2 L^2 A_p p_*}{2 \varepsilon_0 \phi_* \tau^2(\gamma)} \right] \quad (\text{C51})$$

yields a numerical equation for the $\bar{\alpha}\bar{d} \ll 1$ case as

$$\frac{\exp(\bar{p}/E) \exp\left(\frac{\bar{\phi}^{\frac{3}{2}}}{\beta \bar{E}}\right)}{\bar{p} \bar{d}^2 \bar{\phi}^{\frac{1}{2}} \beta \exp\left(\Gamma/\bar{\phi}^{\frac{1}{2}}\right)} \sqrt{\frac{\bar{T}\bar{E}}{\bar{p}}} = \exp(1) (1 + 2\bar{E}). \quad (\text{C52})$$

To obtain the analytic solution, we first take the natural log of both sides and apply $\ln(1 + 2\bar{E}) \approx 2\bar{E}$ and $[\ln(\bar{T}\bar{E}/\bar{p})]/2 = [\ln(\bar{T}/\bar{p})]/2 + [\ln \bar{E}]/2 \approx [\ln(\bar{T}/\bar{p})]/2 + [\ln \Lambda_3 \bar{E}]/2 - [\ln \Lambda_3]/2 \approx [\ln(\bar{T}/\bar{p})]/2 - 1/2 + \Lambda_3 \bar{E}/2 - [\ln \Lambda_3]/2$, where $\Lambda_3 \bar{E} \approx 1$ (here, $\Lambda_3 = 1.5 \times 10^3$), to obtain

$$\begin{aligned} \left(\frac{\Lambda_3}{2} - 2\right) \bar{E}^2 + \left[\frac{[\ln(\bar{T}/\bar{p})] - 3 - \ln(\Lambda_3)}{2} - \frac{\Gamma}{\bar{\phi}^{1/2}} - \ln(\bar{p} \bar{d}^2) - \ln(\beta \bar{\phi}^{1/2}) \right] \bar{E} \\ + \left(\bar{p} + \frac{\bar{\phi}^{3/2}}{\beta} \right) = 0. \end{aligned} \quad (\text{C53})$$

Defining the coefficient of \bar{E}^2 as X_1 , the coefficient of \bar{E} as X_2 , and the third term in parentheses as X_3 , we can solve for an analytic solution for \bar{V} in the form of a quadratic as

$$\bar{V} = \bar{d} \frac{(-X_2 - \sqrt{X_2^2 - 4X_1X_3})}{2X_1}. \quad (\text{C54})$$

Figure 6.3 refers to (C54) as the microscale analytic equation. Finally, to obtain the limiting equation, we note that $X_2 \gg 1$ and apply the binomial theorem within the quadratic to obtain

$$\bar{V} = \frac{X_3}{X_2} \bar{d}, \quad (\text{C55})$$

which is the microscale limit in Figure 6.4.

4. Paschen's Law: Townsend Avalanche

Finally, we consider Paschen's law (PL). Applying the dimensionless variables from (6-7) to the base equation outlined in (6-1) gives

$$\bar{V} = \frac{\bar{p}\bar{d}}{\ln(A_p p_* L \bar{p}\bar{d}) - \ln[\ln(1 + \gamma_{SE}^{-1})]}. \quad (\text{C56})$$

At this point, we have already defined all of our scaling parameters, so we must define one dimensionless, material-dependent term as $\Omega = A_p E_* L / B_p$. Thus, (C56) becomes

$$\bar{V} = \frac{\bar{p}\bar{d}}{\ln(\Omega\bar{p}\bar{d}) - \ln[\ln(1 + \gamma_{SE}^{-1})]} \quad (\text{C57})$$

Figures 6.1 and 6.2 show (C57) for various gases under different conditions.

In summary, this Appendix derived a breakdown and emission model including QSCL, CSCL, FN, coupled field emission/Townsend avalanche (microscale), and traditional PL regimes. This theory is universal from the QSCL up to (but not including) the dimensionless PL.

REFERENCES

- Abeyasinghe, D. C., Dasgupta, S., Boyd, J. T., & Jackson, H. E. (2001) A novel MEMS pressure sensor fabricated on an optical fiber. *IEEE Photonics Technology Letters*, 13, 993-995.
- Ang, L. K., Koh, W. S., Lau, Y. Y., and Kwan, T. J. T. (2006) Space-charge-limited flows in the quantum regime. *Physics of Plasmas*, 13, 056701.
- Ang, L. K., Kwan, T. J. T., and Lau, Y. Y. (2003). New scaling of Child-Langmuir law in the quantum regime. *Physical Review Letters*, 91, 208303.
- Ang, L. K., Lau, Y. Y., and Kwan, T. J. T. (2004) Simple derivation of quantum scaling in Child-Langmuir law. *IEEE Transactions on Plasma Science*, 32, 410-421.
- Asokan, T. & Sudarshan, T. S. (1993) Dependence of the surface flashover properties of alumina on polishing abrasive parameters. *IEEE Transactions on Electrical Insulation*, 28, 535-544.
- Aussems, D. U. B., Nishijimi, D., Brandt, C., van der Meiden, H. J., Vilemova, M., Matejicek, J., De Temmerman, G., Doerner, R. P., Lopes Cardozo, N. J. (2015) The occurrence and damage of unipolar arcing on fuzzy tungsten. *Journal of Nuclear Materials* 463, 303-307.
- Bakhtiari, M., Kramer, G. J., Takechi, M., Tamai, H., Miura, Y., Kusama, Y., and Kamada, Y. (2005) Role of bremsstrahlung radiation in limiting the energy of runaway electrons in tokamaks. *Physical Review Letters*, 94, 215003.
- Baille, P., Chang, J. S., Claude, A., Hobson, R. M., Ogram, G. L., & Yau, A. W. (1981) Effective collision frequency of electrons in noble gases. *Journal of Physics B: Atomic and Molecular Physics*, 14, 1485-1495.
- Baranov, O. O., Xu, S., Xu, L., Huang, S., Lim, J., Cvelbar, U., Levchenko, I., and Bazaka, K. (2018) Miniaturized plasma sources: Can technological solutions help electric micropropulsion? *IEEE Transactions on Plasma Science*, 46, 230-238.
- Becker, K. *Microplasmas, A platform technology for a plethora of plasma applications*. 2017: Springer.
- Becker, K. H. (2010) *The Use of Nonthermal Plasmas in Environmental Applications*, in *Introduction to Complex plasmas*, Springer. 367-394.
- Becker, K., Koutsospyros, A., Yin, S. M., Christodoulatos, C., Abramzon, N., Joaquin, J. C., and Brelles-Marino, G. (2005) Environmental and biological applications of microplasmas. *Plasma Physics and Controlled Fusion*, 47, B513-B523.
- Becker, K. H., Schoenbach, K. H., and Eden, J. G. (2006) Microplasmas and applications. *Journal of Physics D: Applied Physics*, 39, R55-R70.

- Benilov, M. S. (2000) Collision-dominated to collisionless electron-free space-charge sheath in a plasma with variable ion temperature. *Physics of Plasmas*, 7, 4403-4411.
- Benilov, M. S. (2009) The Child-Langmuir law and analytical theory of collisionless to collision-dominated sheaths. *Plasma Sources Science and Technology*, 18, 014005.
- Bhattacharjee, S. and Chowdhury, T. (2009) Experimental investigation of transition from Fowler-Nordheim field emission to space-charge-limited flows in a nanogap. *Applied Physics Letters* 92, 191503.
- Bhattacharjee, S., Vartak, A., and Mukherjee, V. (2008) Experimental study of space-charge-limited flows in a nanogap. *Applied Physics Letters* 92, 191503.
- Bilici, M. A., Haase, J. R., Boule, C. R., Go, D. B., and Sankaran, R. M. (2016) The smooth transition from field emission to a self-sustained plasma in microscale electrode gaps at atmospheric pressure. *Journal of Applied Physics*, 119, 223301.
- Biswas, J. C. and Mitra, V. (1979) High-frequency breakdown and Paschen law, *Applied Physics*, 19, 377-381.
- Bogue, R. (2007) MEMS sensors: Past, present, and future. *Sensor Review*, 27, 7–13.
- Booske, J. H. (2008) Plasma physics and related challenges of millimeter-wave-to-terahertz and high power microwave generation, *Physics of Plasmas*, 15, 055502.
- Booske, J. H., Dobbs, R. J., Joye, C. D., Kory, C. L., Neil, G. R., Park, G. S., Park, J. and Temkin, R. J. (2011) Vacuum electronic high power terahertz sources, *IEEE Transactions on Terahertz Science and Technology*, 1, 54-75.
- Boyle, W. S. & Kisliuk, P. (1955) Departure from Paschen's law of breakdown in gases. *Physical Review*, 97, 255-259.
- Braun, H. H., Döbert, S., Wilson, I., and Wuensch, W. (2003) Frequency and temperature dependence of electrical breakdown at 21, 30, and 39 GHz. *Physical Review Letters*, 90, 224801.
- Brayfield, II, R. S., (2020) "Electrode effects on electron emission and gas breakdown from nano to microscale," Ph.D. dissertation, Dept. Agr. Biol. Eng., Purdue Univ., West Lafayette, IN.
- Brayfield, II, R. S., Fairbanks, A. J., Loveless, A. M., Gao, S., Dhanabal, A., Li, W., Darr, C., Wu, W. and Garner, A. L. (2019) The Impact of Cathode Surface Roughness and Multiple Breakdown Events on Microscale Gas Breakdown at Atmospheric Pressure, *Journal of Applied Physics*, 125, 203302.

- Buendia, J. A. and Venkatraman, A. (2015) Field enhancement factor dependence on electric field and implications on microscale gas breakdown: Theory and experimental interpretation. *Europhysics Letters*, *112*, 55002.
- Buzarbaruah, N., Dutta, N. J., Borgohain, D., Mohanty, S. R., and Bailung, H. (2017) Study on discharge plasma in a cylindrical inertial confinement fusion device. *Physical Letters A* *381*, 2391-2396.
- Campbell, J. D., Bowman III, A., Lenters, G. T., and Remillard, S. K. (2014) Collision and diffusion in microwave breakdown of nitrogen gas in and around microgaps, *AIP Advances*, *4*, 017119.
- Chang, C. Y., Sasaki, M., Kumagai, S., & Wang, G. J. (2016) Design of microplasma electrodes for plasma-on-chip devices. *Journal of Physics D: Applied Physics*, *49*, 155203.
- Chen, C. H., Yeh, J. A., & Wang, P. J. (2006) Electrical breakdown phenomena for devices with micron separations. *Journal of Micromechanics and Microengineering*, *16*, 1366-1373.
- Child, C. D. (1911) Discharge from hot CaO. *Physical Review (Series I)*, *32*, 492-511.
- Collins, P. G., Hersam, M., Arnold, M., Martel, R., and Avouris, P. (2001) Current saturation and electrical breakdown in multiwalled carbon nanotubes. *Physical Review Letters* *86*, 3128-3131.
- Cook, A., Shapiro, M., and Temkin, R. (2010) Pressure dependence of plasma structure in microwave gas breakdown at 110 GHz, *Applied Physics Letters*, *97*, 011504.
- Cook, A. M., Hummelt, J. S., Shapiro, M. A., and Temkin, R. J. (2011) Measurements of electron avalanche formation time in W-band microwave air breakdown, *Physics of Plasmas*, *18*, 080707.
- Craighead, H. Nanoelectromechanical systems. (2000) *Science*, *290*, 1532–1535.
- Darr, A. M., Loveless, A. M., and Garner, A. L. (2019) Unification of field emission and space charge limited emission with collisions. *Applied Physics Letters*, *114*, 014103.
- Darr, A. M., Darr, C. R., Garner, A. L. (2020) Theoretical assessment of transitions across thermionic, field, and space-charge limited emission. *Physical Review Research*, accepted.
- Davydov, Y. I. (2006) On the first Townsend coefficient at high electric field. *IEEE Transactions on Nuclear Science*, *53*, 2931-2935.
- Descoedres, A., Levinsen, Y., Calatroni, S., Taborelli, M., and Wuensch, W. (2009) Investigation of the dc vacuum breakdown mechanism. *Physical Review Special Topics-Accelerators and Beams*, *12*, 092001.

- Dhariwal, R. S., Torres, J. M., Desmulliez, M. P. Y. (2000) Electric field breakdown at micrometer separations in air and nitrogen at atmospheric pressure. *IEEE Proceedings-Science, Measurement and Technology*, 147, 261-265.
- Dynako, S. D., Loveless, A. M., and Garner, A. L. (2018) Sensitivity of modeled microscale gas breakdown voltage due to parametric variation. *Physics of Plasmas*, 25, 103505.
- Elkholy, A., Shoshyn, Y., Nijdam, S., van Oijen, J., van Veldhuizen, E., Ebert, U., and de Goey, L. (2018) Burning Velocity Measurement of Lean Methane-Air Flames in a New Nanosecond DBD Microplasma Burner Platform. *Experimental Thermal and Fluid Science*, 95, 18-26.
- Eun, C. K. and Gianchandani, Y. B. (2012) Microdischarge-based sensors and actuators for portable microsystems: Selected examples. *IEEE Journal of Quantum Electronics*, 48, 814-826.
- Farish, O. & Crichton, B. H. (1976) Effect of electrode surface roughness on breakdown in nitrogen/SF₆ mixtures. *Proceedings of the Institution of Electrical Engineers*, 123, 1047-1050.
- Feng, Y. and Verboncoeur, J. P. (2006) Transition from Fowler-Nordheim field emission to space charge limited current density. *Physics of Plasmas*, 13, 073105.
- Feng, Y., Verboncoeur, J. P., & Lin, M. C. (2008) Solution for space charge limited field emission current densities with injection velocity and geometric effects corrections. *Physics of Plasmas*, 15, 043301.
- Fowler, R. H. & Nordheim, L. (1928) Electron emission in intense electric fields. *Proceedings of the Royal Society of London. Series A, Containing Papers of a Mathematical and Physical Character*, 119, 173-181.
- Friedland, L. (1974) Electron multiplication in a gas discharge at high values of E/P. *Journal of Physics D: Applied Physics*, 7, 2246-2253.
- Fu, Y., Krek, J., Zhang, P., and Verboncoeur, J. P. (2018) Evaluating microgap breakdown mode transition with electric field non-uniformity. *Plasma Sources Science and Technology*, 27, 095014.
- Fu, Y., Yang, S., Zou, X., Luo, H., and Wang, X. (2017) Effect of distribution of electric field on low-pressure gas breakdown. *Physics of Plasmas*, 24, 023508.
- Fu, Y., Krek, J., Zhang, P., and Verboncoeur, J. P. (2018) Gas breakdown in microgaps with a surface protrusion on the electrode. *IEEE Transactions on Plasma Science*, 47, 2011-2019.

- Garner, A. L., Caiafa A., Jiang, Y., Klopman, S., Morton, C., Torres, A. S., Loveless, A. M., and Neculaes, V. B. (2017) Experimental validation of a compact, flexible pulsed power architecture for ex vivo platelet activation. *PLoS ONE*, 12, e0181214.
- Garner, A. L., Loveless, A. M., Dahal, J. N., and Venkatraman, A. (2020) A tutorial on theoretical and computational techniques for gas breakdown in microscale gaps. *IEEE Transactions on Plasma Science*, 48, 808-824.
- Go, D. B. & Pohlman, D. A. (2010) A mathematical model of the modified Paschen's curve for breakdown in microscale gaps. *Journal of Applied Physics*, 107, 103303.
- Go, D. B. & Venkatraman, A. (2014) Microscale gas breakdown: ion-enhanced field emission and the modified Paschen's curve. *Journal of Physics D: Applied Physics*, 47, 503001.
- Gopinath, V. P., Verboncoeur, J. P., and Birdsall, C. K. (1998) Multipactor electron discharge physics using an improved secondary emission model. *Physics of Plasmas*, 5, 1535-1540.
- Hammond, K. C., Raman, R., and Volpe, F. A., (2018) Application of Townsend avalanche theory to tokamak startup by coaxial helicity, *Nuclear Fusion*, 58, 016013.
- Handa, T. & Minamitani, Y. (2009) The effect of a water-droplet spray and gas discharge in water treatment by pulsed power. *IEEE Transactions on Plasma Science*, 37, 179-183.
- Haase, J. R. & Go, D. B. 2016 Analysis of thermionic and thermos-field emission in microscale gas discharges. *Journal of Physics D: Applied Physics*, 49, 055206.
- Hidaka, Y., Choi, E. M., Matovsky, I., Shapiro, M. A., Sirigiri, J. R., Temkin, R. J., Edmiston, G. F., Neuber, A. A., and Oda, Y. (2009) Plasma structures observed in gas breakdown using a 1.5 MW, 110 GHz pulsed gyrotron, *Physics of Plasmas*, 16, 055702.
- Hourdakis, E., Simonds, B. J., & Zimmerman, N. M. (2006) Submicron gap capacitor for measurement of breakdown voltage in air. *Review of Scientific Instruments*, 77, 034702.
- Huxley, L. H. G., Crompton, R. W., & Elford, M. T. (1966) Use of the parameter E/N. *British Journal of Applied Physics*, 17, 1237-1238.
- Ito, T., Izaki, T., & Terashima, K. (2001) Application of microscale plasma to material processing. *Thin Solid Films*, 386, 300-304.
- Iza, F., Kim, G. J., Lee, S. M., Lee, J. K., Walsh, J. L., Zhang, Y. T., and Kong, M. G. (2008) Microplasmas: Sources, particle kinetics, and biomedical applications. *Plasma Processes and Polymers*, 5, 322-344.
- Jensen, K. L. (2003) Electron emission theory and its application: Fowler-Nordheim equation and beyond. *Journal of Vacuum Science and Technology B: Microelectronics and Nanometer Structures Processing, Measurement, and Phenomena*, 21, 1528-1544.

- Jensen, K. L. (2018) A tutorial on electron sources. *IEEE Transactions on Plasma Science*, 46, 1881-1899.
- Jensen, K. L., McDonald, M., Chubenko, O., Harris, J. R., Shiffler, D. A., Moody, N. A., Petillo, J. J., and Jensen, A. J. (2019) Thermal-field and photoemission from meso- and micro-scale features: effects of screening and roughness on characterization and simulation. *Journal of Applied Physics*, 125, 234303.
- Joffrion, J. B., Mills, D., Clower, W., and Wilson, C. G. (2017) On-Chip Microplasmas for the Detection of Radioactive Cesium Contamination in Seawater. *Micromachines*, 8, 259.
- Ju, Y. and Sun, W. (2015) Plasma assisted combustion: Dynamics and chemistry. *Progress in Energy and Combustion Science*, 48, 21-83.
- Kihara, T. (1952) The mathematical theory of electrical discharges in gases, *Review of Modern Physics*, 24, 45-61.
- Kim, K. S., Hurtado, J. A., and Tan, H. (1999) Evolution of a surface-roughness spectrum caused by stress in nanometer-scale chemical etching. *Physical Review Letters*, 83, 3872-3875.
- Kim, K., Park, S., and Eden, J. (2007) Self-patterned aluminium interconnects and ring electrodes for arrays of microcavity plasma devices encapsulated in Al₂O₃. *Journal of Physics D: Applied Physics*, 41, 012004.
- Kishek, R. A., Lau, Y. Y., Ang, L. K., Valfells, A., and Gilgenbach, R. M. (1998) Multipactor discharge on metals and dielectrics: Historical review and recent theories. *Physics of Plasmas*, 5, 2120-2126.
- Kishek, R. A. (2013) Ping-pong modes and higher-periodicity multipactor. *Physics of Plasmas*, 20, 056702.
- Klas, M., Radmilovic-Radjenovic, M., Radjenovic, B., Stan, M., & Matejcik, S. (2012) Transport parameters and breakdown voltage characteristics of dry air and its constituents. *Nuclear Instruments and Methods in Physics Research Section B: Beam Interactions with Materials and Atoms*, 279, 96-99.
- Kogelschatz, U. (2012) Ultraviolet excimer radiation from nonequilibrium gas discharges and its application in photophysics, photochemistry and photobiology. *Journal of Optical Technology*, 79, 484-493.
- Kong, M. et al. Plasma medicine: an introductory review. (2009) *New Journal of Physics*, 11, 115012.

- Kottapalli, A. G. P., Asadnia, M., Miao, J. M., Barbastathis, G., & Triantafyllou, M. S. (2012). A flexible liquid crystal polymer MEMS pressure sensor array for fish-like underwater sensing. *Smart Materials and Structures*, *21*, 115030.
- Langmuir, I. (1913) The effect of space charge and residual gases on thermionic currents in high vacuum. *Physical Review*, *2*, 450-486.
- Laroussi, M. (2015) Low-temperature plasma jet for biomedical applications: a review. *IEEE Transactions on Plasma Science*, *43*, 703712.
- Lau, Y. Y., Liu, Y., and Parker, R. K. (1994) Electron emission: From the Fowler-Nordheim relation to the Child-Langmuir law. *Physical Review Letters*, *66*, 2082-2085.
- Lau, Y. Y., Chernin, D., Colombant, D. G., and Ho, P. T. (1991) Quantum extension of Child-Langmuir law. *Physical Review Letters*, *66*, 1446-1449.
- Lee, M. U., Jeong, S. Y., Won, I. H., Sung, S. K., Yun, G. S., and Lee, J. K. (2016) Non-Maxwellian to Maxwellian transitions of atmospheric microplasmas at microwave frequencies, *Physics of Plasmas*, *23*, 070704.
- Lee, M. U., Lee, J., Yun, G. S., and Lee, J. K. (2017a) Scalings and universality for high-frequency excited high-pressure argon microplasma, *The European Physical Journal D*, *71*, 94-99.
- Lee, M. U., Lee, J., Lee, J. K., and Yun, G. S. (2017b) Extended scaling and Paschen law for micro-sized radiofrequency plasma breakdown, *Plasma Sources Science and Technology*, *26*, 034003.
- Levko, D. and Raja, L. L. (2015) Breakdown of atmospheric pressure microgaps at high excitation frequencies. *Journal of Applied Physics*, *117*, 173303.
- Levko, D. and Raja, L. L. (2016) Electron kinetics in atmospheric-pressure argon and nitrogen in microwave microdischarges, *Journal of Applied Physics*, *119*, 163303.
- Li, M., Tang, H. X., and Roukes, M. L. (2007) Ultra-sensitive NEMS-based cantilevers for sensing, scanned probe and very high-frequency application. *Nature Nanotechnology*, *2*, 114-120.
- Li, W. & Li, D. Y. (2005) On the correlation between surface roughness and work function in copper. *The Journal of Chemical Physics*, *122*, 064708.
- Li, Y. & Go, D. (2014) The quantum mechanics of ion-enhanced field emission and how it influences microscale gas breakdown. *Journal of Applied Physics*, *116*, 103306.
- Li, Y., Tirumala, R., Rumbach, P., & Go, D. (2013) The coupling of ion-enhanced field emission and the discharge during microscale breakdown at moderately high pressure. *IEEE Transactions on Plasma Science*, *41*, 24-35.

- Lieberman, M. A. & Lichtenberg, A. J. (2005) *Principles of Plasma Discharges and Material Processing*, 3rd ed. Hoboken, John Wiley & Sons Inc.
- Lin, L. and Wang, Q. (2015) Microplasma: a new generation of technology for functional nanomaterial synthesis. *Plasma Chemistry and Plasma Processing*, 35, 925-962.
- Lin, J., Wong, P. Y., Yang, P., Lau, Y. Y., Tang, W., and Zhang, P., *Journal of Applied Physics*, 121, 244301 (2017).
- Lisovskiĭ, V. A. (1999) Criterion for microwave breakdown of gases. *Technical Physics*, 44, 1282-1285.
- Lisovskiy, V., Booth, J. P., Landry, K., Douai, D., Cassagne, V., and Yegorenkov, V. (2006) Electron drift velocity in argon, nitrogen, hydrogen, oxygen and ammonia in strong electric fields determined from rf breakdown curves. *Journal of Physics D: Applied Physics*, 39, 660-665.
- Lisovskiy, V. A. and Yegorenkov, V. D. (1998) RF breakdown of low-pressure gas and a novel method for determination of electron-drift velocities in gases. *Journal of Physics D: Applied Physics*, 31, 3349-3357.
- Little, R. P. and Smith, S. T. Electrical breakdown in vacuum. (1965) *IEEE Transactions on Electron Devices*, 12, 77-83.
- Loeb, L. B. & Meek, J. M. (1941) *Mechanism of Electric Spark*. Stanfor, CA. Stanford University Press.
- Loveless, A. M. (2017) *General Gas Breakdown Theory from Microscale to the Classical Paschen Law*, M. S. Thesis, Purdue University.
- Loveless, A. M. & Garner, A. L. (2016) Scaling laws for gas breakdown for nanoscale to microscale gaps at atmospheric pressure. *Applied Physics Letters*, 108, 234103.
- Loveless, A. M. & Garner, A. L. (2017a) Generalization of microdischarge scaling laws for all gases at atmospheric pressure. *IEEE Transactions on Plasma Science*, 45, 5574-583.
- Loveless, A. M. and Garner, A. L. (2017b) A universal theory for gas breakdown from microscale to the classical Paschen law. *Physics of Plasmas*, 24, 113522.
- Loveless, A. M. and Garner, A. L. (2017c) Scaling laws for AC gas breakdown and implications for universality. *Physics of Plasmas*, 24, 104501.
- Loveless, A. M., Meng, G., Ying, Q., Wu, F., Wang, K., Cheng, Y., and Garner, A. L. (2019) The transition to Paschen's law for microscale gas breakdown at subatmospheric pressure, *Scientific Reports*, 9, 5669.

- Mahamud, R. & Farouk, T. L. (2016) Ion kinetics and self pulsing in DC microplasma discharges at atmospheric and higher pressures. *Journal of Physics D: Applied Physics*, *49*, 145202.
- Maric, D., Radmilovic-Radjenov, M., & Petrovic, Z. Lj. (2005) On parametrization and mixture laws for electron ionization coefficients. *The European Physical Journal D—Atomic, Molecular, Optical, and Plasma Physics*, *35*, 313-321.
- Martinez-Sanchez, M. and Pollard, J. E. (1998) Spacecraft electric propulsion—An overview. *Journal of Propulsion and Power*, *14*, 688–699.
- Meng, G., Cheng, Y., Wu, K., and Chen, L. (2014) Electrical Characteristics of Nanometer Gaps in Vacuum under Direct Voltage. *IEEE Transactions on Dielectrics and Electrical Insulation*, *21*, 1950-1956.
- Meng, G., Gao, X., Loveless, A. M., Dong, C., Zhang, D., Wang, K., Zhu, B., Cheng, Y., and Garner, A. L. (2018) Demonstration of field emission driven microscale gas breakdown for pulsed voltages using in-situ optical imaging. *Physics of Plasmas*, *25*, 082116.
- Meng, G., Ying, Q., Loveless, A. M., Wu, F., Wang, F., Wang, K., Fu, Y., Garner, A. L., and Cheng, Y. (2019) Spatio-temporal dynamics of pulsed gas breakdown in microgaps. *Physics of Plasmas*, *26*, 014506.
- Miller, R., Lau, Y. Y., & Booske, J. H. (2007) Electric field distribution on knife-edge field emitters. *Applied Physics Letters*, *91*, 074105.
- Montijn, C. & Ebert, U. (2006) Diffusion correction to the Raether-Meek criterion for the avalanche-to-streamer transition. *Journal of Physics D: Applied Physics*, *39*, 2979-2992.
- Mott, N. F. and Gurney, R. W. *Electronic Processes in Ionic Crystals*. Clarendon Press, Oxford, 1940.
- Murphy, E. L. and Good, R. H. (1956) Thermionic emission, field emission, and the transition region. *Physical Review*, *102*, 1464.
- Nagorny, V. P. & Drallos, P. J. (1997) Effective secondary emission coefficient in a high pressure noble gas. *Plasma Sources Science and Technology*, *6*, 212-219.
- Nguyen, H. K., Mankowski, J., Dickens, J. C., Neuber, A. A., and Joshi, R. P. (2017) Model predictions for atmospheric air breakdown by radio-frequency excitation in large gaps. *Physics of Plasmas*, *24*, 073505.
- Neuber, A. A., Krile, J. T., Edmiston, G. F., and Krompholz, H. G. (2007) Dielectric surface flashover at atmospheric conditions under high-power microwave excitation. *Physics of Plasmas*, *14*, 057102.

- Park, H. J., Kim, S. H., Ju, H. W., Lee, H., Lee, Y., Park, S., Yang, H., Park, S.-J., Eden, J. G., and Yang, J. (2018) Microplasma Jet Arrays as a Therapeutic Choice for Fungal Keratitis. *Scientific Reports*, 8, 2422.
- Paschen, F. (1889) Ueber die zum Funkenübergang in Luft, Wasserstoff und Kohlensäure bei verschiedenen Drucken erforderliche Potentialdifferenz. *Annalen der Physik*, 273, 69-96.
- Phelps, A. V. (1999) Cold-cathode discharges and breakdown in argon: Surface and gas phase production of secondary electrons. *Plasma Sources Science and Technology*, 8, R21-R44.
- Radmilović-Radjenović, M. & Radjenović, B. (2007) The influence of ion-enhanced field emission of the high-frequency breakdown in microgaps. *Plasma Sources Science and Technology*, 16, 337-340.
- Radmilović-Radjenović, M. & Radjenović, B. (2008a) An analytical relation describing the dramatic reduction of the breakdown voltage for the microgap devices. *Europhysics Letters*, 83, 25001.
- Radmilović-Radjenović, M. & Radjenović, B. (2008b) Theoretical study of the electron field emission phenomena in the generation of a micrometer scale discharge. *Plasma Sources Science and Technology*, 17, 024005.
- Radmilović-Radjenović, M and Lee, J. K. (2005) Modeling of breakdown behavior in radio-frequency argon discharges with improved secondary emission model, *Physics of Plasmas*, 12, 063501.
- Radmilović-Radjenović, M., Lee, J. K., Iza, F., & Park, G. Y. (2005) Particle-in-cell simulation of gas breakdown in microgaps. *Journal of Physics D: Applied Physics*, 38, 950-954.
- Radmilović-Radjenović, M., Radjenović, B., Matejčić, S., & Klas, M. (2014) The breakdown phenomena in micrometer scale direct current gas discharges. *Plasma Chemistry and Plasma Processing*, 34, 55-64.
- Ragan-Kelley, B., Verboncoeur, J., & Feng, Y. (2009) Two-dimensional axisymmetric Child-Langmuir scaling law. *Physics of Plasmas*, 16, 103102.
- Raizer, Y. P. (1991) *Gas Discharge Physics*. Berlin: Springer.
- Rezvykh, K. A. and Romanov, V. A. (1999) Gases breakdown voltage calculation for the case of accelerator nonuniform fields by the method of base. *Nuclear Instruments and Methods in Physics Research Section A: Accelerators, Spectrometers, Detectors and Associated Equipment*, 423, 203-212.
- Rosenbluth, M. N. and Putyinski, S. V. (1997) Theory for avalanche of runaway electrons in tokamaks. *Nuclear Fusion*, 37, 10.

- Roveri, D. S., Sant'Anna, G. M., Bertan, H. H., Mologni, J. F., Alves, M. A. R., & Braga, E. S. (2016) Simulation of the enhancement factor from an individual 3D hemisphere-on-post field emitter by using finite elements method. *Ultramicroscopy*, 160, 247-251.
- Sanders, D. M. and Anders, A (2000) Review of cathodic arc deposition technology at the start of the new millennium. *Surface Coatings and Technology*, 133-134, 78-90.
- Schoenbach, K. H. and Becker, K. (2016) 20 years of microplasma research: a status report. *The European Physical Journal D*, 70, 29.
- Semnani, A., Venkatraman, A., Alexeenko, A., and Peroulis, D. (2013) Frequency response of atmospheric pressure gas breakdown in micro/nanogaps. *Applied Physics Letters*, 103, 063102.
- She, J. C., Xu, N. S., Deng, S. Z., and Chen, J. (2003) Vacuum breakdown of carbon-nanotube field emitters on a silicon tip. *Applied Physics Letters*, 83, 2671-2673.
- Sinelnikob, D., Kahita, S., Bulgadaryan, D., Kurnaev, V., Hwangbo, D., Ohno, N. (2018) Emission from tungsten nanostructured tendril bundles under local thermal load. 28th International Symposium on Discharges and Electrical Insulation in Vacuum (ISDEIV). Sept. 2018.
- Sitaraman, H. and Raja, L. L. (2012) Simulation studies of RF excited micro-cavity discharges for micro-propulsion applications, *Journal of Physics D: Applied Physics*, 45, 185201.
- Slade, P. G. & Taylor, E. D. (2002) Electrical breakdown in atmospheric air between closely spaced (0.2 μm -40 μm) electrical contacts. *IEEE Transactions on Component Packaging and Technology*, 25, 390-396.
- Smith, H. B., Charles, C., and Boswell, R. W. (2003) Breakdown behavior in radio-frequency argon discharges. *Physics of Plasmas*, 10, 875-881.
- Song, X., Duan, X. R., Song, X. M., Zheng, G. Y., Wang, S., Li, B., Bai, X. Y., Song, Sh. D., Wang, C., and Sun, J. (2018) Experimental results of plasma breakdown and flux optimization on HL-2A tokamak. *Fusion Eng. Design*, 125, 195-198.
- Spindt, C. A., Brodie, I., Humphrey, L., and Westerberg, E. R. (1976) Physical properties of thin-film field emission cathodes with molybdenum cones. *Journal of Applied Physics*, 47, 5248-5263.
- Taguchi, T. & Antonsen, T. M. Jr. (2004) Resonant heating of a cluster plasma by intense laser light. *Physical Review Letters*, 92, 205003.
- Tholeti, S. S., Shiykumar, G., & Alexeenko, A. A. (2016) Field emission microplasma actuation for microchannel flows. *Journal of Physics D: Applied Physics*, 49, 215303.

- Tirumala, R. T. & Go, D. B. (2010) An analytical formulation for the modified Paschen's curve. *Applied Physics Letters*, 97, 151502.
- Torfason, K., Valfells, A., and Manolescu, A. (2015) Molecular dynamics simulations of field emission from a planar nanodiode. *Physics of Plasmas*, 22, 033109.
- Torfason, K., Valfells, A., & Manolescu, A. (2016) Molecular dynamics simulations of field emission from a prolate spheroidal tip. *Physics of Plasmas*, 23, 123119.
- Torres, J. M. & Dhariwal, R. S. (1999) Electric field breakdown at micrometer separations. *Nanotechnology*, 10, 102-107.
- Ursu, I., Apostol, I., CrAcjun, D., Dinescu, M., MahAilescu, I. N., Nistor, L., Popa, A., Teodorescu, V. S., Prokhorov, A. M., Chapliev, N. I., & Konov, V. I. (1984) On the influence of surface condition on air plasma formation near metals irradiated by microsecond TEA CO₂ laser pulses. *Journal of Physics D: Applied Physics*, 17, 709-720.
- Venkatraman, A. (2012) "Particle simulations of ion generation and transport in microelectromechanical systems and microthrusters," Ph.D. dissertation, Dept. Aero. Eng., Purdue Univ., West Lafayette, IN.
- Venkatraman, A. (2014a) Electric field enhancement due to a saw-tooth asperity in a channel and implications on microscale gas breakdown. *Journal of Physics D: Applied Physics*, 47, 425205.
- Venkatraman, A. (2014b) Generalized criterion for thermos-field emission driven electrical breakdown of gases. *Applied Physics Letters*, 104, 194101.
- Venkatraman, A. & Alexeenko, A. A. (2012) Scaling law for direct current field emission-driven microscale gas breakdown. *Physics of Plasmas*, 19, 123515.
- Venkatraman, A., Garg, A., Peroulis, D., & Alexeenko, A. A. (2012) Direct measurements and numerical simulations of gas charging in microelectromechanical system capacitive switches. *Applied Physics Letters*, 100, 083503.
- Verboncoeur, J. P., Alves, M. V., Vahedi, V., and Birdsall, C. K. (1993) Simultaneous potential and circuit solution for 1D bounded plasma particle simulation codes. *Journal of Computational Physics*, 104, 321-328.
- Wallash A. and Levit, L. (2003) Electrical breakdown and ESD phenomena for devices with nanometer-to-micron gaps, *Reliability, Testing, and Characterization of MEMS/MOEMS II*. 87-96.
- Wang, S., Mi, J., Li, Q., Jin, R., and Dong, J. (2017) Fractional microplasma radiofrequency technology for non-hypertrophic post-burn scars in Asians: A prospective study of 95 patients. *Lasers in Surgery and Medicine*, 49, 563-569.

- Warne, L. K., Jorgenson, R. E., & Nicolaysen, S. D. (2003) Ionization coefficient approach to modeling breakdown in nonuniform geometries. *Sandia Report SAND2003-4078*.
- Welch, D. R., Cuneo, M. E., Olson, C. L., and Mehlhorn, T. A. (1996) Gas breakdown effects in the generation and transport of light ion beams for fusion. *Physics of Plasmas*, 3, 2113-2121.
- Wright, W. P. & Ferrer P. (2015) Electric micropropulsion systems. *Progress in Aerospace Science*, 74, 48-61.
- Zhang, P., Valfells, Á., Ang, L., Luginsland, J., and Lau, Y. (2017) 100 years of the physics of diodes. *Applied Physics Reviews*., 4, 011304.
- Zhu, Z., Chan, G. C.-Y., Ray, S. J., Zhang, X. and Hieftje, G. M. (2008) Microplasma source based on a dielectric barrier discharge for the determination of mercury by atomic emission spectrometry. *Analytical Chemistry*, 80, 8622-8627.
- Zubarev, N. M. and Ivanov, S. N. (2018) Mechanism of runaway electron generation at gas pressures from a few atmospheres to several tens of atmospheres. *Plasma Physics Reports*, 44, 445-452.

VITA

Education

Doctor of Philosophy, Nuclear Engineering Anticipated Aug 2020
Purdue University, West Lafayette, Indiana
Dissertation Topic: Implications of Nanoscale Features on Gas Breakdown and Electron Emission
Advisor: Prof. Allen Garner

Master of Science, Nuclear Engineering May 2017
Purdue University, West Lafayette, Indiana
Thesis Title: General Gas Breakdown Theory from Microscale to the Classical Paschen Law
Advisor: Prof. Allen Garner

Bachelor of Science, Nuclear Engineering May 2015
Purdue University, West Lafayette, Indiana

Experience

Graduate Research Assistant June 2015—Present
BioElectrics and ElectroPhysics (BEEP) Laboratory
Purdue University, West Lafayette, IN
Advisor: Prof. Allen Garner

- Developing theoretical models for predicting gas breakdown voltage for gaps ranging from nanoscale to microscale.
- Coupled field emission and Townsend breakdown effects for a more unified equation
- Work with experimentalists to assess the impact of microscale gas breakdown mechanisms with gap distance, pressure, and cathode surface roughness.

Grader for Nuclear Engineering Courses Aug 2015—Dec 2015, Aug 2016—Dec 2016
Purdue University, West Lafayette, IN

- Graded lab reports, quizzes, exams, and homework for *Nuclear Engineering Undergraduate Lab II* (NUCL 305) and *Engineering Mathematics using Mathematica* course (NUCL 497/597). NUCL 305 covers radiation detectors and reactor operations for seniors majoring in Nuclear Engineering. NUCL 497/597 provides refresher on mathematics ranging from series expansions to differential equations with an emphasis on applications in engineering, physics, and life sciences.
- Collaborated with the other TAs and professors for the courses

Grader for Introductory Nuclear Engineering Courses Jan 2014—May 2015
Purdue University, West Lafayette, IN

- Graded lab reports, quizzes, exams, and homework for *Nuclear Engineering Undergraduate Lab I* (NUCL 205), which is a sophomore level laboratory class covering radiation detectors and measurements, and *Introduction to Nuclear Engineering* (NUCL 200), which is a sophomore level class providing a basic introduction to relevant nuclear engineering and physics.

- Collaborated with the other TAs and professors for the courses
- Provided feedback to the instructor for a newly created Nuclear Engineering course (*Engineering Mathematics using Mathematica*) to aid in revising the curriculum for the second course offering.

Undergraduate Research Assistant

Aug 2013—Dec 2014

BioElectrics and ElectroPhysics (BEEP) Laboratory

Purdue University, West Lafayette, IN

Advisor: Prof. Allen Garner

- Completed manuscript preparation for age-dating for uranium metal.
- Assessed neutron interactions with target materials and neutron lenses for amplifying neutron concentration using the code Monte Carlo n-Particles (MCNP).

Summer Undergraduate Research Fellowship Recipient (SURF)

May 2014—Aug 2014

Purdue University, West Lafayette, IN

Advisor: Prof. Allen Garner

- Analyzed laser-material interactions, focusing on neutron production for medicine and security
- Educated fellow participants in laser-material interactions at end-of-summer research symposium
- These efforts formed the foundation for the PI's application for the Nuclear Forensics Junior Faculty Award

Nuclear Forensics Undergraduate Scholarship Recipient

May 2013—Aug 2013

Y-12 National Security Complex, Oak Ridge, TN

- Studied the feasibility of using radiolytically-induced damage to the crystalline structure of uranium metal to determine the time since formation
- Mastered SRIM/TRIM and Origen software to facilitate the simulations of particle interactions
- Presented a poster at the National Technical Nuclear Forensics Program Review in Washington, D.C. showing the progress made on developing a new age-dating method
- Gave an oral presentation summarizing the project at the Nuclear Forensics Undergraduate Scholarship Program Review in Albuquerque, NM
- Communicated project conclusions and internship experiences at a Nuclear Engineering Undergraduate Seminar at Purdue University

Computer Consultant

May 2011—Sep 2014

Physics Computer Network, Purdue University

- Supported faculty and staff in the physics building with technology issues
- Assisted with everyday tasks and longer, ongoing projects

Awards

- 2020 Purdue College of Engineering (COE) Outstanding Graduate Research Award for the School of Nuclear Engineering
- 2019-2020 Directed Energy Professional Society (DEPS) Scholarship

- 2018-2019 Directed Energy Professional Society (DEPS) Scholarship
- 2018 Igor Alexeff Outstanding Student in Plasma Science Award
- 2017-2018 Directed Energy Professional Society (DEPS) Scholarship
- 2017 IEEE International Conference on Plasma Science (ICOPS) Best Student Paper 2nd runner up
- 2017 IEEE International Conference on Plasma Science (ICOPS) Student Travel Grant
- 2017 IEEE Nuclear and Plasma Sciences Society (NPSS) Graduate Scholarship
- 2016-2017 IEEE Dielectric and Electrical Insulation Society (DEIS) Graduate Fellow
- 2016-2017 Otto F. and Jenny H. Krauss Scholarship
- 2016 American Physics Society Division of Plasma Physics (APS-DPP) Student Travel Grant
- 2016 IEEE International Conference on Plasma Science (ICOPS) Best Student Paper 1st Place
- 2016 Electrostatics Society of America Best Student Paper 1st Place
- 2016 IEEE International Conference on Plasma Science (ICOPS) Student Travel Grant
- 2015 American Physics Society Division of Plasma Physics (APS-DPP) Student Travel Grant

Oral Presentations (Presenter in *italics*)

28. R. S. Brayfield, II, A. M. Darr, W. L. Li, A. J. Fairbanks, H. Wang, **A. M. Loveless**, and A. L. Garner, “Nano/micro-meter electrode topology effects on electron emission,” 22nd Annual Directed Energy Science & Technology Symposium, Student Workshop II, 11 March 2020, West Point, NY, USA.

27. **A. M. Loveless**, A. M. Darr, and A. L. Garner, “Implications of electrode geometry on electron emission and microscale gas breakdown,” 22nd Annual Directed Energy Science & Technology Symposium, Student Workshop II, 11 March 2020, West Point, NY, USA.

26. **A. M. Loveless**, A. M. Darr, R. S. Brayfield II, J. R. Malayter, S. A. Lang, and A. L. Garner, “Nanoscale Feature Implications on Electron Emission and Gas Breakdown,” American Nuclear Society Winter Meeting (ANS), 21 November 2019, Washington D.C., USA.

25. **[INVITED]** *A. L. Garner*, **A. M. Loveless**, R. S. Brayfield II, A. M. Darr, J. R. Malayter, G. Meng, “Gas breakdown and electron emission for microscale and smaller gaps: unified theory and nanofeature effects,” International Vacuum Nanoelectronics Conference (IVNC), 11.1, 25 July 2019, Cincinnati, OH, USA.

24. *R. Brayfield*, A. Fairbanks, **A. Loveless**, S. Gao, C. Darr, J. Malayter, W. Wu, and **A. Garner**, “Microscale Gas Breakdown Voltage Dependence on Electrode Surface,” IEEE Pulsed Power and Plasma Science Conference, 3F3, 25 June 2019, Orlando, FL, USA.

23. **A. Loveless**, A. Darr, and **A. Garner**, “Electron Emission and Gas Breakdown: Unification of Theory from Schrodinger’s Equation to Paschen’s Law,” IEEE Pulsed Power and Plasma Science Conference, 3F2, 25 June 2019, Orlando, FL, USA.

22. **A. Loveless**, M. Lopez de Bertodano, and **A. Garner**, “Modification of the Hodgkin-Huxley Wave Behavior by Electroporation,” IEEE Pulsed Power and Plasma Science Conference, 2D2, 24 June 2019, Orlando, FL, USA.

21. *A. Darr, A. Loveless, and A. Garner*, “Incorporating Resistance into the Unification of Field Emission and Space Charge-Limited Emission with Collisions,” IEEE Pulsed Power and Plasma Science Conference, 7A3, 27 June 2019, Orlando, FL, USA.
20. *G. Meng, Q. Ying, A. Loveless, F. Wu, K. Wang, Y. Fu, A. Garner, and Y. Cheng*, “Spatio-temporal Dynamics of Pulsed Gas Breakdown in Microgaps,” IEEE Pulsed Power and Plasma Science Conference, 10C2, 28 June 2019, Orlando, FL, USA.
19. *R. S. Brayfield, II, A. J. Fairbanks, A. M. Loveless, S. Gao, W. Li, C. Darr, J. R. Malayter, W. Wu, and A. L. Garner*, “Experimental assessment of electrode effects on gas breakdown for microscale gaps,” 21st Annual Directed Energy Science & Technology Symposium, Student Workshop II, 10 April 2019, Destin, FL, USA.
18. *A. M. Loveless, A. M. Darr, and A. L. Garner*, “Transition of Electron Emission and Gas Breakdown Mechanisms from Microscale to Nanoscale,” 21st Annual Directed Energy Science & Technology Symposium, Student Workshop I, 09 April 2019, Destin, FL, USA.
17. *A. Loveless, A. Darr, S. Dynako, and A. Garner*, “Unification of Gas Breakdown and Electron Emission,” American Physical Society March Meeting 2019, Bull. Am. Phys. Soc., Vol. 64, R18.00004 (2019).
16. *A. Loveless and A. Garner*, “Electron Emission and Gas Breakdown from Schrödinger’s Equation to Paschen’s Law,” American Physical Society Division of Plasma Physics, Bull. Am. Phys. Soc., No. 63, NO8.00002 (2018).
15. [INVITED] *A. L. Garner, A. M. Loveless, R. S. Brayfield II, A. J. Fairbanks, S. D. Dynako, S. Gao, W. Wu, R. S. Bean, and G. Meng*, “Gas Breakdown at Microscale and Smaller Gaps: Theoretical Unification of Mechanisms and Experimental Assessment of Surface Roughness,” iPlasmaNano-IX, New Buffalo, MI, 27 August 2018.
14. *A. M. Loveless, A. M. Darr, S. D. Dyanko, and A. L. Garner*, “Transition from Microscale to Nanoscale Breakdown Dynamics,” 2018 IEEE International Conference on Plasma Sciences, O3A-2, 26 June 2018, Denver, CO USA.
13. *A. L. Garner, R. S. Brayfield II, A. J. Fairbanks, A. M. Loveless, S. Gao, R. S. Bean, Y. Xuan, and W. Wu*, “Microscale Gas Breakdown and Implications to Electron Emission,” 20th Annual Directed Energy Science & Technology Symposium, High Power Microwave (HPM) Technologies, 01 March 2018, Oxnard, CA, USA.
12. *A. M. Loveless, A. M. Darr, S. D. Dynako, and A. L. Garner*, “Gas Breakdown Dynamics: From Microscale to Nanoscale,” 20th Annual Directed Energy Science & Technology Symposium, Education Workshop I, 27 February 2018, Oxnard, CA, USA.
11. [STUDENT EXCELLENCE AWARD FINALIST] *A. Loveless, A. Darr, and A. Garner*, “Gas Breakdown: Across Length Scales and Frequency,” Bull. Am. Phys. Soc. Vol. 62, No. 10, ET2.00002 (2017).
10. *A. M. Loveless and A. L. Garner*, “AC Gas Breakdown Scaling Laws,” 2017 Annual Report Conference on Electrical Insulation and Dielectric Phenomena, pp. 632-635 (2017).
9. [STUDENT BEST PAPER COMPETITION] *A. M. Loveless and A. L. Garner*, “Universal Gas Breakdown Theory from Microscale to the Classical Paschen Law,” 2017 IEEE International

Conference on Plasma Sciences, Student Award Competition, 23 May 2017, Atlantic City, NJ USA.

8. **A. M. Loveless** and A. L. Garner, “Universal Gas Breakdown Theory from Microscale to the Classical Paschen Law,” 2017 IEEE International Conference on Plasma Sciences, Oral MO 1.1-3, 22 May 2017, Atlantic City, NJ USA.

7. **A. M. Loveless** and A. L. Garner, “Generalizing Microdischarge Breakdown Scaling Laws for Pressure and Gas,” Bull. Am. Phys. Soc. Vol. 61, No. 18, TO7.00010 (2016).

6. **[INVITED] A. M. Loveless** and A. L. Garner, “Matched Asymptotic Analysis of Atmospheric Pressure Gas Breakdown from Nanoscale to Microscale,” 2016 IEEE International Conference on Plasma Sciences, Oral 3A-5, 21 June 2016, Banff, Alberta, Canada.

5. **[STUDENT BEST PAPER COMPETITION] A. M. Loveless** and A. L. Garner, “Generalization of Scaling Laws for Gas Breakdown to Account for Pressure,” 2016 IEEE International Conference on Plasma Sciences, Poster 1P-3, 21 June 2016, Banff, Alberta, Canada.

4. **A. M. Loveless** and **A. L. Garner**, “Predicting breakdown voltage for microscale and nanoscale gaps as a function of pressure,” Proc. 2016 Electrostatics Joint Conference, Oral R1, 16 June 2016, West Lafayette, IN.

3. *A. L. Garner*, R. S. Bean, *G. McCullough, Sr.*, and **A. M. Loveless**, “Proposal for a Nuclear Reactor Operations Course at Purdue University,” Conference on Nuclear Training and Education (CONTE), 03 February 2015, Jacksonville, FL, pp. 90-91.

2. **A. M. Loveless**, A. L. Garner, R. D. Bean, and N. Satvat, “Optimizing neutron yield for active interrogation,” The Summer Undergraduate Research Fellowship (SURF) Symposium, 07 August 2014, West Lafayette, IN, no. 116 (2014).

1. **A. Loveless**, “Age-dating uranium metal using microstructural damage,” Nuclear Forensics Undergraduate Scholarship Program Review, Albuquerque, NM, 19 December 2013.

Poster Presentations (Presenter in italics)

13. **A. M. Loveless**, A. M. Darr, R. S. Brayfield II, J. R. Malayter, S. A. Lang, and A. L. Garner, “The implications of nanoscale features for microscale and small gaps on electron emission,” International Vacuum Nanoelectronics Conference (IVNC), 18.1, 24 July 2019, Cincinnati, OH, USA.

12. J. Malayter, R. Brayfield, **A. Loveless**, and **A. Garner**, “Implications of surface roughness on microscale gas breakdown theory,” IEEE Pulsed Power and Plasma Science Conference, 1P02, 24 June 2019, Orlando, FL, USA.

11. *R. Brayfield*, A. Fairbanks, **A. Loveless**, W. Li, C. Darr, and **A. Garner**, “Submicroscale Gas Breakdown as a Function of Cathode Protrusion,” 1P21, 24 June 2019, Orlando, FL USA.

10. **A. Loveless**, K. Torfason, A. Valfells, and **A. Garner**, “Investigation of Electron Emission using Molecular Dynamics Simulations,” IEEE Pulsed Power and Plasma Science Conference, 1P05, 24 June 2019, Orlando, FL, USA.

9. **A. Loveless**, Z. Vander Missen, A. Semnani, and **A. Garner**, “RF Gas Breakdown Theory and Experiment as a Function of Gas, Gap Size, Frequency, and Pressure,” IEEE Pulsed Power and Plasma Science Conference, 1P04, 24 June 2019, Orlando, FL, USA.

8. A. L. Garner, **A. M. Loveless**, Z. Vander Missen, and A. Semnani, "AC Gas Breakdown: From Simple Scaling Laws to Experiments," 2018 IEEE International Conference on Plasma Sciences, P2A-1346-12, 27 June 2018, Denver, CO USA.
7. A. L. Garner, **A. M. Darr**, and **A. M. Loveless**, "Incorporating Collisions into the Transition from Field Emission to Space Charge Limited Flow," 2018 IEEE International Conference on Plasma Sciences, P2A-1346-1, 27 June 2018, Denver, CO USA.
6. **A. M. Loveless** and A. L. Garner, "Scaling Laws for AC Breakdown Voltage in Microdischarges," 2017 IEEE International Conference on Plasma Sciences, MO Posters-2, 22 May 2017, Atlantic City, NJ USA.
5. **A. M. Darr**, **A. M. Loveless**, and **A. L. Garner**, "Quantum Scale Breakdown," 2017 IEEE International Conference on Plasma Sciences, MO Posters-1, 22 May 2017, Atlantic City, NJ USA.
4. **A. M. Loveless** and A. L. Garner, "Generalization of Scaling Laws for Gas Breakdown to Account for Pressure," 2016 IEEE International Conference on Plasma Sciences, Poster 1P-3, 20 June 2016, Banff, Alberta, Canada.
3. **A. M. Loveless** and **A. L. Garner**, "Calculating Field Enhancement Factor using the Boundary Element Method," Proc. 2016 Electrostatics Joint Conference, Poster G3, 14 June 2016, West Lafayette, IN.
2. **A. Loveless**, A. Garner, and A. Valfells, "Unifying Paschen Curve Conditions across Pressure and Gap Distance," Bull. Am. Phys. Soc. Vol. 60, No. 19, JP12.00141 (2015).
1. **A. Loveless**, G. Schaaff, E. Peskie, and H. Hall, "Dating of Uranium Metal," National Technical Nuclear Forensics Program Review, Merrifield, VA, 21 July 2013.

Invited Seminars

2. **A. M. Loveless**, "Unification of gas breakdown laws across frequency and gap distance," Naval Research Laboratory, 10 July 2018.
1. **A. Loveless**, "Age-dating Uranium Metal using Microstructural Damage," School of Nuclear Engineering, Purdue University, Undergraduate Seminar, 06 November 2013.

Service

- Graduate student mentor for 2018 Summer Undergraduate Research Fellowship (SURF) student
- Panelist for the 2018 IEEE International Conference on Plasma Science (ICOPS) Best Student Paper award.
- Reviewed 2016 IEEE Power Modulator and High Voltage Conference manuscripts.
- Co-Vice President of Purdue's Nuclear Engineering Graduate Organization (NEGO)
- Helped assemble the Abstract Book and the final Conference Proceedings for the 2014 IEEE Power Modulator and High Voltage Conference for over 200 submissions.

PUBLICATIONS

Journal Articles

A. M. Loveless, A. M. Darr, and A. L. Garner, “Unification of Electron Emission and Breakdown Mechanism Theories from Quantum Scales to Paschen’s Law,” Submitted.

14. A. L. Garner, **A. M. Loveless**, J. N. Dahal, and A. Venkatraman, “A Tutorial on Theoretical and Computational Techniques for Gas Breakdown in Microscale Gaps,” *IEEE Transactions on Plasma Science* **48**, 808-824 (2020).

13. R. S. Brayfield, II, A. J. Fairbanks, **A. M. Loveless**, S. Gao, A. Dhanabal, W. Li, C. Darr, W. Wu, and A. L. Garner, “The Impact of Cathode Surface Roughness and Multiple Breakdown Events on Microscale Gas Breakdown at Atmospheric Pressure,” *Journal of Applied Physics* **125**, 203302 (2019).

12. **A. M. Loveless**, G. Meng, Q. Ying, F. Wu, K. Wang, Y. Cheng, and A. L. Garner, “The Transition to Paschen’s Law for Microscale Gas Breakdown at Subatmospheric Pressure,” *Scientific Reports* **9**, 5669.

11. G. Meng, Q. Ying, **A. M. Loveless**, F. Wu, K. Wang, Y. Fu, A. L. Garner, and Y. Cheng “Spatio-temporal dynamics of pulsed gas breakdown in microgaps,” *Physics of Plasmas* **26**, 014506 (2019).

10. A. M. Darr, **A. M. Loveless**, and A. L. Garner, “Unification of field emission and space charge limited emission with collisions,” *Applied Physics Letters* **114**, 014103 (2019).

9. S. Dyanko, **A. M. Loveless**, and A. L. Garner, “Sensitivity of Modeled Microscale Gas Breakdown Voltage due to Parametric Variation,” *Physics of Plasmas* **25**, 103505 (2018).

8. G. Meng, X. Gao, **A. M. Loveless**, C. Dong, D. Zhang, K. Wang B. Zhu, Y. Chen, and A. L. Garner, “Demonstration of Field Emission Driven Microscale Gas Breakdown for Pulsed Voltages using In-situ Optical Imaging,” *Physics of Plasmas* **25**, 082116 (2018). [Selected for Featured Article: <https://publishing.aip.org/publishing/journal-highlights/researchers-unravel-path-electrical-discharges-scales-are-phenomenally>]

7. **A. M. Loveless** and A. L. Garner, “A Universal Theory for Gas Breakdown from Microscale to the Classical Paschen Law,” *Physics of Plasmas* **24**, 113522 (2017).

6. **A. M. Loveless** and A. L. Garner, “Scaling Laws for AC Gas Breakdown and Implications for Universality,” *Physics of Plasmas* **24**, 104501 (2017).

5. A. L. Garner, A. Caiafa, Y. Jiang, S. Klopman, C. Morton, A. S. Torres, **A. M. Loveless**, and V. B. Neculaes, “Experimental Validation of a Compact, Flexible Pulsed Power Architecture for Ex Vivo Platelet Activation,” *PLoS ONE* **12**(7), e0181214 (2017).

4. V. S. Robinson, A. L. Garner, **A. M. Loveless**, and V. B. Neculaes, “Calculated plasma membrane voltage induced by applying electric pulses using capacitive coupling,” *Biomedical Physics & Engineering Express* **3**, 025016 (2017).

3. [INVITED] **A. M. Loveless** and A. L. Garner, “Generalization of Microdischarge Scaling Laws for All Gases at Atmospheric Pressure,” *IEEE Transactions on Plasma Science* **45(4)**, 574-583 (2017).
2. **A. M. Loveless** and A. L. Garner, “Scaling Laws for Gas Breakdown for Nanoscale to Microscale Gaps at Atmospheric Pressure,” *Applied Physics Letters* **108(23)**, 234103 (2016).
1. **A. M. Loveless**, T. G. Schaaff, and A. L. Garner, “Age-dating Uranium Metal using Microstructural Damage,” *Annals of Nuclear Energy* **83**, 298-301 (2015).

Conference Papers

4. **A. M. Loveless**, A. M. Darr, R. S. Brayfield II, J. R. Malayter, S. A. Lang, and A. L. Garner, “Nanoscale Feature Implications on Electron Emission and Gas Breakdown,” *Trans. Am. Nucl. Soc.* **121**, 399-401 (2019).
3. **A. M. Loveless** and A. L. Garner, “AC Gas Breakdown Scaling Laws,” 2017 Annual Report Conference on Electrical Insulation and Dielectric Phenomena, pp. 807-809 (2017).
2. **A. M. Loveless** and **A. L. Garner**, “Predicting Breakdown Voltage for Microscale and Nanoscale Gaps as a Function of Pressure,” Proc. 2016 Electrostatics Joint Conference, Oral R1, 16 June 2016, West Lafayette, IN.
1. **A. M. Loveless** and **A. L. Garner**, “Calculating Field Enhancement Factor using the Boundary Element Method,” Proc. 2016 Electrostatics Joint Conference, Poster G3, 14 June 2016, West Lafayette, IN.